ROADWAY-EMBEDDED TRANSMITTERS AND MULTI-PAD RECEIVERS FOR HIGH POWER DYNAMIC WIRELESS POWER TRANSFER

by

Benny J. Varghese

A dissertation submitted in partial fulfillment
of the requirements for the degree

of

DOCTOR OF PHILOSOPHY

in

Electrical Engineering

Approved:

Abhilash Kamineni, Ph.D. Major Professor	Regan A. Zane, Ph.D. Co-Advisor
Reyhan Baktur, Ph.D. Committee Member	Hongjie Wang, Ph.D. Committee Member
Nicholas Roberts, Ph.D. Committee Member	D. Richard Cutler, Ph.D. Interim Vice Provost of Graduate Studies

UTAH STATE UNIVERSITY
Logan, Utah

2021

ABSTRACT

Roadway-Embedded Transmitters and Multi-Pad Receivers for High Power Dynamic Wireless Power Transfer

by

Benny J. Varghese, Doctor of Philosophy

Utah State University, 2021

Major Professor: Abhilash Kamineni, Ph.D.
Department: Electrical and Computer Engineering

Electric vehicles (EVs) offer considerable economic and environmental benefits to society. Despite the decreasing vehicle costs and increasing range of newer EVs, the problem of range anxiety still exists. Range anxiety, at its core, is an issue of charging speeds rather than a concern about the driving range. Dynamic wireless charging of EVs is seen as a potential solution to this issue of range anxiety. Wireless charging technology also helps the push towards level 5 autonomy and opens new opportunities for how an EV can be utilized.

Dynamic wireless power transfer (DWPT) systems typically require a high initial investment due to the scale of deployment needed and require a certain level of EV adoption before they become economically viable. The challenges facing DWPT technologies are broadly categorized into development, deployment and operation challenges. To address the deployment challenges, this dissertation explores the pavement integration of dynamic wireless chargers using existing roadway construction methods. A 50 kW concrete-embedded DWPT system is built and tested. To improve infrastructure utilization and address the operation challenge, different vehicle classes need to recharge from the same charging infrastructure. This is made possible by the use of multi-pad receivers. This dissertation presents

the design of a 30 kW DWPT system using a receiver with three individual 11.1 kVA receivers to demonstrate the scalability of modular receivers.

To help further reduce the cost of development and implementation of DWPT systems, finite element method (FEM) and circuit simulation models are presented. These time-domain simulations can be used to develop and validate various control and communication schemes without the need for expensive hardware implementation. Finally, leakage magnetic field reduction to ensure safety and compliance for DWPT systems is discussed and an example system is analyzed using FEM simulations.

(145 pages)

PUBLIC ABSTRACT

Roadway-Embedded Transmitters and Multi-Pad Receivers for High Power Dynamic Wireless Power Transfer

Benny J. Varghese

Electric vehicles (EVs) offer considerable economic and environmental benefits to society. Despite the decreasing vehicle costs and increasing range of newer EVs, the problem of range anxiety still exists. Range anxiety, at its core, is an issue of charging speeds rather than a concern about the driving range. Dynamic wireless charging of EVs is seen as a potential solution to this issue of range anxiety. Further, wireless charging technology also helps the push towards level 5 autonomy and opens new opportunities for how an EV can be utilized.

Dynamic wireless power transfer (DWPT) systems typically require a high initial investment due to the scale of deployment needed and require a certain level of EV adoption before they become economically viable. The challenges facing DWPT technologies are broadly categorized into development, deployment and operation challenges. To address the deployment challenges, this dissertation presents the pavement integration of DWPT systems, and the design and validation of concrete-embedded wireless charging pads. To improve infrastructure utilization and address the operation challenge, different vehicle classes need to recharge from the same charging infrastructure. This is made possible by the use of multi-pad receivers, which allow different vehicle classes to receive different power levels using the same charging infrastructure. This work presents a scaled-down version of a multi-pad receiver system to demonstrate the operation and scalability of these modular receivers.

To help further reduce the cost of development and implementation of DWPT systems, finite element method (FEM) and circuit simulation models are presented. The time-domain

simulations can be used to develop and validate various control and communication schemes without the need for expensive hardware implementation. Finally, leakage magnetic field reduction to ensure safety and compliance for DWPT systems is discussed, and an example system is analyzed using FEM simulations.

To mom, dad and Emma...

ACKNOWLEDGMENTS

I would like to thank Dr. Abhilash Kamineni and Prof. Regan Zane for giving me an opportunity to work on exciting research at the ASPIRE engineering research center and for being excellent mentors. I also thank my committee members, Dr. Reyhan Baktur, Dr. Hongjie Wang, and Dr. Nick Roberts for their valuable feedback and time invested.

This work would not have been possible without the support and kindness of many friends and colleagues. I thank my friend and colleague Dr. Dorai Yelaverthi for many thought-provoking discussions and dinner conversations. I express gratitude to my colleague Shuntaro Inoue for his assistance with electro-magnetic simulations. A special thanks goes out to John Mermigas, Jonathan Scheelke, Dr. Mohammed Kamel, Nathan Raine, Pilaiwan Vaikasi, and Arden Barnes for their assistance in various projects over the past few years. I also thank Ryan Bohm, Dr. Reza Tavakoli, Dr. Zeljko Pantic, Dr. Ahmed Azad, and Ujjwal Pratik for their support and guidance in research activities. I'm thankful for the support Dr. Duleepa Thrimawithana and Dr. Marv Halling provided over the course of my study. I express my sincere gratitude to all the colleagues and staff at the lab for making the last few years a memorable experience.

Finally, I thank my parents for being a source of wisdom and guidance, and I thank Emma and her family for their constant support during this journey.

Benny J. Varghese

CONTENTS

Page

ABSTRACT . . . iii

PUBLIC ABSTRACT . . . v

ACKNOWLEDGMENTS . . . viii

LIST OF TABLES . . . xii

LIST OF FIGURES . . . xiii

ACRONYMS . . . xix

1 INTRODUCTION . . . 1
- 1.1 Background . . . 1
  - 1.1.1 The Need for Transportation Electrification . . . 1
  - 1.1.2 Challenges Facing the Mass Adoption of Electric Vehicles . . . 4
- 1.2 Review of Existing Research . . . 6
  - 1.2.1 Pad Designs . . . 7
  - 1.2.2 Power Electronics . . . 8
  - 1.2.3 Pavement Integration . . . 9
  - 1.2.4 System Modeling . . . 10
  - 1.2.5 Feasibility Studies . . . 11
- 1.3 Problem Statement . . . 13
- 1.4 Contributions . . . 13
- 1.5 Dissertation Organization . . . 14

2 DYNAMIC WIRELESS POWER TRANSFER . . . 16
- 2.1 Inductive Power Transfer . . . 16
- 2.2 Dual-LCCL System Design Methodology . . . 18
- 2.3 Power level definitions . . . 22

3 MODELING DYNAMIC WIRELESS POWER TRANSFER SYSTEMS . . . 24
- 3.1 Challenges in Modeling DWPT Systems . . . 24
- 3.2 Generalized DWPT System . . . 25
- 3.3 Simulation Workflow . . . 29
- 3.4 Magnetic Model . . . 30
  - 3.4.1 Unit-cell Model . . . 31
- 3.5 Circuit Model . . . 39
  - 3.5.1 LTSpice . . . 39
  - 3.5.2 PLECS . . . 39
  - 3.5.3 Summary . . . 41

4 ROADWAY-EMBEDDED TRANSMITTER COILS 44
4.1 Design Considerations 44
4.1.1 Wire Insulation Jacket 45
4.1.2 Coil Shape and Design 47
4.1.3 Ferrite Shape 48
4.1.4 Frequency Selection 49
4.1.5 Pavement Reinforcement 50
4.1.6 Thermal Management 52
4.1.7 Power Electronics Design 57
4.2 Hardware Development 58
4.3 Test Setup 60
4.3.1 Circulating Power Test 60
4.4 Results and Discussion 60
4.4.1 Wireless Power Transfer Tests 60
4.4.2 Structural Testing 61
4.4.3 Summary 68

5 MULTI-PAD RECEIVER COILS 69
5.1 Design Considerations 69
5.2 Connection Methods for Multiple Receivers 70
5.2.1 Independent Receivers 70
5.2.2 Series or Parallel Connected Receivers 72
5.2.3 Analytical Comparison 73
5.3 Simulation Models 76
5.3.1 ANSYS Maxwell 76
5.3.2 PLECS 77
5.3.3 LTSpice 77
5.4 Hardware Development 80
5.4.1 Vehicle Detection System 82
5.4.2 Compensation Networks 83
5.4.3 Pad Weatherproofing 84
5.5 Transmitter Power Electronics 85
5.6 Receiver Power Electronics 86
5.7 Testing and Results 86
5.7.1 Track Current Tests 88
5.7.2 Open Circuit Voltage Tests 88
5.7.3 Electric and Magnetic Field Safety 90
5.7.4 Power Transfer Tests 92
5.7.5 Summary 98

6 SAFETY AND COMPLIANCE FOR DWPT SYSTEMS 99
6.1 Introduction 99
6.2 ICNIRP Limits 99
6.3 CISPR Limits 100
6.4 Booster Pad Example 101
6.4.1 ANSYS Model 102
6.4.2 LTSpice Model 104

6.5 Methods to Reduce Leakage Magnetic Field 105
6.5.1 Passive Shielding 106
6.5.2 Active Shielding 106
6.5.3 Simulation Results 106
6.5.4 Summary 111

7 CONCLUSIONS AND FUTURE WORK 112
7.1 Conclusions 112
7.2 Future Work 113

REFERENCES 114

CURRICULUM VITAE 125

LIST OF TABLES

Table		Page
1.1	Nomenclature used to describe inductive WPT pads.	7
3.1	Example 1 geometric parameters.	32
3.2	Example 2 geometric parameters.	32
4.1	Long-term inductance and resistance values [1].	45
4.2	Summary of how system attributes are affected by frequency.	51
4.3	LCCL Compensation Values for the Primary Pad	58
4.4	LCCL Compensation Values for the Secondary Pad	58
4.5	Testing conditions for fatigue cycling	64
5.1	Secondary Side LCCL Compensation Values for Series and Parallel Connected Multi-Pad Receivers	74
5.2	LCCL Compensation Network Sizing for Series Connected Multi-Pad Receiver	75
5.3	LCCL Compensation Network Sizing for Parallel Connected Multi-Pad Receiver	75
5.4	Primary Pad Self-Inductances	82
5.5	LCCL Compensation Values for the Primary Pad	85
5.6	Measured Leakage Field Values	92
6.1	Table showing the CISPR 11 limits for wireless power transfer [2].	100
6.2	CISPR 11 limits for harmonic band emissions for 85 kHz WPT in Japan [3].	101
6.3	Summary of how system attributes are affected by shielding methods.	111

LIST OF FIGURES

Figure Page

1.1 U.S. energy consumption by source and sector in 2019 [4]. 2

1.2 U.S. energy sources used by the transportation sector in 2019 [4]. 3

1.3 Share of U.S. GHG emissions by sector and vehicle class in 2018 [5]. 4

1.4 Tesla Model 3 LR charging profile on a V3 Supercharger [6]. 5

1.5 Li-ion battery capacity degradation with different C rates [7]. 6

1.6 Segmented coils used to demonstrate dynamic charging [8]. 7

1.7 Elongated rectangular track coil used for wireless charging [9]. 8

1.8 DWPT technology gap assessment and dissertation contributions. 13

2.1 Circuit diagram showing two loosely coupled coils. 17

2.2 Circuit diagram showing the primary LCCL resonant network in a WPT system. 20

2.3 Circuit diagram showing the secondary LCCL resonant network in a WPT system. 20

3.1 Circuit diagram showing two loosely coupled coils. 25

3.2 Circuit diagram showing a generalized multi-coil WPT system. 26

3.3 Example showing the coupling coefficient between one primary pad and one secondary pad in the system as a function of longitudinal misalignment. . . 28

3.4 Example showing the coupling coefficient between one primary pad and one secondary pad in the system as a function of time at different speeds. . . . 28

3.5 Flowchart showing the DWPT FEM and circuit modeling process. 29

3.6 ANSYS models showing the a) full coil model b) three-coil model and c) two-coil model for a DWPT system with $l_{tx} = 1400\,\text{mm}$. 33

3.7 Coupling factors between each primary and secondary pad using a) full coil model b) three-coil model and c) two-coil model for a DWPT system with $l_{tx} = 1400\,\text{mm}$. 34

3.8 Coupling factors between adjacent primary pads using a) full coil model b) three-coil model and c) two-coil model for a DWPT system with $l_{tx} = 1400\,\text{mm}$. 35

3.9 ANSYS models showing the a) full coil model b) three-coil model and c) two-coil model for a DWPT system with $l_{tx} = 700\,\text{mm}$. 36

3.10 Coupling factors between each primary and secondary pad using a) full coil model b) three-coil model and c) two-coil model for a DWPT system with $l_{tx} = 700\,\text{mm}$. 37

3.11 Coupling factors between adjacent primary pads using a) full coil model b) three-coil model and c) two-coil model for a DWPT system with $l_{tx} = 700\,\text{mm}$. 38

3.12 Examples of dependent voltage sources modeled in LTSpice to describe the behavior of DWPT pads. 40

3.13 Four transmitter pads and one receiver pad modeled as part of a DWPT system in LTSpice. 41

3.14 Top level PLECS schematic showing the three transmitter pad and three receiver pads modeled using the Roadway block. 42

3.15 PLECS schematic showing the elements inside the Roadway block. 42

3.16 PLECS schematics showing the primary side elements modeled inside the PSU block. 43

3.17 PLECS schematics showing the secondary side elements modeled inside the SecReg1 block. 43

4.1 Comparison of coil impedance before and after embedding the coil in concrete [10]. 45

4.2 Circular pad with single-nylon insulation being directly embedded in concrete [1]. 46

4.3 Rectangular pad with single-nylon insulation directly embedded in concrete [10]. 46

4.4 Litz wire with 2 mm TPE insulation used to construct the coils. 47

4.5 Scaled-down prototype of the coil designed to evaluate the performance of the TPE insulating jacket a) before concrete pour b) during concrete pour. 47

4.6 Variation in the prototype coil Q over a 68 hour time period from the start of concrete pouring. 48

4.7 Thermal image of the prototype pad when energized with nominal track current a) prototype with steel rebar b) prototype with fiberglass rebar. . . 52

4.8 Cross-sectional view of the primary coils and ferrite bars showing the three sample spacing configurations. 54

4.9 Loss distribution in the three sample ferrite bars simulated in ANSYS Maxwell. 54

4.10 Close-up image of the primary pad showing the effects of different ferrite spacing configurations a) normal image b) thermal image. 55

4.11 Cross-sectional view of the primary coils and ferrite bars. 55

4.12 Graph showing distribution of copper losses and core losses in the primary pad when the airgap size and position are varied while keeping the power transfer capability constant (ESR = 45 mΩ). 56

4.13 Graph showing distribution of copper losses and core losses in the primary pad when the airgap size and position are varied while keeping the power transfer capability constant (ESR = 110 mΩ). 56

4.14 Cross section of a CF139 ferrite bar covered in PCM. 57

4.15 Required DWPT power level to achieve unlimited range using the HWFET drive cycle [11]. 59

4.16 Two-meter long concrete-embedded pad prototype. 59

4.17 System block diagram showing the circulating power test setup. 60

4.18 Hardware test setup for testing the WPT system and the corresponding power electronics. 61

4.19 Graph showing the DC-DC efficiency at various output power levels. 62

4.20 Scope waveforms showing the inverter output voltage, track current, and DC output current in the system. 62

4.21 Three concrete-embedded 1 m x 1 m pad prototypes a) before concrete pours b) after concrete pours. 63

4.22 Hardware test setup for testing the WPT system and the corresponding power electronics. 64

4.23 Variation in pad Q over the duration of the fatigue cycling tested at a) 32 kip b) 50 kip c) 64 kip. 65

4.24 Test setup used for the three-point bending test a) before pad failure b) after pad failure. 66

4.25 Frequency sweep measurement of the concrete-embedded pad impedance before and after 3-point bending test failure. 67

4.26 Q measurement during the 3-point bending test. 67

5.1 Dynamic profiles for coupling coefficients between primary pads and secondary pads. 70

5.2 Multi-pad receivers operating as independent receivers. 71

5.3 Multiple receivers connected in a) parallel and b) series. 72

5.4 DWPT system modeled in ANSYS Maxwell for FEM simulation. 76

5.5 DWPT system modeled in PLECS for circuit simulation. 77

5.6 H-bridge inverter and rectifier model in LTSpice to simulate the WPT system. 78

5.7 Primary and secondary resonant tank model with constant coupling coefficient. 78

5.8 Series connected three-pad receiver a) PLECS schematic b) V_{oc} waveform. . 79

5.9 Parallel connected three-pad receiver a) PLECS schematic b) V_{oc} waveform. 79

5.10 Wireless power transfer system overview. 80

5.11 Simulated battery current waveforms showing dynamic power transfer to the multi-pad receiver. 81

5.12 System overview with three transmitter pads and a three-pad receiver. . . . 82

5.13 Hardware used for the vehicle detection system. 83

5.14 Three receiver pads connected in series with compensation capacitors - top view. 84

5.15 Series compensation capacitors mounted under the primary pad. 84

5.16 Three primary pads potted and placed in the outdoor trench. 85

5.17 Primary side electronics and compensation network. 86

5.18 Three receiver pads and series compensation capacitors mounted to the EV - bottom view. 87

5.19 Secondary side electronics and compensation network inside the vehicle. . . 87

5.20 Hardware DWPT system overview. 88

5.21 Scope waveforms showing inverter output current, output voltage and track current through the primary pad. 89

5.22 View of the test setup inside the shed. 89

5.23 Single primary pad energized: a) Simulated V_{oc} profile b) Measured V_{oc} profile. 90

5.24 Two primary pads: a) Simulated V_{oc} profile b) Measured V_{oc} profile. 90

5.25 Field probe in a) position 1 outside the RAV4 EV b) position 2 on the driver seat inside the RAV4 EV c) position 3 beside the receiver power electronics inside the RAV4 EV. 91

5.26 Scope waveforms showing inverter output current, output voltage and input DC current. 93

5.27 Primary side waveforms showing inverter (bridge) output voltage and current along with the track current. 93

5.28 Secondary side measured battery current and battery voltage showing a) 29.6 kW delivered to the battery at 7 mph vehicle speed b) 29.8 kW delivered to the battery at 22 mph vehicle speed. 94

5.29 Scope waveforms showing inverter output voltage for all three primary pads. 95

5.30 Scope waveforms showing primary pad currents and total input DC current at 7 mph and a peak power transfer of 29.6 kW to the vehicle battery. . . . 96

5.31 Scope waveforms showing inverter output voltages and input DC currents for all three primary pads at 22 mph vehicle speed and a peak power transfer of 29.8 kW to the vehicle battery. 97

5.32 Scope waveforms showing the three primary track currents at 22 mph vehicle speed using automated system turn-on. 97

6.1 Image of Booster Coil pads in the outdoor trench. 102

6.2 Image of Booster Coil pads modeled in ANSYS. 103

6.3 Adaptive meshing across a test plane showing the mesh shape. 103

6.4 Plots showing leakage magnetic field along a) test lines 1 and b) test line 3. 104

6.5 Plot showing leakage magnetic field along the test line 2 105

6.6 LTSpice simulation used to obtain the amplitude and phase of the current excitations. 105

6.7 ANSYS model with the receiver in a) position 1 b) position 2 and c) position 3. 107

6.8 Leakage field comparison on test plane with receiver pad in a) position 1 b) position 2 and c) position 3. 108

6.9 Active cancellation for primary and secondary pads. 109

6.10 Leakage field comparison on test plane with a) no cancellation b) active cancellation and phase-shift control c) active cancellation and DC-DC control. 110

ACRONYMS

AC	alternating current
AWG	american wire gauge
CP	circular pad
DC	direct current
DD	double-D pad
DIPT	dynamic inductive power transfer
DWPT	dynamic wireless power transfer
EMC	electromagnetic compatibility
EMF	electromagnetic field
ESR	equivalent series resistance
EV	electric vehicle
FEM	finite element method
GA	ground assembly
GHG	green house gas
GSSA	generalized state space averaging
ICE	internal combustion engine
IPT	inductive power transfer
PCM	phase change material
SOC	state of charge
TPE	thermoplastic elastomer
VA	vehicle assembly
V2G	vehicle-to-grid
V2I	vehicle-to-infrastructure
V2V	vehicle-to-vehicle
WPT	wireless power transfer
XFC	extreme fast charging

CHAPTER 1

INTRODUCTION

1.1 Background

In 2019, transportation accounted for 28% of the total energy consumption of the United States (U.S.). Approximately 91% of this energy demand is fulfilled using petroleum sources and powers internal combustion engine (ICE) vehicles, leading to a significant amount of tailpipe emissions [12]. This can be seen in a visual representation of the 2019 U.S. energy consumption by source and sector as shown in Fig. 1.1. With the U.S. government setting aggressive climate change goals and targeting a reduction in greenhouse gases [13], electric vehicles (EVs) are seen as a key component in the global effort to improve air quality [14]. Electric vehicles (EVs) are considered a paradigm-shifting technology due to their untapped potential for environmental and economical impact. Regardless of how the electricity for EVs is produced, EVs have a significantly higher energy efficiency than traditional gasoline-powered vehicles. Data obtained from Oak Ridge National Lab and Idaho National Lab estimate EVs to have an energy efficiency of 77% and traditional ICE vehicles a 12-30% energy efficiency [15]. This shows that the total energy required by the transportation industry in the U.S. can be cut by 62% to 85% if all the gasoline powered transportation is converted to electric.

1.1.1 The Need for Transportation Electrification

Societal Benefits

On a societal level, mass adoption of EVs and transportation electrification improves the air quality in and around areas of high population density. Typically these population centers suffer from poor air quality issues due to the high concentration of vehicular traffic.

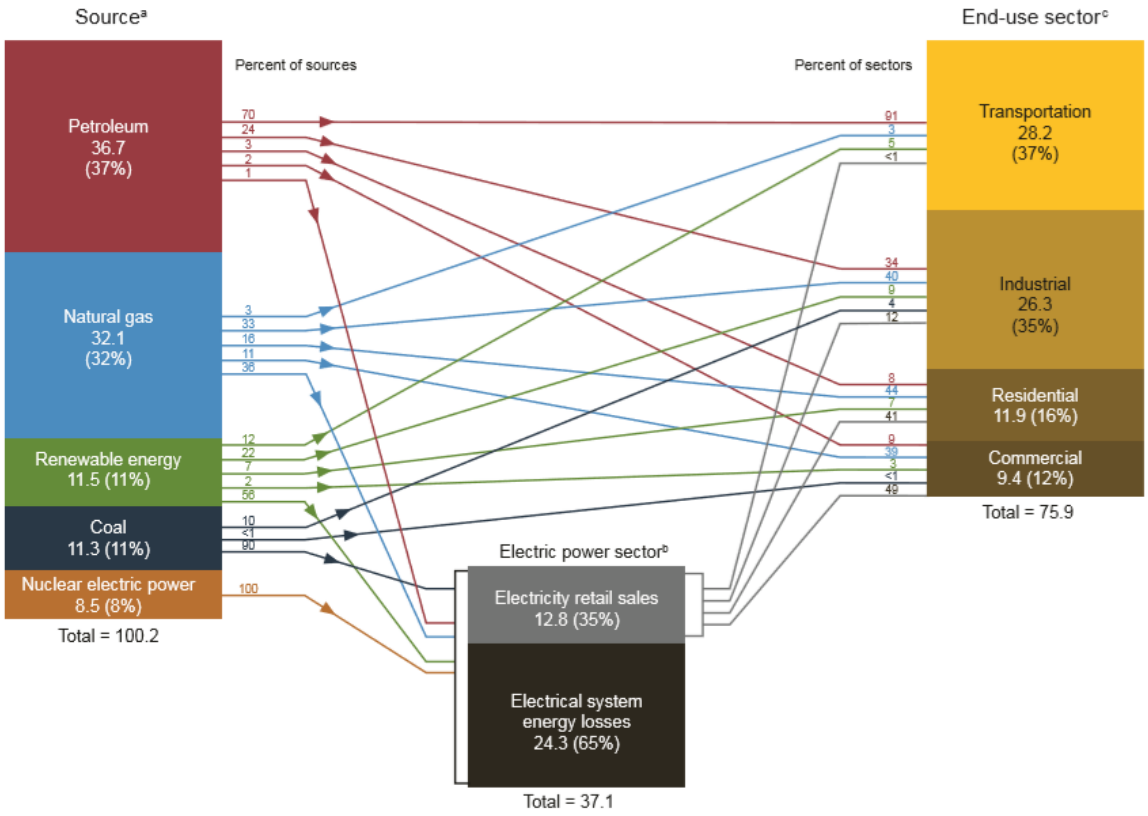

Fig. 1.1: U.S. energy consumption by source and sector in 2019 [4].

While ICE vehicles are not the only cause of poor air quality in urban population centers, tailpipe emissions are considered to be a major contributor [5].

Higher market penetration of EVs and alternate fuel vehicles (bio-diesel, natural gas, hydrogen etc.) provides the economy with much needed diversification in transportation energy consumption. In the United States for instance, with transportation accounting for a major portion of the energy consumption needs, a gradual shift to EVs helps balance the energy pie chart shown in Fig. 1.2 and move away from petroleum products. A wide variety of sources are available for the generation of electricity, including coal, natural gas, nuclear, solar, and wind. This can help countries reduce their reliance on the global supply of crude oil.

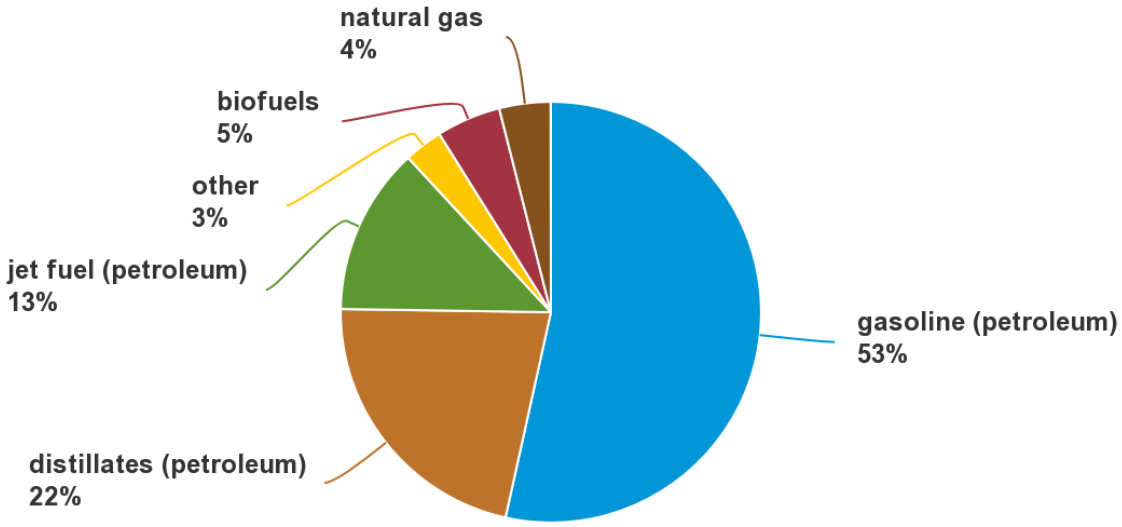

Fig. 1.2: U.S. energy sources used by the transportation sector in 2019 [4].

Benefits of EV Ownership

Companies and individuals who own EVs can expect significant short-term and long-term benefits. Studies [16] indicate that fleet electrification helps companies reduce total cost of ownership in addition to achieving their sustainability and environmental goals. Further, they provide a hedge against fluctuating oil prices and future national and international policy regulations [17]. This in turn helps companies reduce some of the uncertainty in estimating future growth and profits [17, 18].

EVs offer the benefit of custom range vehicles based on the application they're being used for. For instance, a delivery truck in a dense urban location such as Manhattan driving an average of 18-20 miles a day can be designed with a lighter battery pack, reducing vehicle cost and increasing the weight capacity.

On an individual level, EV ownership provides cost savings due to the lower electricity prices and the convenience of charging at home or at the workplace. With the increasing adoption of solar energy and DC micro-grid technologies, an initial investment could provide energy to recharge vehicles at almost no additional cost to the consumer.

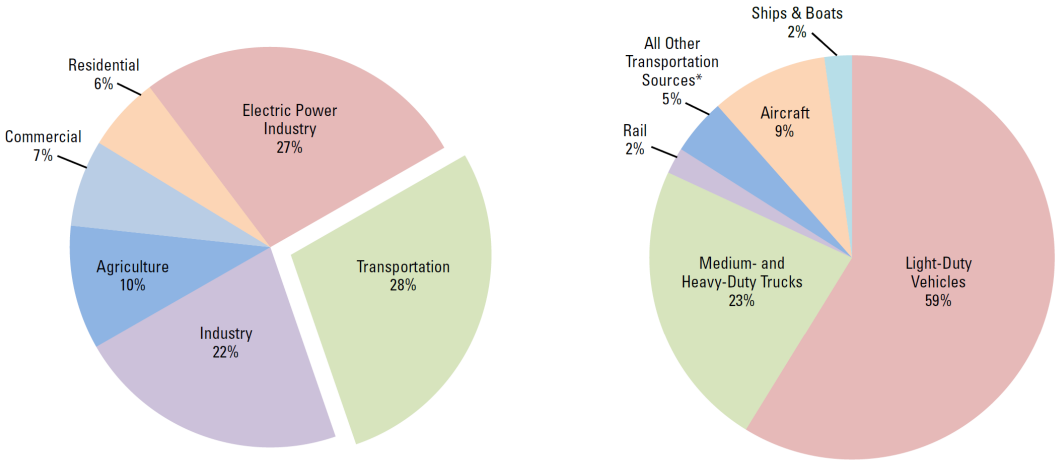

Fig. 1.3: Share of U.S. GHG emissions by sector and vehicle class in 2018 [5].

1.1.2 Challenges Facing the Mass Adoption of Electric Vehicles

Mass adoption of EVs refers to the scenario where a significant percentage of the vehicles on the road are electric. Despite the potential benefits of transportation electrification and mass adoption of EVs, there are a few challenges on the road to mass adoption. While the range and cost of present day (2021) consumer EVs is almost comparable to ICE vehicles, the issue of refuelling (recharging) times still remains.

For instance, a road trip from Los Angeles to Salt Lake City (708 miles) takes 19% longer to complete and requires 66% more fuel (charging) stops when a long range Tesla Model 3 is used over an ICE vehicle with the same range of 353 miles (Model 3 trip details calculated using [19]). While this does relate to range anxiety, at its core, it is an issue of slow recharging times. While it is practically impossible to reach the same refuelling (recharging) speed as gasoline using current battery technology, the issue can be partially addressed using existing technologies. Two possible solutions to this issue are the deployment of extreme fast chargers (XFC) [20–22] and in-motion charging technologies [9, 23–25]. Extreme fast chargers (XFCs) work on the same concept as a fueling station and require the vehicle to stop and recharge as and when the battery state-of-charge (SOC) drops below a certain range. While XFC technology is easier to deploy and is already commercially available from some automakers [26, 27], there are certain drawbacks that limit the capabilities of

this technology. One prominent drawback is the current day battery technology and its inability to maintain a high rate of charge over the entire SOC range. Fig. 1.4 shows this phenomenon using real world data from a supercharger. It can be seen that the full charging power of 250 kW is only available for a small and impractical SOC range due to the charging profile of the vehicle battery. Another potential drawback is the impact high C rate charging has on battery life. Authors in [7] experimentally validate the degradation of Li-ion batteries at different C rates. Fig. 1.5 shows that the frequent charging at higher C rates increases the rate at which the Li-ion battery degrades. Therefore, XFC technology by itself can not fully solve the issues of range anxiety and refueling (recharging) times.

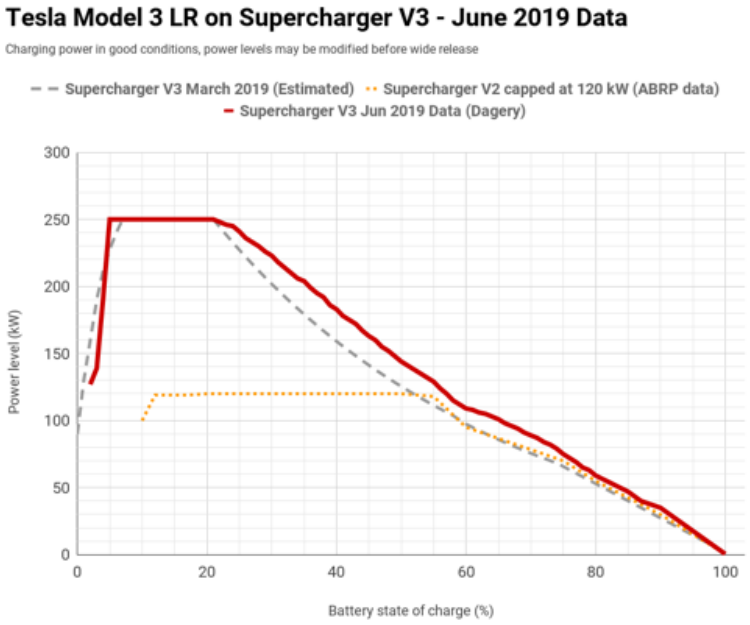

Fig. 1.4: Tesla Model 3 LR charging profile on a V3 Supercharger [6].

The second possible solution is to use in-motion charging technologies to dynamically charge EVs without the need for frequent charging stops. In-motion charging opens up a wide range of possibilities that were previously not thought possible, such as quasi-dynamic charging at intersections and traffic lights, and in-motion vehicle-to-grid (V2G) energy transfer. Fixed route applications such as transit buses can make use of in-motion charg-

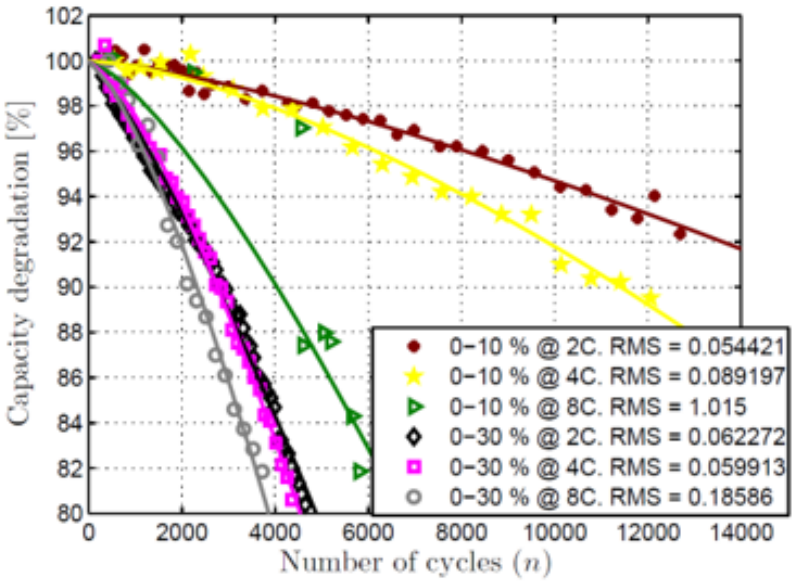

Fig. 1.5: Li-ion battery capacity degradation with different C rates [7].

ing technologies to drastically reduce the on-board battery pack and improve passenger capacity or decrease their energy consumption per mile. Other applications include drayage trucks, warehouse vehicles, and industrial robots. With automakers racing toward level 5 autonomy, the refueling (recharging) aspect of the vehicle still requires human intervention. Using WPT technologies, autonomous EVs would be able to recharge automatically without human interaction. With the availability of wireless charging units on vehicles, additional range benefits and smaller battery packs become even more practical with the adoption of DWPT technologies.

Therefore, a good mix of wired XFC and DWPT technologies is seen as the catalyst to overcome the issues of "range anxiety" and move towards the mass adoption of EVs. This dissertation focuses on the dynamic wireless power transfer (DWPT) solution and aspects related to the practical deployment of DWPT technologies.

1.2 Review of Existing Research

1.2.1 Pad Designs

The transmitter and receiver pads are key components in wireless charging systems. Depending on the context and application, other terms used to describe the power transmitter and receiver pads are given in Table. 1.1.

Table 1.1: Nomenclature used to describe inductive WPT pads.

Transmitter Pad	Receiver Pad
Primary Pad	Secondary Pad
Track	Pick-up
Ground Assembly	Vehicle Assembly

Prior research works [23, 28–39] on pad designs have explored a variety of coil shapes and ferrite arrangements in order to achieve application specific objectives. These objectives include horizontal and vertical misalignment tolerance, reducing leakage magnetic fields, increasing the ferrite utilization, and increasing power transfer capability to name a few.

The dynamic wireless charging systems implemented in prior research typically consist of an elongated transmitter pad [40] or smaller segmented transmitter pads [8, 28] powering one or more receiver pads as seen in Fig. 1.6 and Fig. 1.7.

Fig. 1.6: Segmented coils used to demonstrate dynamic charging [8].

Fig. 1.7: Elongated rectangular track coil used for wireless charging [9].

Authors in [41] explore the use of a dual-phase bipolar track (BPT) to ensure interoperability with square/circular (CP) and Double-D (DD) standard receiver pads. Various trade-offs with the BPT transmitter and CP and DD receivers are analyzed. The authors in [28] develop a modified segmented rectangular pad design with overlapping coils to address the issue of pulsating dynamic power profiles caused by a drop in coupling coefficient when transitioning from one transmitter pad to another. This is a challenge that multiple research groups have run into and tried to address by modifying the pad shapes [35, 36], adding additional reactive elements to the system [8] and developing new ways to control the system [42–44]. The proposed solutions with overlapping coil designs [28, 41] restrict the use of modular transmitter pad units. For a large scale deployment of road-embedded chargers, a modular system offers installation and maintenance benefits.

To overcome this challenge of pulsating power profiles without compromising on the modularity of the system, the authors in [23] have proposed a Booster Coil ground assembly (GA) design. Some of the challenges with this design and proposed solutions are addressed in Section 6.4.

1.2.2 Power Electronics

Research on power electronics in WPT systems is focused on the DC/AC conversion, AC/DC conversion, auxiliary DC/DC conversion [45] and the design of various compensation networks [46, 47]. A majority of DWPT systems make use of a full-bridge phase shifted inverter and a diode bridge rectifier as the DC/AC and AC/DC conversion com-

ponents respectively. Authors in [48] propose a secondary-side control method for power control and efficiency maximization is achieved using a Half Active Rectifier. Energy efficiency improvements are typically achieved by actively controlling the turn-on and turn-off of different transmitter pads in a DWPT system with multiple transmitter pads [25, 28, 43]. Authors in [42] propose an auto-tuning control system to detect the presence of a receiver pad and turn the corresponding transmitter pads on using the variation in self-inductance of the transmitter pad, without the use of additional sensors. Authors in [49] present an optimal frequency tracking scheme to maximize the infrastructure utilization and make use of phase shift control to regulate the output voltage. The system designed in [50] presents the use of a front-end DC/DC buck converter powering a push-pull converter. This system is intended for use in a DWPT scenario due to its tolerance to mistuning and coupling factor between the primary and secondary pads. Authors in [51] analyze an LCCL tuning network and show how the system robustness is improved when compared to other compensation networks.

Other works like [52] explore the transfer of power and information together by using a trapezoidal current waveform controlled by phase-shift modulation. Authors in [53] present the design of a dual-output inverter topology to power two different primary pads in a segmented pad DWPT system independently if needed. Few of the prior works also discuss the concepts of multi-phase transmitter and receiver pads [31, 35, 44, 54, 55].

Other research works on WPT systems include current fed systems [56, 57], and synchronous rectifiers [58, 59]. Current and future research direction in this field is focused on reducing system costs [60], improving reliability and cybersecurity [61].

1.2.3 Pavement Integration

Prior works in pavement integration discuss some of the design challenges with constructability of concrete and asphalt-embedded pads [1, 10, 41, 62–67]. Depending on the geographical location of the research group, and local pavement construction methods, the authors explore pavement-embedded transmitter pads in asphalt or concrete.

The concept of magnetizable concrete has been explored in [62, 63] to embed wireless

charging infrastructure into roadways and enable dynamic wireless charging. Works in [1,64] show that regular construction methods can not be integrated directly when constructing pavement-embedded charging pads due to the limitations of the charging pads. For example, authors in [64] use a specialized cement asphalt mortar (CAM) mix instead of hot mix asphalt due to the high temperatures in the process. In [1], a flowable mix with only sand aggregate is used so that a uniform composition of the concrete slab can be achieved. This is due to the limitations of the wireless charging pad used in the work. The densely packed coil turns restrict the flow of concrete and prevent the use of larger aggregate particles which are typically used in concrete pavement construction. Authors in [65] develop numerical models to analyze the impact of embedding wireless charging pads inside pavements and to estimate the structural consequences of doing so. Researchers in [66] evaluate the thermal characteristics of a WPT pad to estimate how losses in the coil and ferrite affect the system performance when there is limited airflow available.

Authors in [67] analyze the construction of steel-reinforced concrete pavement slabs and the power dissipation of WPT systems. The eddy current loss in the reinforcement steel rebar is identified as the largest individual source of loss in the system. The authors suggest methods to redesign the steel reinforcement structure to break the eddy current loops by using carved bars. While this method helps in reducing losses in the rebar, it increases the construction complexity due to the need for custom rebar mats, which in turn increases the total system cost and construction time.

1.2.4 System Modeling

Stationary inductive power transfer systems have been extensively studied analytically and modeled in prior works [68, 69]. While stationary circuit models provide an insight into the system operation at individual operating points, they cannot be used to accurately model the inter-dependent effects between multiple primary pads and related power electronics hardware in dynamic operation. Prior research works [70–74] have explored analytically modeling the transient effects observed in dynamic wireless power transfer systems.

The authors in [70, 71] develop a simplified model that accurately models well-tuned

systems, but does not account for system mistuning which is very likely in DWPT systems. Authors in [75] present the direct envelope modeling of an LCCL tuned resonant WPT system by decomposing the inverter output into its fundamental frequency and two dominant side bands. The authors in [76] model the dynamic nature of coupling as a step change in input voltage and design a closed loop controller to stabilize the output voltage. This method fails to take into account the effect of vehicle speed on the dynamics of the controller and the effects of induced voltages from the neighboring pads. The authors in [40] present a comprehensive analysis of a specific WPT system using the generalized state space averaging (GSSA), which can be used to model converter dynamics when the coupling coefficient remains constant. Authors in [77] model the dynamic behavior by estimating the mutual inductance in real time. Authors in [73] also use GSSA and small-signal models to analyze the steady-state and transient system responses considering a constant coupling factor. An envelope model of the turn-on transient is developed analytically. The design of the DWPT system presented in [72, 73] makes use of the GSSA method and implements a dual loop controller. The simulations presented in [72] are limited to one transmitter pad and one receiver pad. Further, the dynamic behavior of the secondary pad and vehicle is modelled as a time varying load resistance profile and the exact variation in coupling coefficient between the pads is not taken into account.

1.2.5 Feasibility Studies

The economic feasibility of new technology is an important aspect of research to understand the value a particular technology brings to society. Prior works have analyzed the economic impact of transportation electrification and the usefulness of in-motion charging technologies.

A report by logistics company UPS and Greenbiz [16] discusses the need for fleet electrification and some of the challenges faced in achieving this goal. Multiple studies conducted by the Electrification Coalition [17, 18, 78–80] discuss various real world case studies and scenarios where transportation electrification makes economic sense. Aspects such as total cost of ownership, vehicle maintenance and support savings, and the need

for charging infrastructure are highlighted in a collaborative study with logistics company FedEx [18].

Authors in [81] develop a mathematical model to evaluate the cost of electrification for a bus route in New Zealand. The costs and benefits associated with the installation of a dynamic IPT system are presented in this work. The optimal placement of chargers along a bus route is shown to help optimize battery pack sizing. With power companies adopting a demand pricing model, the price of electricity varies according to the time of day. The optimal charging time and route scheduling problem is explored in this context in [82]. The optimization shows that a reduction in battery size is possible with an optimal charging schedule for wirelessly charged electric buses. The optimal scheduling is made possible due to the availability of wireless charging, instead of the electric bus having to return to the bus station to take advantage of off-peak pricing.

Authors in [83] discuss the various challenges facing DWPT technologies including vehicle to infrastructure (V2I) communications and reducing the leakage EMF to satisfy current safety standards. Authors in [11] present the power consumption model of an EV and present a simulation analysis on the trade-offs between a standalone charging option versus a combination of dynamic and quasi-dynamic wireless charging system. The study concludes that deploying a combination of charging systems at an optimal road coverage level can achieve unlimited range for light duty vehicles. This work also addresses some challenges with the safety concerns regarding human exposure to magnetic fields. Authors in [84] suggest a solution for increasing the driving range of EVs by using vehicle to vehicle (V2V) communication and dynamic wireless charging technology. The increase in driving range is achieved by route optimization using a combination of static charging systems and dynamic charging. Research presented in [85] explores the use of bidirectional quasi-dynamic wireless charging at traffic intersections to increase EV range in city driving scenarios and the possibility of vehicle-to-grid (V2G) services.

Authors in [86, 87] explore detailed models for DWPT installation and provide recommendations on a power level that can satisfy the energy needs for multiple vehicle classes,

thereby improving infrastructure utilization. The authors also recommend the use of multiple receivers to increase the power received.

1.3 Problem Statement

Dynamic wireless power transfer (DWPT) refers to the set of technologies that enable in-motion charging of electric vehicles. The current work specifically deals with dynamic inductive power transfer (DIPT). DWPT and DIPT are used interchangeably in this dissertation. The high initial construction cost, integration with existing roadways and infrastructure utilization are seen as the major challenges that need to be addressed. Further, the time taken to test and develop these systems can be quite a hassle due to the cost of construction and the real world testing required to validate the power electronics and coil designs. An overview of the problem statement and proposed contributions is shown in Fig. 1.8.

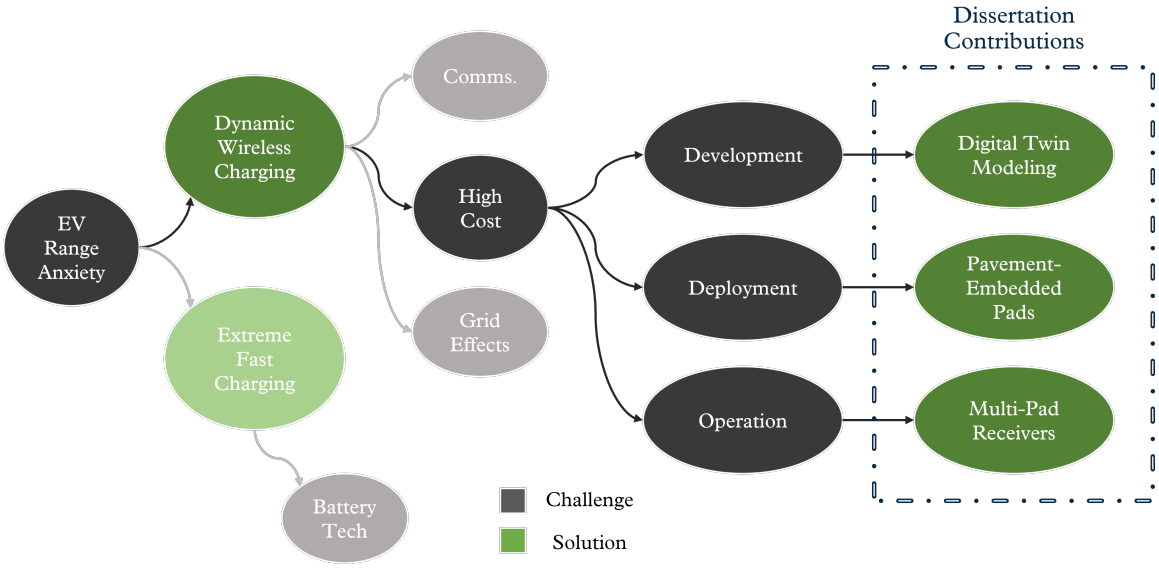

Fig. 1.8: DWPT technology gap assessment and dissertation contributions.

1.4 Contributions

To address the aforementioned issues, the current work:

- Models a digital-twin DWPT system that can be used to rapidly evaluate new coil designs, tuning networks and power electronic topologies, thereby reducing the time taken to design and develop these systems.

- Presents the design and pavement integration of DWPT transmitter coils and related power electronics hardware. Pavement integration allows different vehicle classes to utilize the infrastructure without sacrificing their available ground clearance.

- Presents the design and validation of multi-pad receivers to enable modularity and scalable power levels. This results in higher utilization of the charging infrastructure since different vehicle classes with different power levels can make use of the same charging infrastructure to receive power wirelessly.

1.5 Dissertation Organization

This dissertation is organized as follows:

- Chapter 2 discusses the basic principles behind wireless power transfer, the process of designing a practical dual-LCCL WPT system, and presents a brief discussion on how power levels are classified in this work.

- Chapter 3 presents the modeling approach used to model various transmitter and receiver topologies and simulate their working and dynamic operation. Detailed modeling procedures are presented for magnetic FEM modeling in ANSYS Maxwell and circuit modeling in LTSpice and Plexim PLECS software.

- Chapter 4 covers the design and analysis of roadway-embedded transmitter coils, including the design considerations for concrete-embedding of power electronics. This chapter also includes details about the designed hardware and test results obtained from validation testing.

- Chapter 5 covers the design and analysis of multi-pad receiver systems. Real-world hardware tests are performed to validate the operation of multi-pad receivers with DWPT transmitters.

- Chapter 6 presents the safety and compliance requirements for WPT systems and how they can be applied to DWPT systems. A simulation analysis is performed to evaluate methods to reduce leakage magnetic fields in a sample DWPT system.
- Chapter 7 concludes the dissertation and briefly discusses the direction of future research.

CHAPTER 2

DYNAMIC WIRELESS POWER TRANSFER

2.1 Inductive Power Transfer

Inductive power transfer can fundamentally be described using Ampere's law and Faraday's law. A time-varying current (AC) flowing in the primary coil generates a time-varying magnetic flux as described by Ampere's law. When the secondary coil is in the vicinity of the primary coil, the time-varying magnetic flux induces a voltage on the secondary coil as described by Faraday's law. The differential forms of Ampere's and Faraday's laws are given in (2.1) and (2.2) [47].

$$\nabla \times \boldsymbol{H} = J + \frac{\partial \boldsymbol{D}}{\partial t} \tag{2.1}$$

$$\nabla \times \boldsymbol{E} = -\frac{\partial \boldsymbol{B}}{\partial t} \tag{2.2}$$

where $\boldsymbol{H}$ and $\boldsymbol{E}$ are the vector magnetic field intensity and electric field intensity respectively. The magnetic flux density and the electric flux density are represented by $\boldsymbol{B}$ and $\boldsymbol{D}$ respectively. And the current density is represented by $\boldsymbol{J}$.

Inductive power transfer coils are in essence inductors whose magnetic flux links with each other when they are in each other's vicinity. The self-inductance of a magnetic structure is defined as the ratio of total flux linkage to the current that generates the flux [88].

$$L_{self} = \frac{N\phi}{I} \tag{2.3}$$

where I is the excitation current generating the flux, ϕ is the total flux generated by the coil and N represents the number of turns in the structure. It should be noted that (2.3) is valid only under the assumption that the total flux links with each of the N turns.

Since ϕ is directly proportional to the number of turns in the magnetic structure, L_{self} is proportional to N^2. In a wireless inductively coupled system of coils, the magnetic flux generated by the primary coil links to the secondary coil. This mutual flux linkage ϕ_{12} gives rise to mutual inductance M_{12} between the two coils. This characteristic of an inductive charging system is often represented using the coupling coefficient k_{12}, where k_{12} and M_{12} are related as follows [89]

$$k_{12} = \frac{M_{12}}{\sqrt{L_1 L_2}} \tag{2.4}$$

where L_1 and L_2 are the self-inductances of the primary and secondary coils respectively.

Inductive wireless power transfer systems are typically modeled as a loosely coupled transformer as shown in Fig. 2.1. A single transmitter and single receiver is shown in this case.

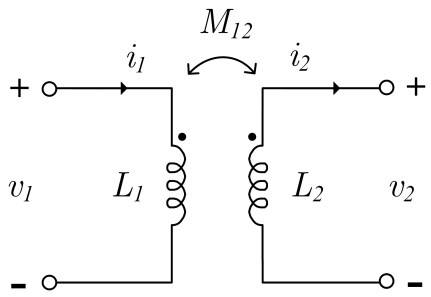

Fig. 2.1: Circuit diagram showing two loosely coupled coils.

where the corresponding voltages and currents are related as follows

$$v_1 = L_1 \frac{di_1}{dt} + M_{12} \frac{di_2}{dt} \tag{2.5}$$

$$v_2 = L_2 \frac{di_2}{dt} + M_{12} \frac{di_1}{dt} \tag{2.6}$$

where L_1, L_2 and M_{12} are the self-inductances of the primary and secondary coils and the mutual inductances between the two coils respectively.

The equations can be represented in matrix form as follows

$$\begin{bmatrix} v_1 \\ v_2 \end{bmatrix} = \begin{bmatrix} L_1 & M_{12} \\ M_{12} & L_2 \end{bmatrix} \begin{bmatrix} \frac{di_1}{dt} \\ \frac{di_2}{dt} \end{bmatrix} \tag{2.7}$$

One significant difference between an inductive power transfer system and a transformer is the large leakage inductance present due to the lack of a low reluctance path between the coils. This leakage inductance is compensated by the use of capacitors in compensation networks. In case of WPT systems transferring more than a few watts, these compensation networks are also utilized to create a resonant condition and maximize power transfer. This is commonly referred to as resonant inductive power transfer. Since IPT in the context of electric vehicles is typically in the order of kilowatts, inductive power transfer in this dissertation refers to resonant inductive power transfer. One common compensation network used in practice is the LCC or LCCL resonant network [90]. The design of a system with dual-LCCL resonant compensation networks is presented in the following section.

2.2 Dual-LCCL System Design Methodology

A wide variety of resonant networks are available for WPT systems depending on the system requirements [47, 91]. WPT and DWPT systems make use of the LCCL resonant network due to its desirable current source characteristics and load-independent output current. Further, the LCCL compensation networks allow for zero coupling, which is an important passive safety feature for DWPT systems. Consequently, this work makes use of the dual-LCCL resonant networks in the works presented in Chapters 4 and 5. This section presents the design procedure used to select the component values and system parameters using a full-bridge inverter.

In many practical DWPT systems, the output power level is the primary design specification around which the system is designed. The output power of an inductive WPT

system is given by

$$P_{out} = QS_u \tag{2.8}$$

where Q is the loaded quality factor of the system and S_u is the uncompensated power [68]. The S_u can be calculated as follows

$$S_u = \omega I^2 k^2 L_{pad} \tag{2.9}$$

where I is the current flowing through a primary coil with self-inductance L_{pad} and ω is the angular frequency of the excitation current given by (2.10).

$$\omega = 2\pi f \tag{2.10}$$

where f is the fundamental frequency of the primary coil excitation. And the coupling coefficient between the primary and secondary coils is represented by k.

Based on the thermal limitations of the system and availability of Litz wire, an upper limit on the track current value I can be established. This limit also depends on the intended system operation. For instance, with DWPT systems, each coil is energized for a brief period of time when a vehicle passes over and then turned off until the next vehicle arrives. In case of stationary WPT systems, the coils need to be designed for continuous operation.

Using (2.8) and (2.9), the required coupling k and L_{pad} are design parameters that are chosen based on the air-gap and vehicle size. When standardized primary or secondary pads are used, then available design parameters are adjusted to achieve the required power transfer. Typically, a misalignment tolerance specification is also desired. The system is then designed to achieve the rated power at the worst case misalignment and the power transfer is modulated at better misalignments using the DC/AC, AC/DC or DC/DC power converters in the system.

The choice of DC link voltage V_{DC} on the primary side depends on the available DC supply or grid converter and the system design can be adjusted accordingly. The

equivalent primary side circuit model with three impedances can be seen in Fig. 2.2. The network formed by Z_{br} and Z_{par} circulates the higher order harmonics of the system and the fundamental frequency sinusoidal is fed into the series combination of Z_{ser}, which is a series combination of L_{pad} and C_{ser}.

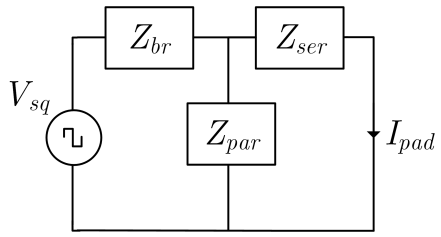

Fig. 2.2: Circuit diagram showing the primary LCCL resonant network in a WPT system.

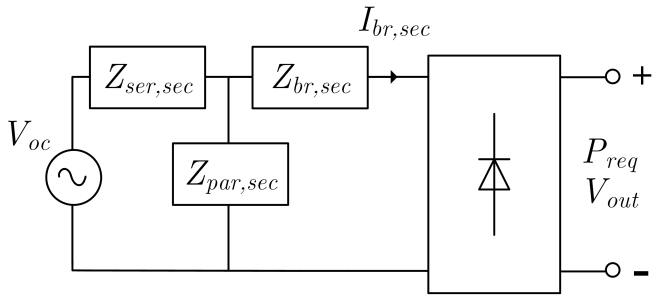

Fig. 2.3: Circuit diagram showing the secondary LCCL resonant network in a WPT system.

The value of Z_{br} is determined as shown in (2.11) and Z_{par} is set to resonate with Z_{br} as shown in (2.13).

$$\|Z_{br}\| = \frac{V_{DC}}{I} \tag{2.11}$$

$$L_{br} = \frac{\|Z_{br}\|}{\omega} \tag{2.12}$$

$$Z_{br} = -Z_{par} \tag{2.13}$$

C_{par} can then be calculated as follows

$$C_{par} = \frac{1}{\omega \| Z_{par} \|} \tag{2.14}$$

The series capacitor C_{ser} is used in LCCL resonant network to compensate the inductance of the primary pad and reduce voltage on the C_{par} capacitor bank. The value of C_{ser} can be calculated as follows

$$C_{ser} = \frac{1}{\omega(\| Z_{pad} \| - \| Z_{ser} \|)} \tag{2.15}$$

where

$$\| Z_{ser} \| = \| Z_{br} \| = \| Z_{par} \| \tag{2.16}$$

$$\| Z_{ser} \| = \omega L_{pad} \tag{2.17}$$

Similarly on the secondary side, the desired input current to the AC/DC full bridge rectifier is determined based on the output power required and the DC output voltage. This voltage is typically an input to a DC/DC converter interfaced to the vehicle battery pack. The equivalent circuit of the secondary side, used for analysis is shown in Fig. 2.3. When a diode bridge rectifier is used, the secondary bridge current is calculated as follows

$$I_{br,sec} = \frac{\pi}{2\sqrt{2}} \frac{P_{req}}{V_{out}} \tag{2.18}$$

where P_{req} is the output power required and V_{out} is the output voltage of the AC/DC diode bridge rectifier. The $Z_{ser,sec}$ impedance can then be calculated as shown

$$\| Z_{br,sec} \| = \frac{V_{oc}}{I_{br,sec}} \tag{2.19}$$

where V_{oc} is the open circuit induced voltage on the secondary pad, calculated as follows

$$V_{oc} = j\omega M I \tag{2.20}$$

where M is the mutual inductance between the primary and secondary pad. The other elements of the LCCL resonant network are calculated similar to the primary side as follows

$$C_{ser,sec} = \frac{1}{\omega(\|Z_{pad,sec}\| - \|Z_{ser,sec}\|)} \tag{2.21}$$

$$\|Z_{ser,sec}\| = \|Z_{br,sec}\| = \|Z_{par,sec}\| \tag{2.22}$$

where $Z_{ser,sec}$, $Z_{br,sec}$, $Z_{par,sec}$ and $Z_{pad,sec}$ are the corresponding secondary side LCCL impedances.

2.3 Power level definitions

Power level definitions are arbitrary and change over time as technology further evolves. This section classifies the power levels based on the respective functionality offered.

- 1 kW - 7 kW

  Used for low power industrial robots and small machinery. Impractical for roadway DWPT due to the infrastructure cost and the return on investment.

- 7 kW - 30 kW

  Can be used to charge EVs in a drive-thru or at a traffic light. Includes quasi-dynamic charging offered as a convenience to the customer. Higher end of this range can also be used for fixed route EVs such as transit buses.

- 30 kW - 80 kW

  Power level which can enable roadway dynamic charging with current battery technology and cost of electrification. Potential battery size reduction depends on the percentage of roadways that are electrified. Larger vehicles can make use of multiple receivers to scale up the received power.

- 80 kW - 200 kW

High power level which can reduce the percentage of roadways that need to be electrified. With current battery technology, constant charging at these power levels could result in a decrease in battery capacity.

- 200 kW+

  Extreme fast charging power levels. Possible application includes robo-taxi autonomous recharging or semi-truck recharging, where higher EV utilization is more important than the battery degradation effects due to the higher rate of charge.

CHAPTER 3

MODELING DYNAMIC WIRELESS POWER TRANSFER SYSTEMS

3.1 Challenges in Modeling DWPT Systems

Dynamic wireless power transfer systems involve high upfront infrastructure costs and can benefit from a digital-twin approach in design. Digital-twin system models are designed to save time and cost during the development and fine-tuning of resource-intensive technologies. A comprehensive digital-twin model of a DWPT system should include the following:

- FEM simulation model to determine the electro-magnetic characteristics
- Circuit simulation model to determine the electrical characteristics of the system
- Mechanical models to model the thermal and structural aspects of the system
- Multi-physics models to model the interactions between the thermal and electrical characteristics
- Accurate material models to understand the behavior of the surrounding environment on the system thermals, structural strength and power transfer

While lots of information can be obtained from a detailed digital-twin model, there is a trade-off between the time taken to develop and tune the model and the level of detail included. Depending on the application, various levels of complexity can be included in a digital-twin model. This dissertation focuses on the FEM simulation model and the circuit simulation models. Details on the thermal and structural modeling of DWPT systems can be found in [92, 93].

Dynamic inductive power transfer systems are typically modeled as discrete stationary inductive power transfer systems due to the ease of modeling. This chapter presents a

detailed workflow, modeling dynamic inductive power transfer systems, starting from FEM models using ANSYS Maxwell and obtaining accurate circuit simulation models that can be implemented in both SPICE and PLECS simulation software. This chapter details the modeling methods used to simulate DWPT pads and the corresponding power electronics required.

3.2 Generalized DWPT System

As explained in Chapter 2, inductive wireless power transfer systems are typically modeled as a loosely coupled transformer as shown in Fig. 3.1. A single transmitter and single receiver case is shown here for simplicity.

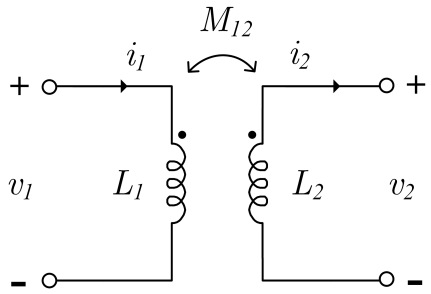

Fig. 3.1: Circuit diagram showing two loosely coupled coils.

The two-port network voltage and current relationships can be represented in matrix form as follows

$$\begin{bmatrix} v_1 \\ v_2 \end{bmatrix} = \begin{bmatrix} L_1 & M_{12} \\ M_{12} & L_2 \end{bmatrix} \begin{bmatrix} \frac{di_1}{dt} \\ \frac{di_2}{dt} \end{bmatrix} \tag{3.1}$$

where the mutual inductance M_{12} is related to the coupling coefficient k as shown in (3.2)

$$M_{12} = k\sqrt{L_1 L_2} \tag{3.2}$$

For a generalized system with multiple transmitter and receiver pads, the coupled

inductor is shown in Fig. 3.1 and (3.1) are modified to obtain Fig. 3.2 and the matrix shown in (3.3).

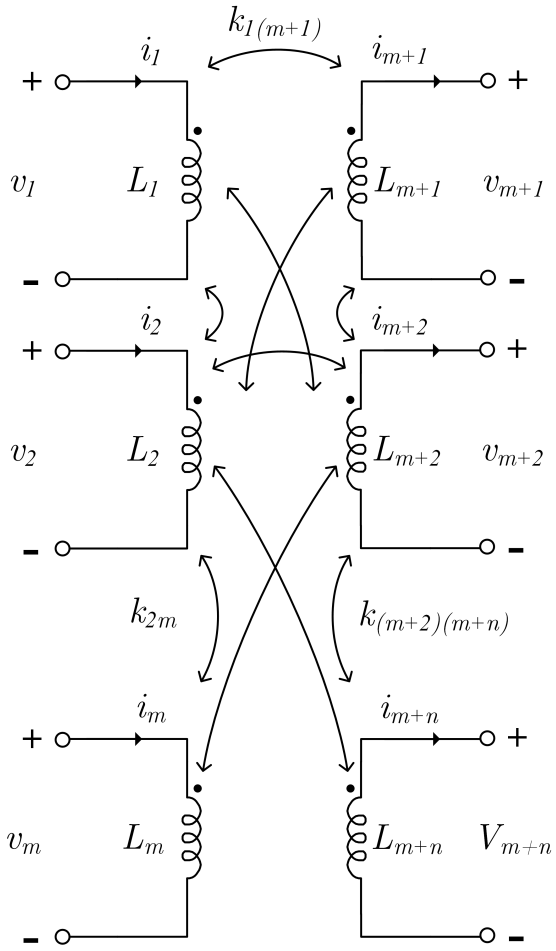

Fig. 3.2: Circuit diagram showing a generalized multi-coil WPT system.

$$\begin{bmatrix} v_1 \\ v_2 \\ \vdots \\ v_{(m+n)} \end{bmatrix} = \begin{bmatrix} L_1 & M_{12} & \dots & M_{1(m+n)} \\ M_{12} & L_2 & & \\ \vdots & & \ddots & \\ M_{1(m+n)} & & & L_{(m+n)} \end{bmatrix} \begin{bmatrix} \frac{di_1}{dt} \\ \frac{di_2}{dt} \\ \vdots \\ \frac{di_{(m+n)}}{dt} \end{bmatrix} \tag{3.3}$$

In case of stationary wireless power transfer systems with fixed air-gap and misalignment, the coil self-inductances L_1, L_2, $\ldots L_{m+n}$ and mutual inductances M_{12}, M_{13}, $\ldots M_{1(m+n)}$ are constant values and can be used to compute the required voltages and currents in the system. In case of dynamic wireless power transfer systems, the self- and mutual inductances in the inductance matrix are time-dependent variables and the modified inductance matrix can be represented as follows

$$\begin{bmatrix} L_1(t) & M_{12}(t) & \ldots & M_{1(m+n)}(t) \\ M_{12}(t) & L_2(t) & & \\ \vdots & & \ddots & \\ M_{1(m+n)}(t) & & & L_{(m+n)}(t) \end{bmatrix} \tag{3.4}$$

where t is the time. The time varying functions $L_1(t)$, $L_2(t)$, $\ldots L_{(m+n)}(t)$ and $M_{12}(t)$, $M_{13}(t)$, $\ldots M_{1(m+n)}(t)$ are dependent on vehicle speed and longitudinal misalignment coupling coefficient profiles in the direction of vehicle motion. The matrix shown in (3.4) can be calculated using (3.5) and the desired vehicle speed.

$$\begin{bmatrix} L_1(x) & M_{12}(x) & \ldots & M_{1(m+n)}(x) \\ M_{12}(x) & L_2(x) & & \\ \vdots & & \ddots & \\ M_{1(m+n)}(x) & & & L_{(m+n)}(x) \end{bmatrix} \tag{3.5}$$

where x is the time. $L_1(x)$, $L_2(x)$, $\ldots L_{m+n}(x)$ and $M_{12}(x)$, $M_{13}(x)$, $\ldots M_{1(m+n)}(x)$ are dynamic self- and mutual inductance profiles of the DWPT system.

Variable x in this context refers to the longitudinal misalignment of the system. An example of the coupling coefficient between one primary pad and one secondary pad in the system as a function of longitudinal misalignment $k_{ps}(x)$ is shown in Fig. 3.3 and the corresponding time varying coupling coefficient $k_{ps}(t)$ is plotted in Fig. 3.4.

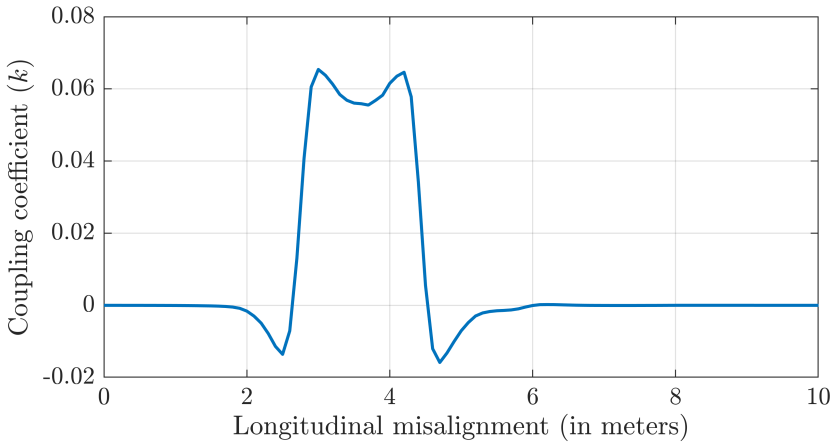

Fig. 3.3: Example showing the coupling coefficient between one primary pad and one secondary pad in the system as a function of longitudinal misalignment.

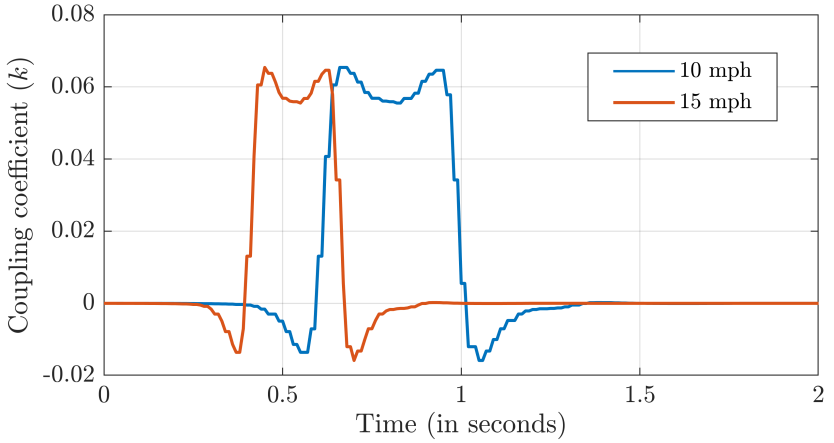

Fig. 3.4: Example showing the coupling coefficient between one primary pad and one secondary pad in the system as a function of time at different speeds.

3.3 Simulation Workflow

The process of simulating DWPT systems is outlined in Fig. 3.5. The preliminary inputs at the beginning of the modeling process are as follows:

- Coil shape (topology) and geometric dimensions
- DC/AC and AC/DC power electronics
- Primary and secondary compensation topologies
- System power level

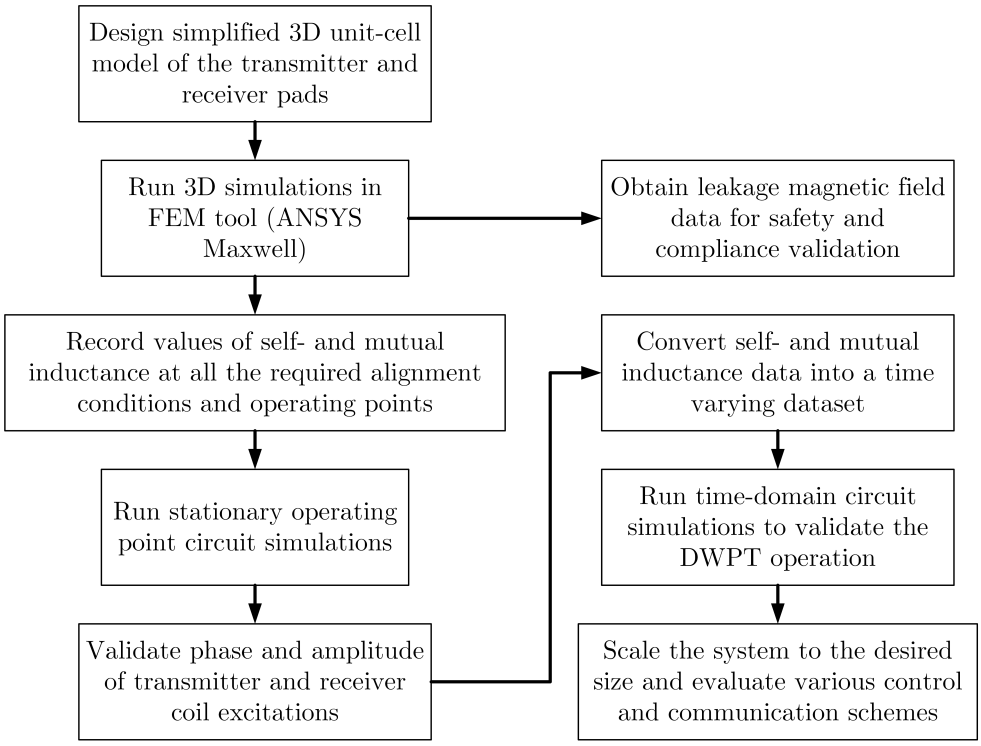

Fig. 3.5: Flowchart showing the DWPT FEM and circuit modeling process.

The digital-twin modeling process begins with the development of a 3D model for simulation in an FEM tool such as ANSYS Maxwell. The preliminary simulation yields system parameters such as coupling coefficient, and self- and mutual inductances between all the

coils modeled. This data can then be used to design the primary and secondary compensation networks based on the system power level requirements. Once the compensation values are modeled based on realistic capacitor and inductor values, the WPT system can be simulated in a circuit simulator such as LTSpice or PLECS. The amplitude and phase of currents in various components of the system can be analytically calculated or obtained from the circuit simulation. The amplitude and phase data is then applied to coils in the ANSYS model to obtain transient loss distribution and leakage magnetic field data. For DWPT systems with more than three primary pads, a unit-cell model can be identified as explained in Section 3.4.1 and the system behavior can be extrapolated from a simplified model.

3.4 Magnetic Model

Simulated inductive coupler models for static and dynamic wireless power transfer systems have been extensively used in prior works [23, 25, 28, 54, 69]. The objective of an FEM simulation is to obtain the inductance matrix for all the coils in the system. For a system with m primary coils and n secondary coils, an $(m+n) \times (m+n)$ matrix can be obtained to model the circuit behavior during the dynamic system operation. In practical DWPT systems, a stretch of roadway is embedded with inductive charging coils and one or more vehicles travel over the electrified roadway section and receive charge. The number and total length of all primary pads is expected to be far greater than the length of individual secondary pad assemblies. To reduce the complexity of the magnetic simulation, the parameters obtained from a small section of roadway can be extrapolated to obtain the entire system behavior. This model is described as a unit-cell model and can also be used to simulate radiated magnetic fields and ensure safety and EMC regulations are met.

Using optimetric sweeps along the direction of vehicle motion, various inductance profiles are obtained which are a function of X-misalignment (in the direction of vehicle motion or longitudinal direction). Similarly, inductance matrix profiles can also be obtained for different values of Y-misalignment (to emulate lateral misalignment of the vehicle). The obtained magnetic characteristics of the system are then used to develop a circuit model

to analyze the system behavior and aid in compensation network design and evaluate controller behavior with system dynamics. With a circuit model simulation of the inductive power transfer system, realistic circuit behavior can be analyzed, and auxiliary sensing and detection circuits can be evaluated before the full system is built.

3.4.1 Unit-cell Model

Practical dynamic wireless charging systems are expected to span several meters at a stretch to enable charging zones along different interstate highways and city roads. Developing a electro-magnetic FEM model for the entire stretch of road is challenging due to the computational power needed to model and run a full system FEM simulation. The solution to this challenge is to identify a unit-cell in the system and extrapolate the electro-magnetic characteristics to model the entire system. The unit-cell model is the smallest number of transmitter and receiver pads that can be modeled to ensure an accurate repeating model of the system. The unit-cell model is unique to each system design and modeling objectives of the system. A method to identify and model the unit-cell of a system is presented in this subsection.

The following criteria are established for a model to satisfy the unit-cell requirements:

- The electro-magnetic behavior of the entire system should be replicable by extrapolating the unit-cell model.
- The coupling coefficient (k) or mutual inductance (M) variations greater than 1% of the corresponding peak values should be included in the model.
- The unit-cell model should be applicable to different values of lateral misalignment and air-gaps.

An example system is considered with four transmitter pads and one receiver pad. The three different models simulated are shown in Fig. 3.6. Coupling factors between each primary pad and receiver pad are presented in Fig. 3.7 and the coupling factors between adjacent primary pads are presented in Fig. 3.8. The parameters used in the above example

are as given in Table 3.1. A second example is also considered with the primary pad dimension almost equal to the secondary pad dimension. The geometric parameters for this system are given in Table. 3.2. The three different models simulated are shown in Fig. 3.9. Coupling factors between each primary pad and receiver pad are presented in Fig. 3.10 and the coupling factors between adjacent primary pads are presented in Fig. 3.11.

Table 3.1: Example 1 geometric parameters.

Parameter	Value
l_{Tx}	1400 mm
l_{Rx}	600 mm
l_{gap}	200 mm

Table 3.2: Example 2 geometric parameters.

Parameter	Value
l_{Tx}	700 mm
l_{Rx}	600 mm
l_{gap}	200 mm

It can be seen from Fig. 3.8b and Fig.3.11b that the coupling between the different primary pads is accurately modeled using the three-coil model. When a two coil model is used for extrapolation as shown in Fig. 3.8c and Fig. 3.11c, the coupling data between adjacent pads is lost and hence these effects can't be modeled in the circuit simulations. Therefore a three-coil model with two primary pads and one secondary pad is sufficient to model and extrapolate the behavior of the full coil model in the two examples considered. This holds true for all systems where the primary pad is at least as long as the receiver pad assembly in the longitudinal direction and satisfies (3.6). In a practical DWPT system, it is unlikely that the individual primary pads are smaller than the receiver pads. Hence the three-coil unit-cell model can be applied to model all practical DWPT systems.

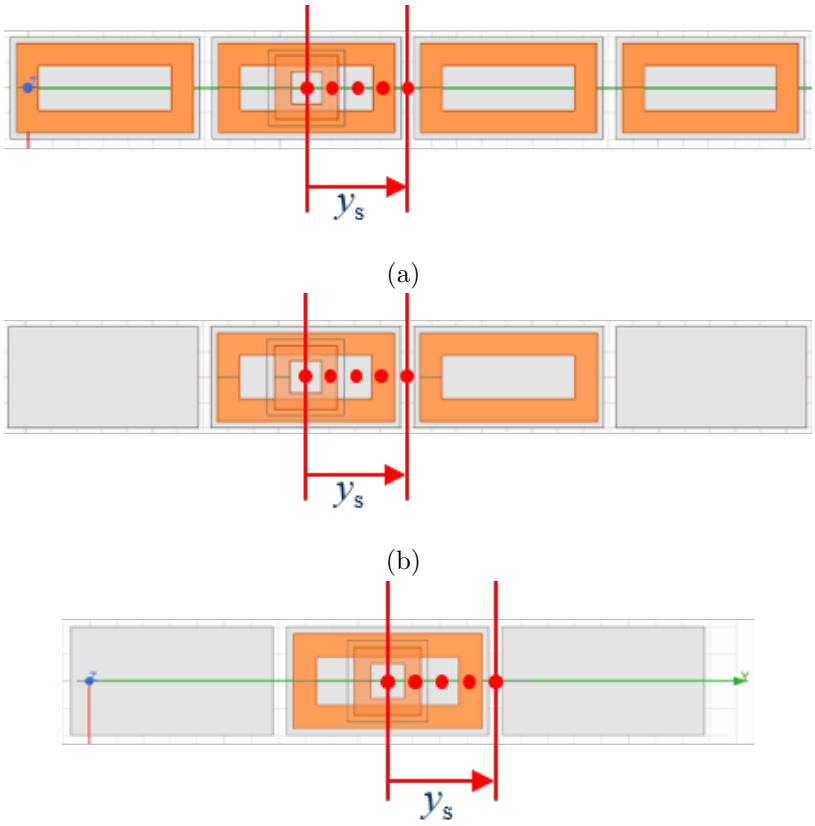

(a)

(b)

(c)

Fig. 3.6: ANSYS models showing the a) full coil model b) three-coil model and c) two-coil model for a DWPT system with $l_{tx} = 1400\,\text{mm}$.

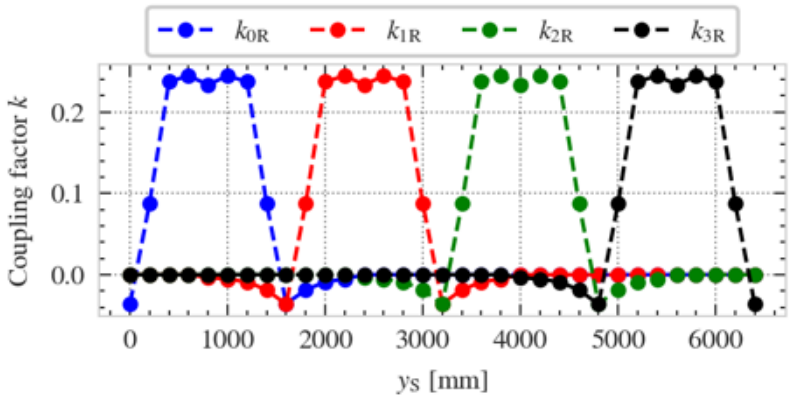

(a)

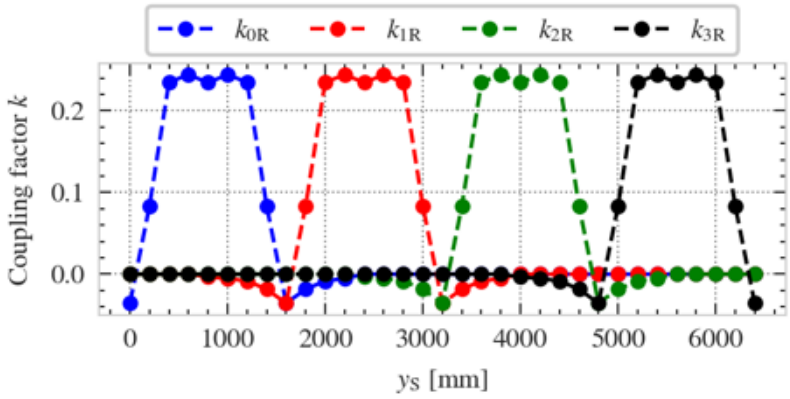

(b)

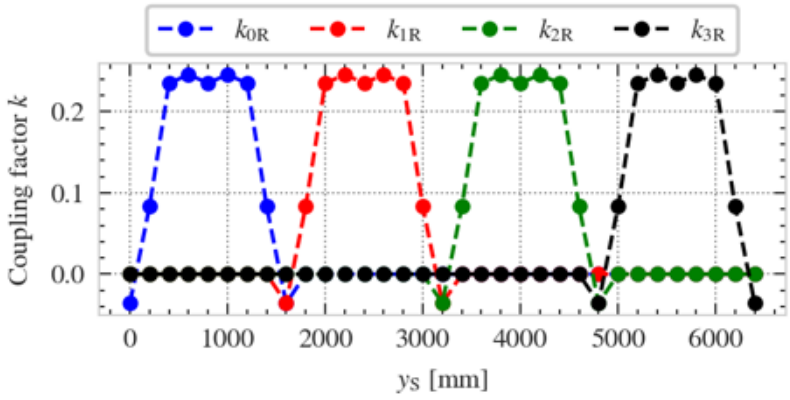

(c)

Fig. 3.7: Coupling factors between each primary and secondary pad using a) full coil model b) three-coil model and c) two-coil model for a DWPT system with $l_{tx} = 1400\,\text{mm}$.

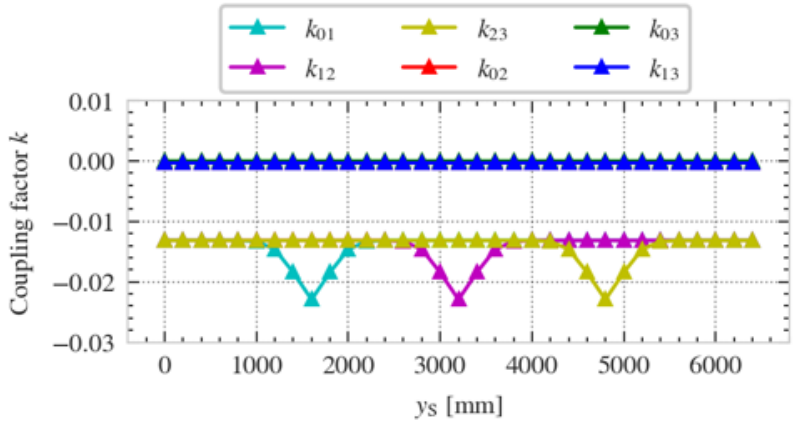

(a)

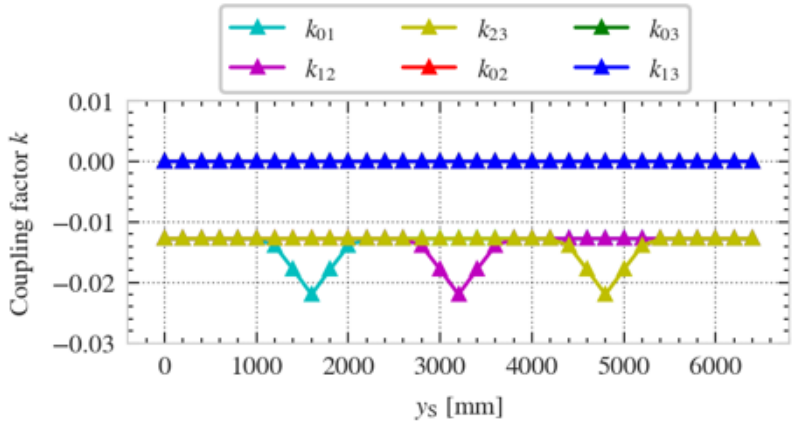

(b)

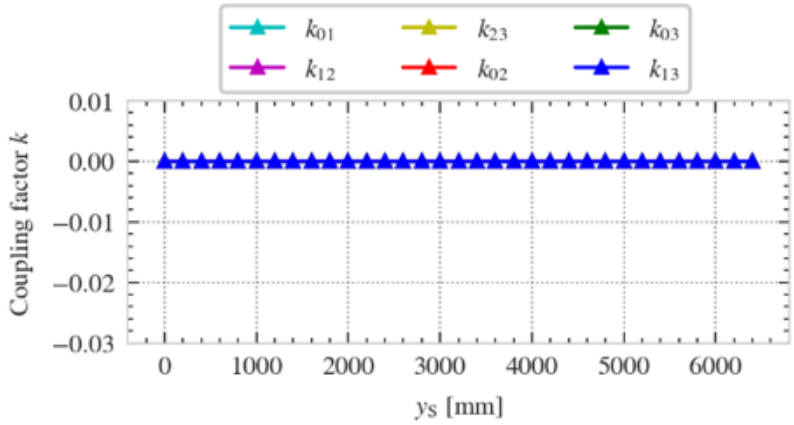

(c)

Fig. 3.8: Coupling factors between adjacent primary pads using a) full coil model b) three-coil model and c) two-coil model for a DWPT system with $l_{tx} = 1400\,\text{mm}$.

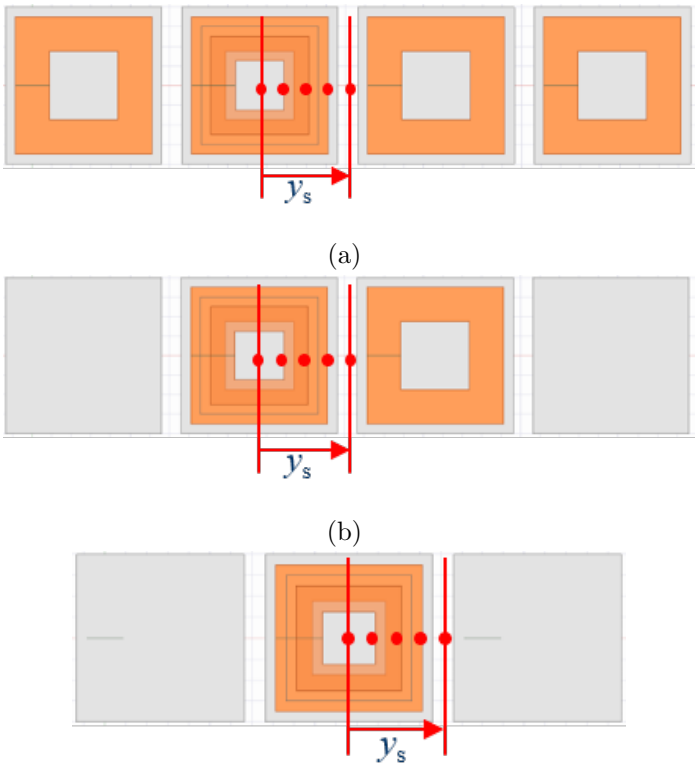

Fig. 3.9: ANSYS models showing the a) full coil model b) three-coil model and c) two-coil model for a DWPT system with $l_{tx} = 700\,\text{mm}$.

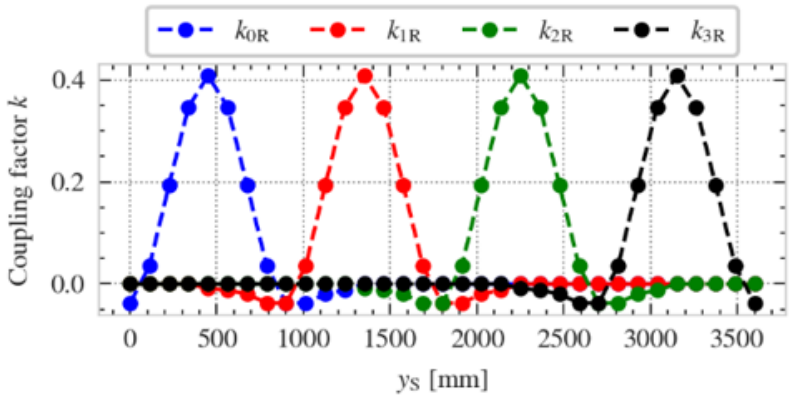

(a)

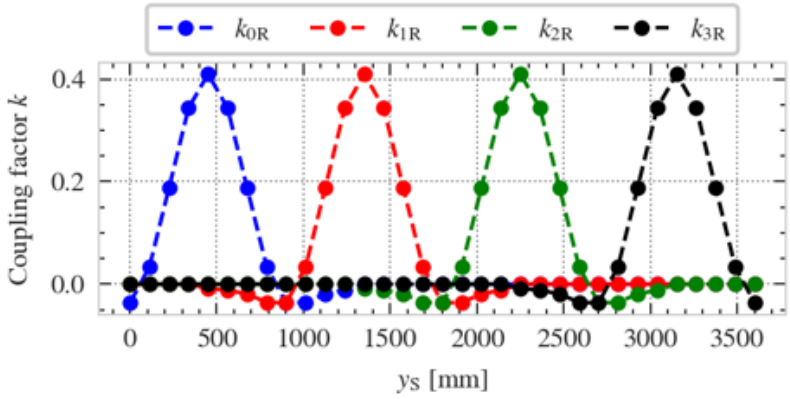

(b)

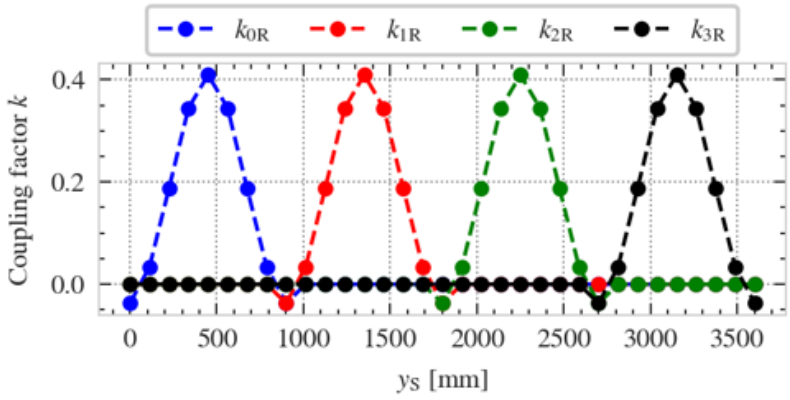

(c)

Fig. 3.10: Coupling factors between each primary and secondary pad using a) full coil model b) three-coil model and c) two-coil model for a DWPT system with $l_{tx} = 700\,\text{mm}$.

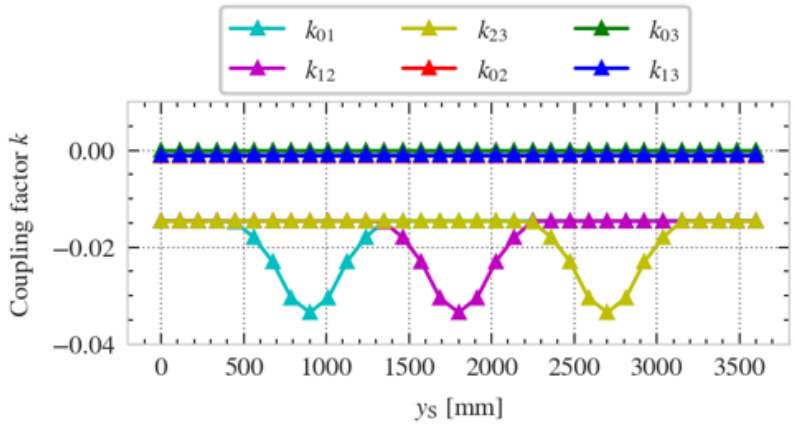

(a)

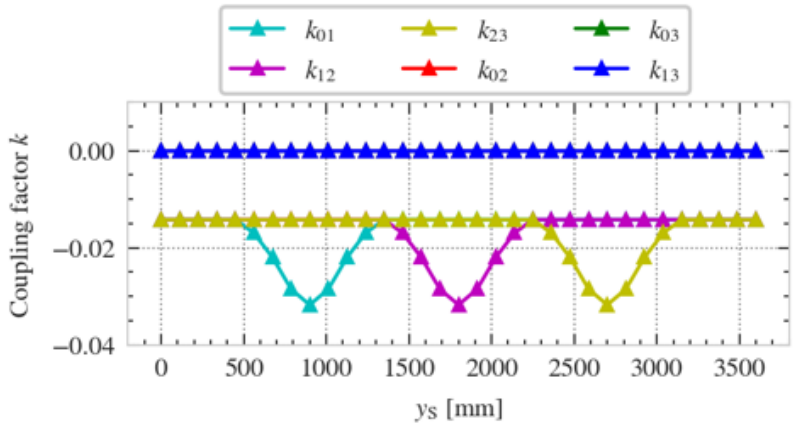

(b)

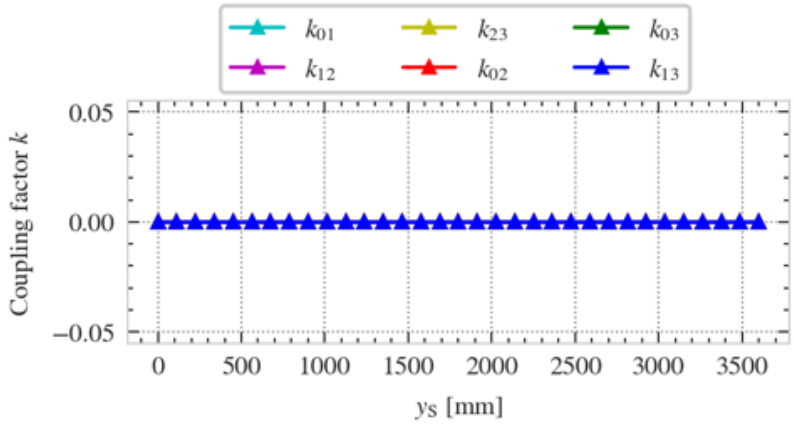

(c)

Fig. 3.11: Coupling factors between adjacent primary pads using a) full coil model b) three-coil model and c) two-coil model for a DWPT system with $l_{tx} = 700\,\text{mm}$.

$$\frac{2 \times l_{\mathrm{Tx}} + l_{\mathrm{gap}}}{l_{\mathrm{Rx}}} > 2 \tag{3.6}$$

where l_{Tx} is the length of each individual primary pad, l_{Rx} is the length of each individual secondary pad assembly and l_{gap} is the longitudinal distance between two adjacent primary pads.

3.5 Circuit Model

3.5.1 LTSpice

To create a circuit model in LTSpice, the inductance matrix (3.5) obtained from ANSYS Maxwell is converted to a time-varying inductance matrix (3.4) based on the desired vehicle speed. In the current work, a Matlab script is used to generate the desired time-varying inductance matrix from an X-misalignment dependent inductance matrix obtained from ANSYS. This conversion can be customized to adjust resolution of the data, vehicle speed, and misalignment. The time-varying inductance matrix is transferred to LTSpice using the Piecewise Linear (PWL) function option as shown in Fig. 3.12. Here, an example system containing four transmitter coils and one receiver coil is considered. A few of the dependent voltage sources used to model the differential equations presented in (3.3). For example, the files L1data.txt and k12data.txt contain comma separated values of self-inductance of L_1 and coupling coefficient k_{12}. The time-varying self- and mutual inductances are then used to calculate the externally induced voltages on each coil and model the behavior of the DWPT system as shown in Fig. 3.13. A sinusoidal 85 kHz current source is used in this example to simplify the model. Additional details regarding the compensation network and power electronics can also be added to the model in place of the sinusoidal current source.

3.5.2 PLECS

The circuit model in PLECS is modeled using a variable inductor model. The dynamic profile of pad self- and mutual inductances are provided in the form of a control signal

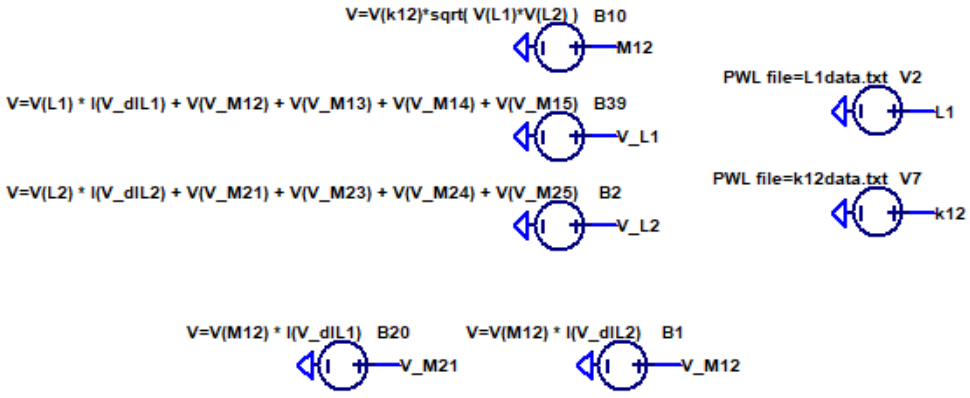

Fig. 3.12: Examples of dependent voltage sources modeled in LTSpice to describe the behavior of DWPT pads.

vector to the variable inductor. PLECS requires that the inductances be arranged by the elements of the inductance matrix (row by row) followed by their time derivatives as shown in (3.7). The control vector matrix therefore has a width of $2.(m+n)^2$, where $(m+n)$ is the total number of coils being modeled. The terminals of all coils are connected to wire multiplexers at each terminal of the variable inductor as shown in the example in Fig. 3.15. This models the variable coupling behaviour of all coils in the DWPT system and their time varying behavior. The rest of the system components including the compensation network, inverters, rectifiers, controls and communication system can be modeled in PLECS or Simulink as required. An example system with three transmitters and three receiver pads is shown. The top-level PLECS schematic is shown in Fig. 3.14. The three transmitter pads are powered from three independent power supply units (PSUs) and the three receiver pads are connected in series and connected to one rectifier unit. The Dual-LCCL compensation networks are also modeled in the simulation. The elements inside the PSU1 and SecReg1 subsystems are shown in Fig. 3.16 and Fig. 3.17 respectively. LP1_1 and LP1_2 are the two terminals of the first transmitter pad and LS1_1 and LS1_2 are the two terminals of the first receiver pad. The example in consideration is based on the system designed in Chapter 5. Hence the simulation validation results are also presented in Chapter 5.

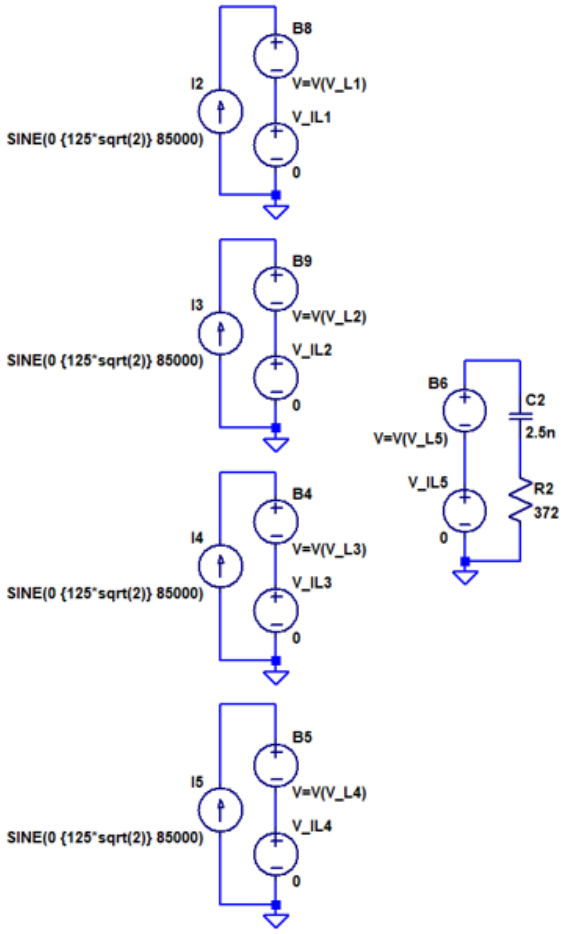

Fig. 3.13: Four transmitter pads and one receiver pad modeled as part of a DWPT system in LTSpice.

$$\text{Lmat} = \begin{bmatrix} L_1 & M_{12} & \dots & M_{(m+n-1)(m+n)} & L_{(m+n)} \dots \\ \frac{d}{dt}L_1 & \frac{d}{dt}M_{12} & \dots & \frac{d}{dt}M_{(m+n-1)(m+n)} & \frac{d}{dt}L_{(m+n)} \end{bmatrix} \tag{3.7}$$

3.5.3 Summary

A comprehensive simulation work flow including FEM simulations and time domain circuit simulations is developed in this chapter. The digital twin models presented in this chapter allow designers to evaluate various pad shapes and power electronics topologies without the need for a complex hardware build-out. This simplifies the process of designing DWPT systems.

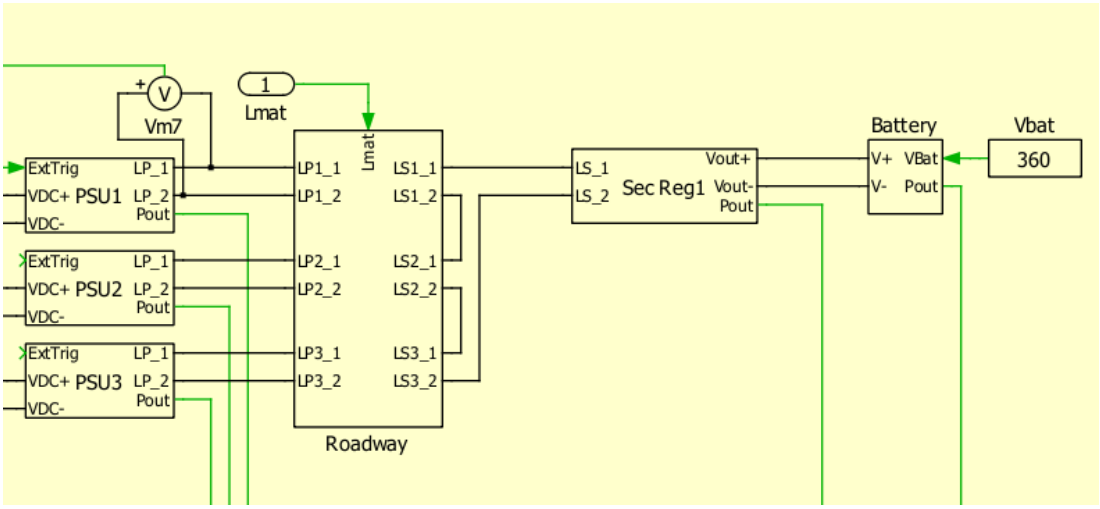

Fig. 3.14: Top level PLECS schematic showing the three transmitter pad and three receiver pads modeled using the Roadway block.

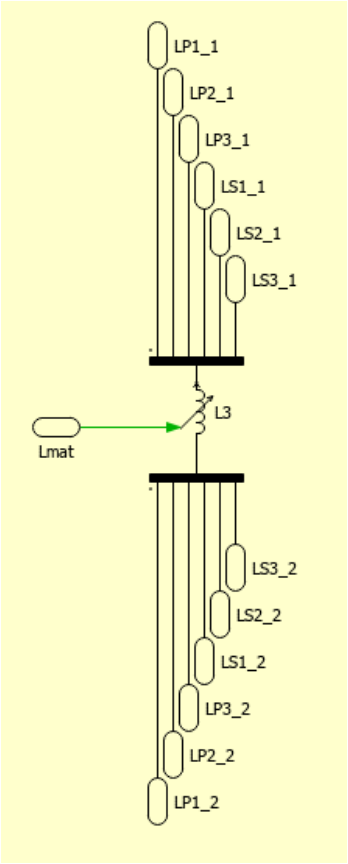

Fig. 3.15: PLECS schematic showing the elements inside the Roadway block.

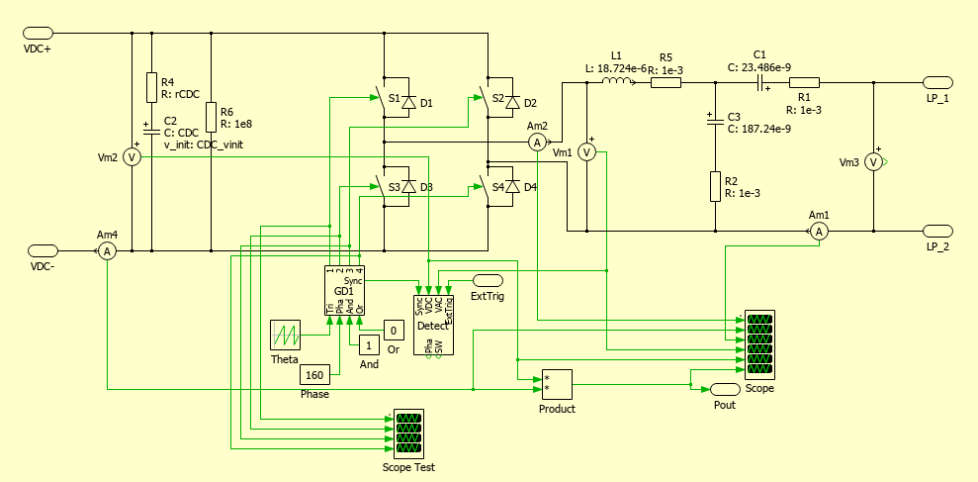

Fig. 3.16: PLECS schematics showing the primary side elements modeled inside the PSU block.

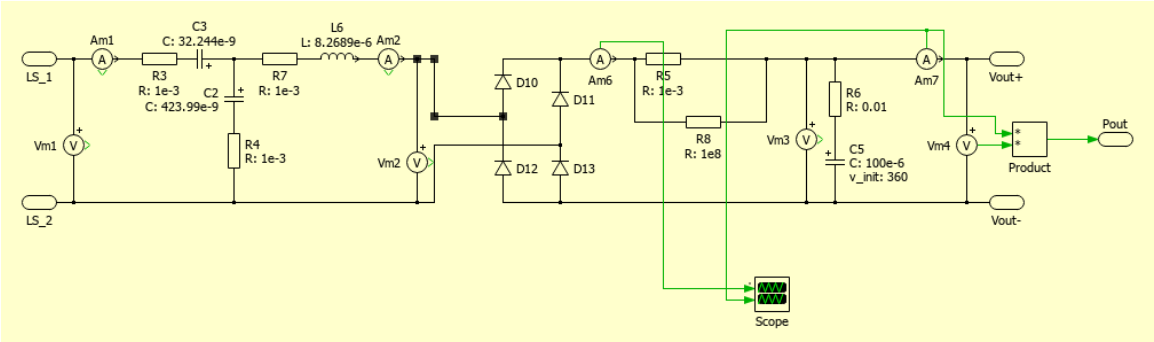

Fig. 3.17: PLECS schematics showing the secondary side elements modeled inside the SecReg1 block.

CHAPTER 4

ROADWAY-EMBEDDED TRANSMITTER COILS

Practical implementation of dynamic inductive power transfer requires integrating coil design techniques with existing construction methods. This work explores the various design challenges associated with embedding inductive power transfer (IPT) coils in concrete pavements. The coil design process outlined in this chapter takes into account the structural aspects of concrete pavements and ease of construction. This chapter also explores the effects of ferrite spacing on losses generated in the pad. A phase change material is used for passive thermal management of ferrite bars inside the concrete. Multiple concrete-embedded pad prototypes are built and tested for their electrical and structural properties.

Dynamic wireless charging systems allow EVs to recharge while in motion and can theoretically help them achieve infinite range depending on the percentage of roadways that are electrified [81, 94, 95]. Dynamic wireless charging systems require lower power levels than extreme fast charging (XFC) systems and thereby reduce peak loading on the grid. The lower rate of charge offered by dynamic wireless charging systems can prolong EV battery life [96].

Integrating dynamic wireless power transfer (DWPT) systems with roadway construction is seen as the next step towards practical adoption of DWPT technologies. This chapter presents the design and testing of a 50 kW concrete-embedded DWPT system.

4.1 Design Considerations

Based on engineering experiences with wireless charging systems and challenges faced in prior works, various design decisions are made to improve the performance of the current system.

4.1.1 Wire Insulation Jacket

Prior implementations of pavement-embedded wireless charging coils in the concrete or asphalt showed an increase in the effective series resistance (ESR) of the pad and a subsequent drop in the pad quality factor (Q) [1, 10]. The quality factor of the pad Q is defined as shown in (4.1), where L_{pad} is the self-inductance of the pad. Results showing a change in impedance before and after concrete-embedding can be seen in Fig. 4.1 and Table. 4.1. The large variation in the pad impedance renders the WPT system unusable due to the increase in conductive losses in the system.

$$Q = \frac{\omega L_{pad}}{ESR} \tag{4.1}$$

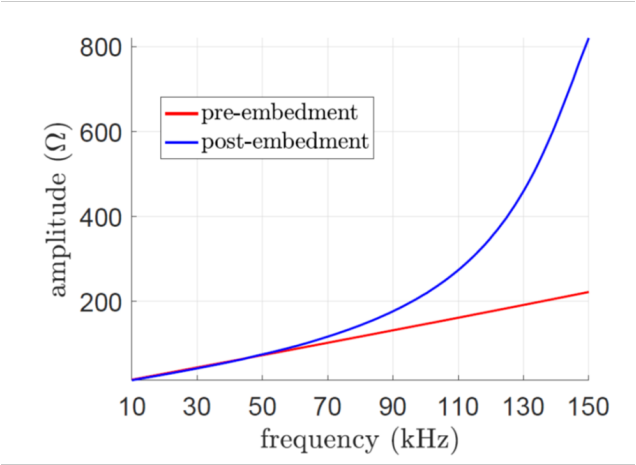

Fig. 4.1: Comparison of coil impedance before and after embedding the coil in concrete [10].

Table 4.1: Long-term inductance and resistance values [1].

Measurement	Initial	28 days	60 days
Inductance (μH)	170.5	170.5	170.5
Resistance (Ω)	0.25	8.00	4.50

Upon further inspection, the reason for this change in coil impedance is identified as

the insufficient insulation thickeness available on both the coils. Fig. 4.2 and Fig. 4.3 show the use of single nylon insulation on the respective Litz wires.

Fig. 4.2: Circular pad with single-nylon insulation being directly embedded in concrete [1].

Fig. 4.3: Rectangular pad with single-nylon insulation directly embedded in concrete [10].

The Litz wire chosen for this work uses a 2 mm thermoplastic elastomer (TPE) insulation for waterproofing and reducing the eddy current losses due to soluble salts present in concrete. An image of the wire cross section is shown in Fig. 4.4.

A small-scale circular pad (CP) prototype is constructed using the chosen Litz wire as shown in Fig. 4.5. The prototype pad includes the coil, ferrite, and steel rebar for

Fig. 4.4: Litz wire with 2 mm TPE insulation used to construct the coils.

reinforcement. The pad inductance and equivalent series resistance (ESR) are measured before, during and after the concrete pour. The parameters are also measured over the consequent 68 hours of concrete curing. The results are combined into a Q factor plot and are shown in Fig. 4.6. The x-axis on this graph is plotted in a logarithmic scale to allow the reader to observe the initial change in Q and its gradual recovery back to the initial value.

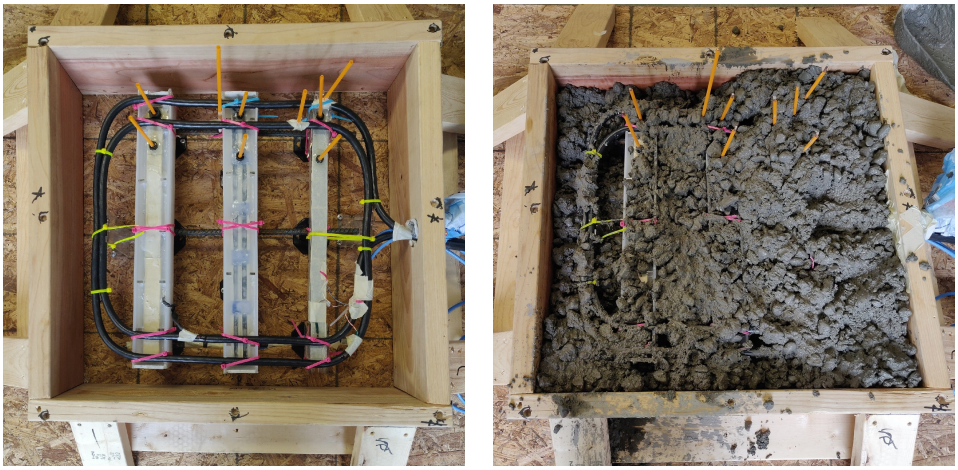

(a) (b)

Fig. 4.5: Scaled-down prototype of the coil designed to evaluate the performance of the TPE insulating jacket a) before concrete pour b) during concrete pour.

4.1.2 Coil Shape and Design

Inductive charging coils require a high quality factor for efficient power transfer [68].

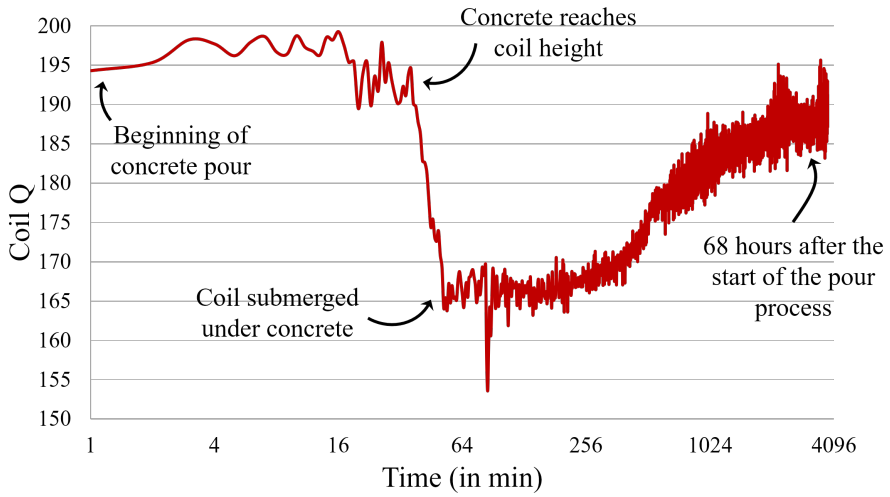

Fig. 4.6: Variation in the prototype coil Q over a 68 hour time period from the start of concrete pouring.

Therefore, coils designed for static or dynamic wireless charging include multiple turns with a high ferrite fill-factor to increase inductance or multiple parallel windings to decrease series resistance [69, 72]. When it comes to designing concrete-embedded IPT coils, this approach results in coil designs with high area fill-factor and limited space for the concrete to flow through. WPT pads behave as foreign objects in pavements and can cause artificial discontinuities in concrete, decrease the load bearing capacity [97], and create sites for pavement failure. To minimize the effect of these discontinuities, coil designs with lower fill-factor are required. Fill-factor in the context of the present work is considered to be the ratio of area occupied by the material to the area occupied by the entire pad. Taking the above factors into consideration, a pad structure is designed with a copper area fill-factor of 12% and a ferrite area fill-factor of 30%. This leaves more than 60% of the pad area to be filled in by concrete (some of the copper and ferrite areas overlap which results in the percentages not adding up).

An elongated DD coil is arbitrarily chosen for the purpose of this work, but the above mentioned design principles can be applied to other coil topologies as well.

4.1.3 Ferrite Shape

The structural engineering constraints mentioned in Section 4.1.2 restrict the use of an aluminum backplate and a continuous ferrite structure as both these features can restrict the flow of concrete during pavement construction. Additionally, concrete used for roadway construction includes coarse aggregate particles ranging from 4.5 mm to 37.5 mm in diameter. The use of larger aggregates keeps the construction costs low and meets pavement design requirements. The current work uses a concrete mix which contains approximately 40% of #57 rock (25 mm in diameter). These large aggregate particles need to flow through the WPT coil and ferrite assembly to obtain a homogeneous composition of the concrete structure. To allow the flow of these coarse aggregate particles in concrete, the lowest spacing between adjacent windings or ferrite bars is chosen to be 50 mm.

4.1.4 Frequency Selection

The choice of system frequency in a WPT system depends on a variety of factors. Prior works can be categorized primarily into two frequency ranges - 20 kHz and 85 kHz.

As discussed in Section 2.2, the output power of an inductive WPT system is given by

$$P_{out} = QS_u \tag{4.2}$$

where Q is the loaded quality factor of the system and S_u is the uncompensated power [68]. The S_u can be calculated as follows

$$S_u = \omega I^2 k^2 L_{pad} \tag{4.3}$$

where I is the current flowing through a primary coil with self-inductance L_{pad} and ω is the angular frequency of the excitation current given by (4.4). The coupling coefficient between the primary and secondary coils is represented by k.

$$\omega = 2\pi f \tag{4.4}$$

where f is the fundamental frequency of the primary coil excitation. The voltage build up across the pad terminals is given by

$$V_{pad} = I_{pad} Z_{pad} \tag{4.5}$$

$$V_{pad} = j\omega L_{pad} I_{pad} \tag{4.6}$$

From (4.3) and (4.2) it is evident that a higher frequency of operation results in a higher output power with the same pad design and coupling coefficient k. It is important to note that as the frequencies of operation are pushed higher, the ferrite losses tend to increase significantly, thereby decreasing system efficiency. Therefore it is uncommon to find high power WPT systems operating over 150 kHz. Further, it can be observed from (4.6) that a higher frequency of operation results in larger voltages across the coil terminals. This requires additional high voltage safety features and an increase in system insulation requirements. The factors affecting the frequency selection can be summarized as shown in Table. 4.2. Taking these factors and the existing SAE J2954 standard into consideration, an operating frequency of 85 kHz is chosen.

4.1.5 Pavement Reinforcement

The designed DWPT pad needs to be supported at a fixed height until the concrete cures. The pad makes use of structural rebar in the concrete to support its weight without needing additional structures inside the pavement. Since structural rebar is typically used in concrete to improve the tensile strength and longevity, it is advantageous to use the same rebar as a support structure for the pad. Steel is typically used to reinforce concrete slabs, but in the presence of high frequency magnetic fields (85 kHz) generated by the IPT coils, it causes localized heating due to eddy currents and core losses. Initial hardware tests indicate that a steel rebar structure used with the IPT pad designed in Section 4.2 generates a loss of 790 W when a current source output from the LCCL compensation network generates 187 ampere-turns in the primary pad structure. This localized heating causes a temperature

Table 4.2: Summary of how system attributes are affected by frequency.

System attribute	20 kHz range	85 kHz range
Pad size	Large	Small
Voltage across the coil terminals	Low	High
Switching devices	IGBT, Si, SiC	Si, SiC
ICNIRP limit compliance	Higher limits for harmonic frequencies	Lower limits for harmonic frequencies
Loss mechanisms	Comparatively lower losses	Higher skin effect loss, core loss and switching loss (if hard switching)
Existing EV standards	No specific standard governing this frequency range	Existing EV wireless chargers make use of the SAE J2954 standard
Miscellaneous	Possible issues with audible noise	Second harmonic and higher frequencies could interfere with amateur radio frequencies

gradient in the concrete structure which can result in cracking and structural failure [98], in addition to a decrease in system efficiency. This loss can be mitigated by the use of a non-metallic fiberglass rebar structure replacing the steel rebar [99]. Owens Corning Aslan 100 #4 fiberglass rebar is used in this system. Thermal imagery of the two different pad structures in Fig. 4.7 shows the localized heating caused in the pad with steel rebar compared to an identical pad with fiberglass rebar. Fig. 4.7a shows the steel rebar grid structure reaching temperatures above 91 °C and the same rebar grid when replaced with fiberglass rebar is practically invisible on the thermal image in Fig. 4.7b. Additional benefits of using fiberglass for reinforcement are its corrosion resistance and lighter weight compared to steel rebar. It should be noted that the thermal distribution on the ferrite bars can be simulated accurately using FEM tools such as ANSYS Maxwell and this closely corresponds to the magnetic flux distribution in the ferrite bars. The thermal images shown in Fig. 4.7 show an uneven distribution of heat in the ferrite bars since each ferrite bar was set to have different spacing configurations as discussed in Section 4.1.6. However, in the final

pad design used for testing, all the ferrite bars are identical.

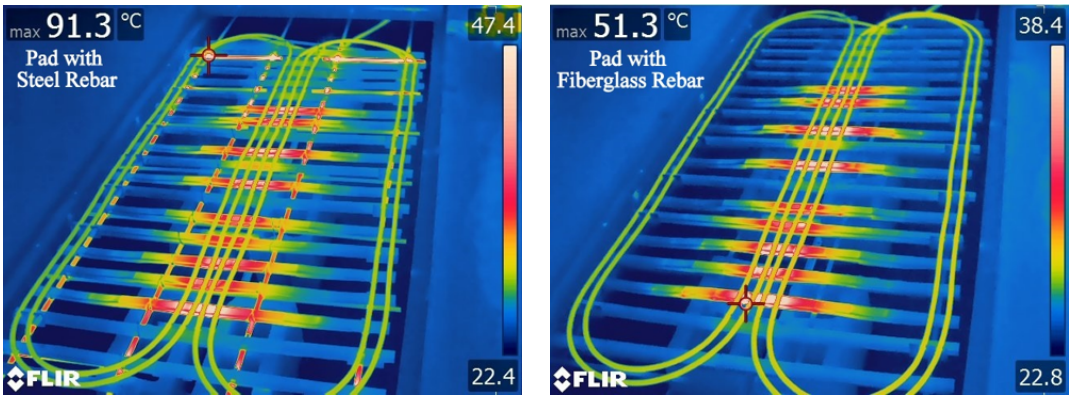

(a) (b)

Fig. 4.7: Thermal image of the prototype pad when energized with nominal track current a) prototype with steel rebar b) prototype with fiberglass rebar.

4.1.6 Thermal Management

Coil and Ferrite

Wireless charging pads generate heat under normal operation in the form of copper and ferrite losses. Excessive heating in electronic systems can cause performance issues and even hardware failure. This problem is compounded when the system is enclosed in concrete, which has a low thermal conductivity. Further, localized temperature gradients in concrete can cause structural failure due to stresses [98].

The required ferrite rods for the primary pad are constructed by stacking CF139 ferrite bars (93 x 27.5 x 16 mm) end to end. This configuration results in the highest value of primary inductance, and consequently a high value of power transfer between the primary and secondary coils when the thermal aspects of the system are neglected. The heat generation profile of this ferrite configuration as observed using a FLIR T640 thermal camera corresponds to an FEM profile of loss generation simulated in ANSYS Maxwell.

Considering the thermal effects of ferrite heating, an internally distributed air-gap

within the ferrite rods helps reduce the magnetic flux going through the rod. However, the introduction of air gaps within the ferrite rods leads to a decrease in self-inductance of the primary pad and hence a decrease in power transfer capability for the same track current. There exists an optimal configuration for ferrite spacing that can achieve relatively high primary pad self-inductance while eliminating hotspots in the ferrite. Different ferrite spacing configurations are evaluated to determine the optimal design.

Optimal Ferrite Spacing

The primary DD pad consists of two turns wound using the 2 AWG Litz wire and ferrite bars along the direction of the flux path. To facilitate the use of larger aggregate and improve the structural properties when the pad is embedded in concrete, a ferrite fill factor of 30% is chosen. The presence of air gaps in the ferrite bars, along the flux path increases the effective reluctance of the path, decreases the amount of magnetic field intensity in the ferrite and thus decreases core loss generated in the ferrites. While this is a desirable characteristic, these air gaps also decrease the self-inductance of the primary pad and its coupling with a secondary pad. Consequently, the track current needs to be increased to maintain the same amount of power transfer. With an increase in track current, the Ohmic losses in the pad winding increase. To study the trade-offs, three different ferrite spacing configurations as shown in Fig. 4.8 are simulated and constructed for hardware validation. The simulation results are shown in Fig. 4.9 and the experimental results are shown in Fig. 4.10. The simulation results and experimental tests show a close correlation in the ferrite loss distribution.

To quantify these effects and identify optimal length of the air gap and its position, the following analysis is performed. To maintain pad symmetry, the air gaps are assumed to be symmetric about the length of the pad as shown in Fig. 4.11. The distance between an air gap and the center of the pad cross section is taken to be x_{AG}. The length of the air gap is taken to be l_{AG} and the width of the ferrite is taken to be W_{Fe}, which is also the width of the pad. Multiple designs are simulated by varying x_{AG} and l_{AG} and measuring the core loss and calculating the Ohmic losses. The results from the optimal ferrite spacing

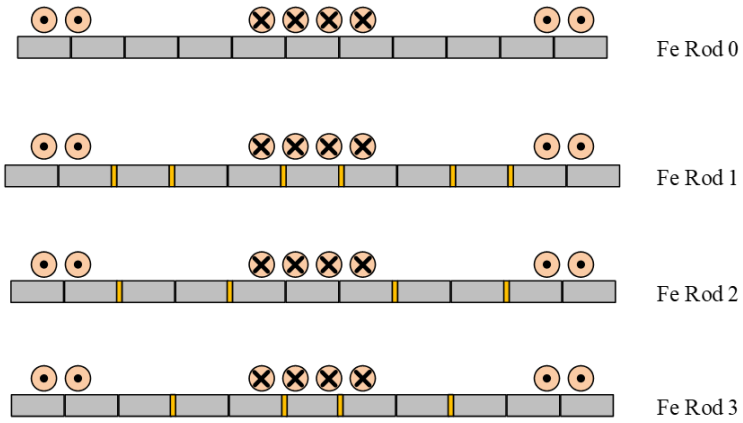

Fig. 4.8: Cross-sectional view of the primary coils and ferrite bars showing the three sample spacing configurations.

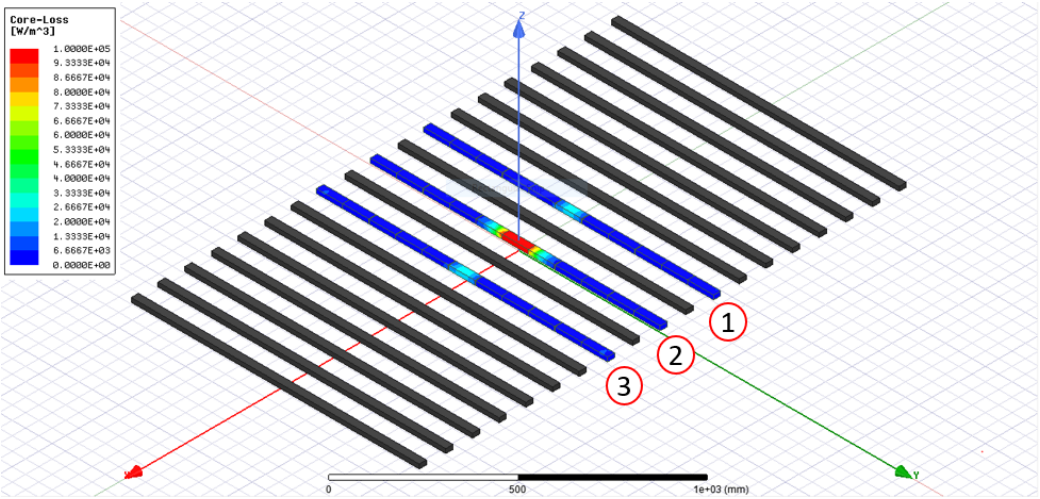

Fig. 4.9: Loss distribution in the three sample ferrite bars simulated in ANSYS Maxwell.

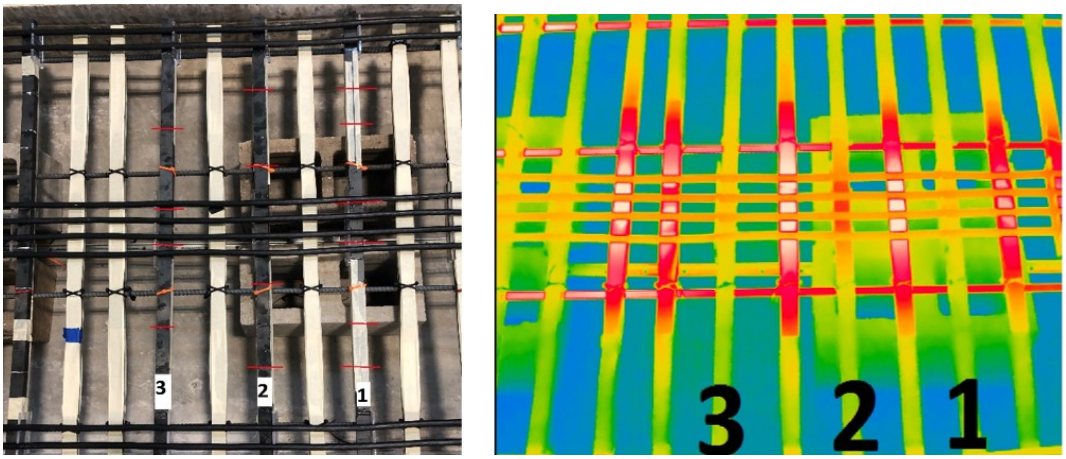

(a) (b)

Fig. 4.10: Close-up image of the primary pad showing the effects of different ferrite spacing configurations a) normal image b) thermal image.

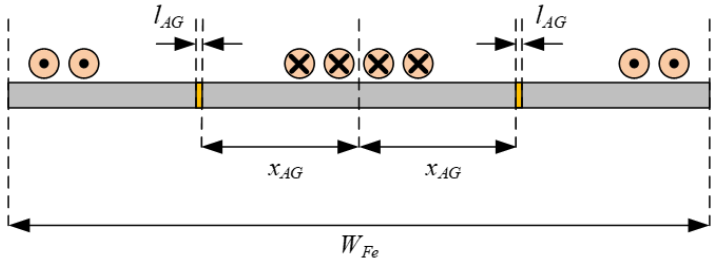

Fig. 4.11: Cross-sectional view of the primary coils and ferrite bars.

analysis are shown in Fig. 4.12 and Fig. 4.13.

Results for core loss and copper loss variation with a variation in x_{AG} and l_{AG} are shown for the fiberglass and steel reinforced pads in Fig. 4.12 and Fig. 4.13 respectively. Primary coil ESRs of 110 mΩ (with steel rebar) and 45 mΩ (with fiberglass rebar) are considered for this analysis. The ferrites have a combined volume of approximately 8831 cm^3 and the copper has a combined volume of approximately 1103 cm^3. While it is slightly advantageous to have higher loss in the ferrite compared to copper, the total amount of loss needs to be taken into consideration.

Passive thermal management

Passive thermal management refers to the method of heat dissipation without the

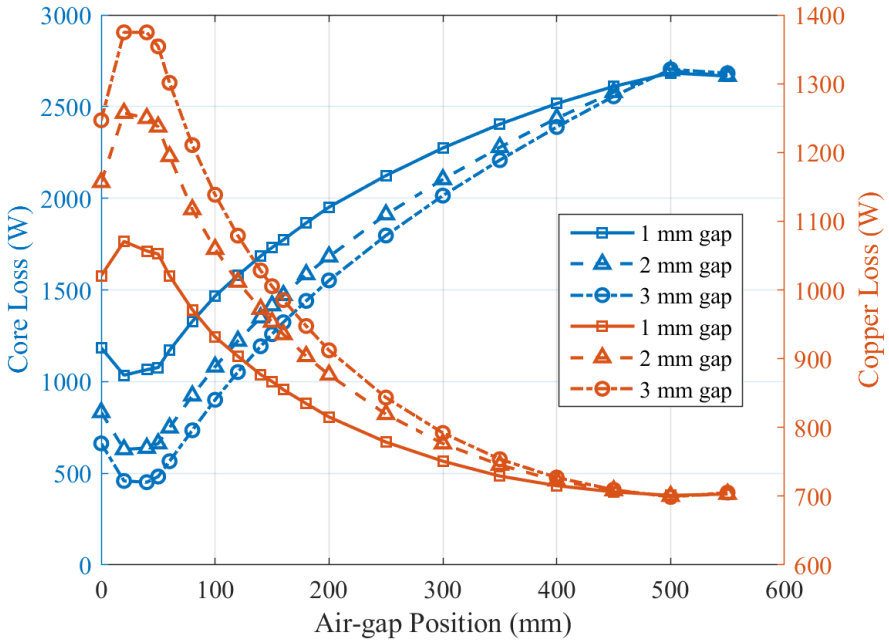

Fig. 4.12: Graph showing distribution of copper losses and core losses in the primary pad when the airgap size and position are varied while keeping the power transfer capability constant (ESR = 45 mΩ).

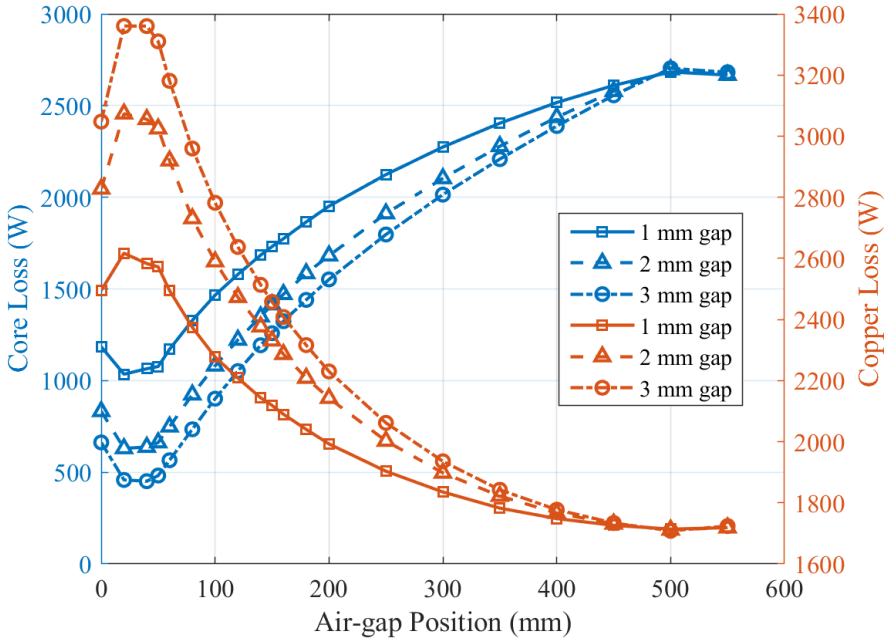

Fig. 4.13: Graph showing distribution of copper losses and core losses in the primary pad when the airgap size and position are varied while keeping the power transfer capability constant (ESR = 110 mΩ).

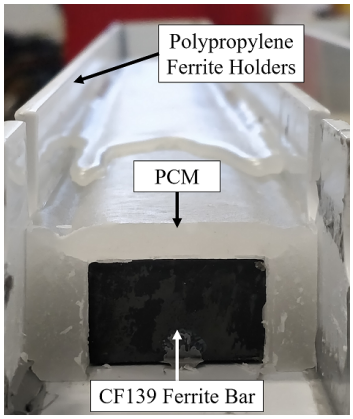

Fig. 4.14: Cross section of a CF139 ferrite bar covered in PCM.

use of external energy to affect the heat transfer process [92, 100]. In the present work, passive thermal management is achieved by the use of a phase-change material (PCM) [101]. Phase-change materials are substances which undergo a thermodynamic phase transition by releasing or absorbing thermal energy. Ferrite bars used in the primary pad are submerged in liquid PCM and then cooled to let the PCM solidify. The cross section of a PCM enclosed ferrite rod is shown in Fig. 4.14. The PCM absorbs transient thermal energy from the ferrites during power transfer and undergoes a phase transition from solid to liquid. This prevents localized hot-spots and large temperature gradients in the concrete structure. This is especially useful in DWPT systems due to the transient nature of system operation. The use of passive cooling methods in a large scale deployment can significantly reduce the total system cost when compared to active cooling methods.

4.1.7 Power Electronics Design

The inverter is designed using Cree/Wolfspeed CAS325M12HM2 power modules and a high current multi-layer printed circuit board. An operating frequency of 85 kHz is chosen, in compliance with existing standards for static inductive power transfer (SAE J2954).

An LCCL compensation as described in Section 2.2 is chosen for both the primary and secondary sides of the system. The component values of the primary and secondary compensation networks are given in Table. 4.3 and Table. 4.4.

Table 4.3: LCCL Compensation Values for the Primary Pad

Component	Value
L_{s0}	8.7 µH
C_{p0}	400 nF
C_{s0}	79 nF
L_{pri}	52.9 µH

Table 4.4: LCCL Compensation Values for the Secondary Pad

Component	Value
L_{s1}	4.9 µH
L_{s2}	4.9 µH
C_{s1}	3.7 nF
C_{s2}	3.7 nF
C_{s3}	1.4 nF
C_{s4}	1.4 nF
C_{p1}	827 nF
L_{sec}	6.8 µH

4.2 Hardware Development

Authors in [11] show that a knee point exists at approximately 15-20% DWPT road coverage and a 50 kW DWPT power level to achieve unlimited driving range using the Highway Fuel Economy (HWFET) drive cycle [102] and this data is shown in Fig. 4.15. The research presented in [11] models a Nissan Leaf as the vehicle of choice. Hence the data obtained is accurate in the case of similar light duty vehicles. However, in a real world DWPT implementation, utilization is expected to be shared between different vehicle classes to obtain the maximum possible return on investment. Authors in [86,87] perform a similar study with class 8 heavy duty trucks and other vehicles classes as well. The authors make use of geographically diverse data sets, validated vehicle models, real-world drive cycles, and variable vehicle adoption and infrastructure deployment rates. The authors conclude that a 50 kW power level is sufficient to satisfy the power requirements of different vehicle classes (when used in conjunction with multi-pad receivers for larger vehicles).

Based on the above discussion, a target power level of 50 kW is chosen for the purpose of this work.

Using the various design considerations outlined in Section 4.1, a DD shaped primary

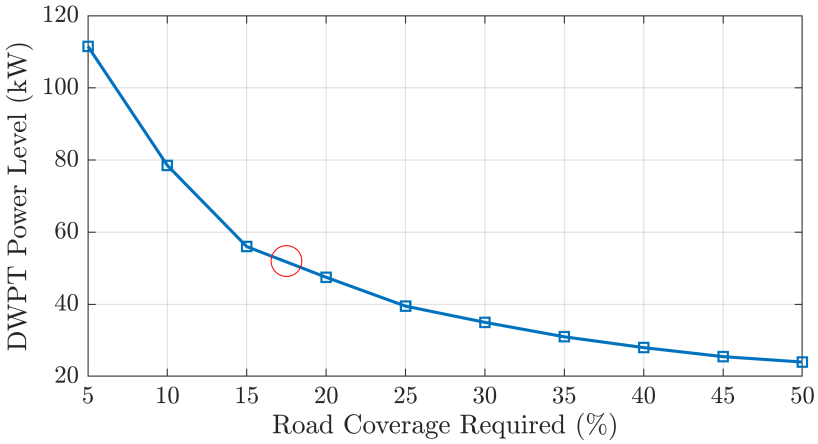

Fig. 4.15: Required DWPT power level to achieve unlimited range using the HWFET drive cycle [11].

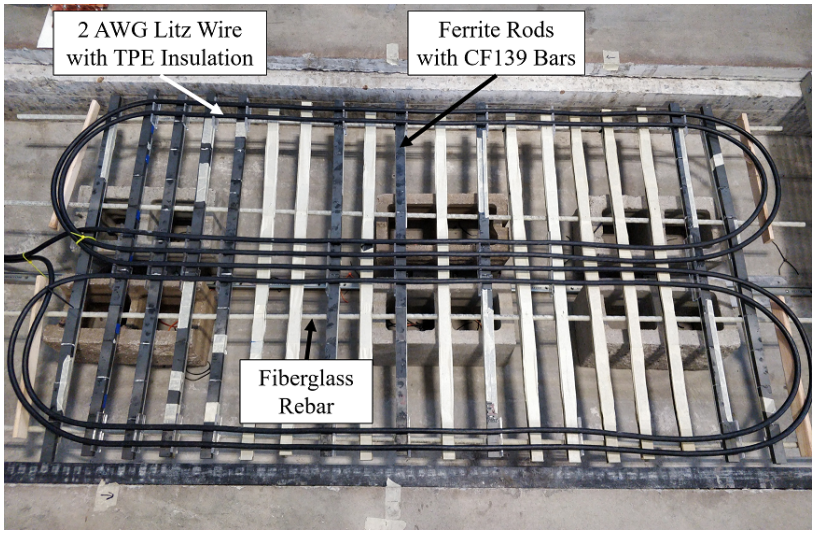

Fig. 4.16: Two-meter long concrete-embedded pad prototype.

pad is designed with two turns wound using 2 AWG Litz wire and ferrite bars along the direction of the flux path. A 2 m × 1 m DD coil is designed based on the above considerations as shown in Fig. 4.16. A lower-turn, high-current design is chosen to facilitate elongated coil designs for DWPT without significant voltage drop. A 2 AWG 5×5×5/34/38 type 2 Litz wire is chosen with a 2 mm thermoplastic elastomer (TPE) insulation jacket to protect against alkaline conditions inside the concrete pavement and increase distance between the copper Litz wire and concrete.

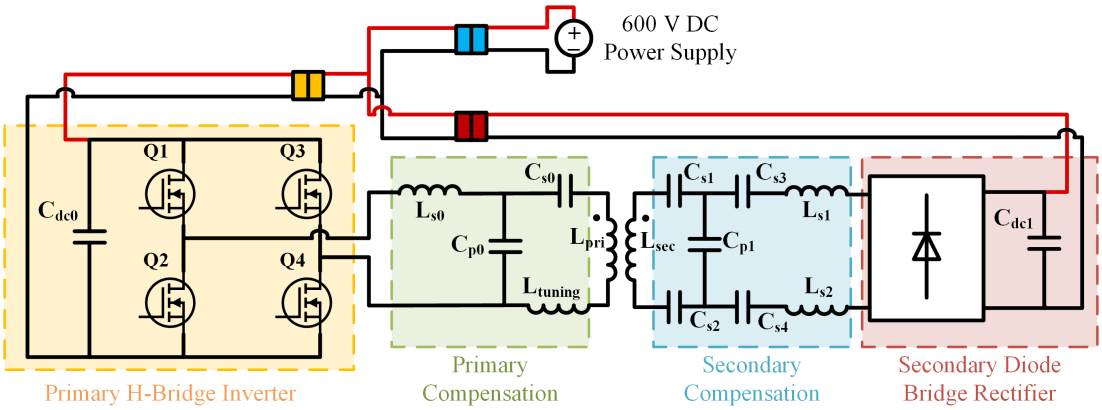

Fig. 4.17: System block diagram showing the circulating power test setup.

4.3 Test Setup

4.3.1 Circulating Power Test

An image of the hardware setup used for power electronics testing is shown in Fig. 4.18. The primary coil is covered under the grates and the secondary coil is mounted under a movable cart. To avoid dissipating a large amount of power and to reduce the system complexity, a circulating power setup is used to test the electronics. The system block diagram is shown in Fig. 4.17. The three power connectors (red, yellow and blue) used in the setup are the same as shown in Fig. 4.17. A DC bus voltage of 600 V is chosen as the input voltage and emulated output battery voltage. An extendable DC cable is used to connect the output of the secondary diode bridge rectifier to the primary DC link.

4.4 Results and Discussion

4.4.1 Wireless Power Transfer Tests

Results from the wireless power transfer tests are shown in Fig. 4.19. The primary side track RMS current is shown on the X-axis with DC-DC efficiency and output DC power shown on two different Y-axes. The results show efficiencies above 93% over the entire operating range of the system from 2 kW to 56 kW. Scope waveforms for the inverter output voltage (bridge voltage), primary track current and the DC output current are shown

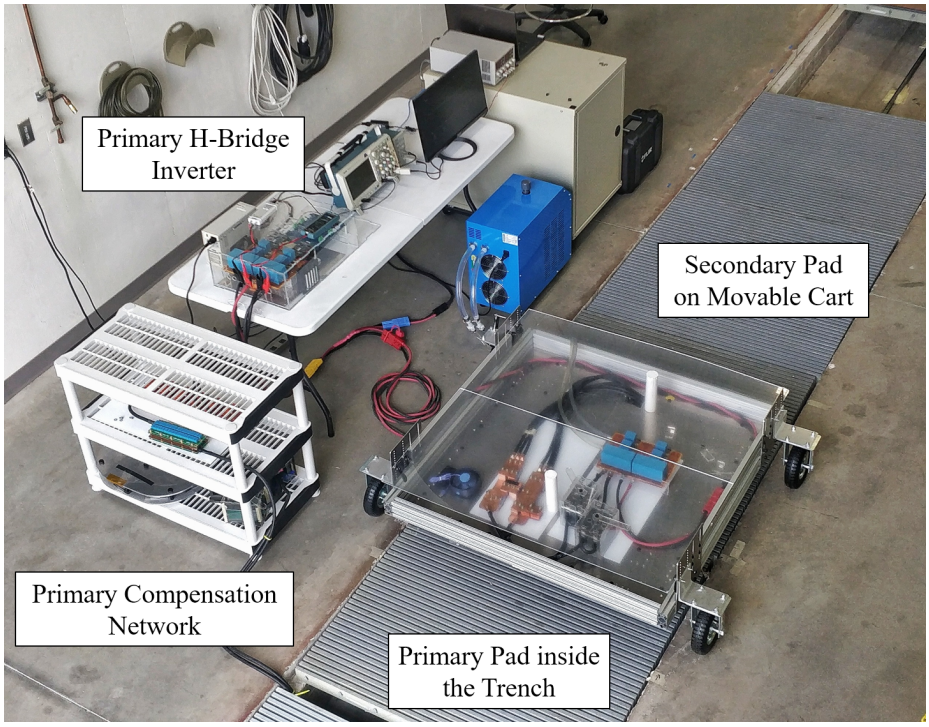

Fig. 4.18: Hardware test setup for testing the WPT system and the corresponding power electronics.

in Fig. 4.20. At a 110 A RMS track current at 85 kHz, the designed primary pad transfers 56 kW of power wirelessly across a coil-to-coil air-gap of 203.2 mm. The power variation in this test is achieved by adjusting the DC link voltage. Hence the nearly constant efficiency throughout the operating range. Power variation using a front-end DC-DC converter or other modulation schemes for the H-Bridge inverter would result in a more conventional efficiency profile.

4.4.2 Structural Testing

The structural properties of the concrete-embedded pad are tested using fatigue cycling and a three-point bending test. Strain measurements and other results of the structural tests are beyond the scope of this dissertation and can be found in [93]. Three concrete-embedded pad prototypes as shown in Fig. 4.21 are constructed and tested. The coil prototypes in Fig. 4.21 are half-length replicas of the pad shown in Fig. 4.16 and are embedded in lane width concrete slabs. The objective of fatigue cycling is to observe how the electrical

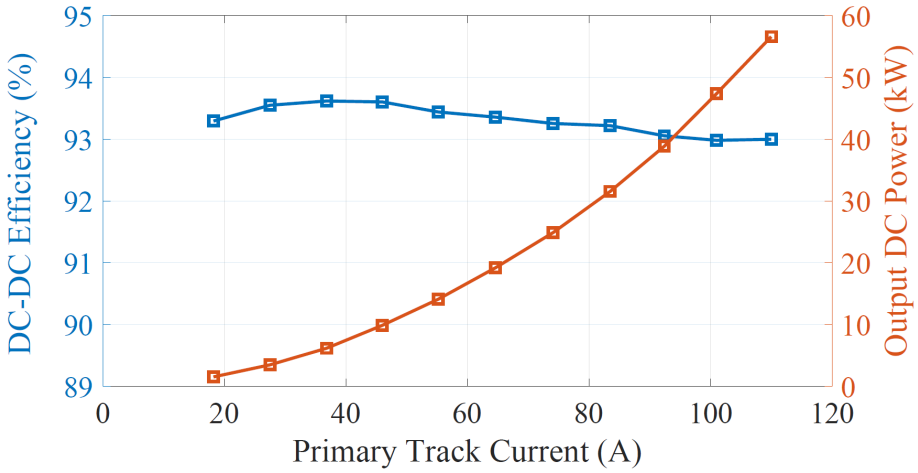

Fig. 4.19: Graph showing the DC-DC efficiency at various output power levels.

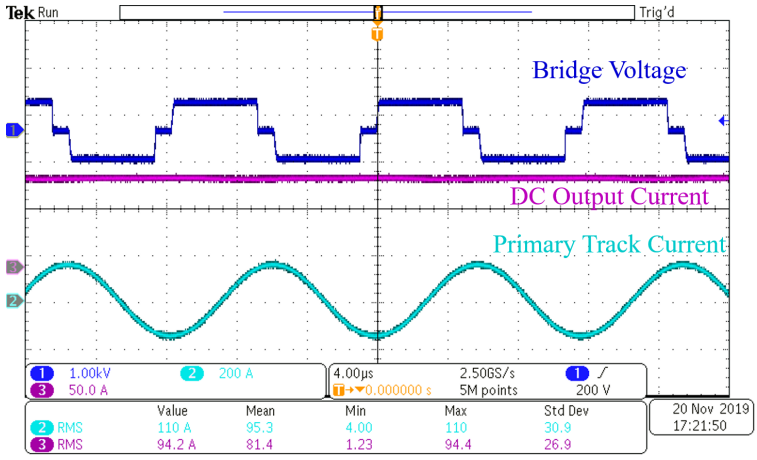

Fig. 4.20: Scope waveforms showing the inverter output voltage, track current, and DC output current in the system.

properties of the concrete-embedded pad vary with cyclical loading designed to emulate heavy-duty vehicular traffic. The three-point bending test is performed to observe how the DWPT behaves under extreme failure modes.

(a) (b)

Fig. 4.21: Three concrete-embedded 1 m x 1 m pad prototypes a) before concrete pours b) after concrete pours.

Fatigue Cycling Test

An image of the fatigue cycling test setup is seen in Fig. 4.22. The approximate location of the coil inside the concrete slab is also shown in the figure. The fatigue cycling test is designed to emulate the behavior of a vehicle driving over the concrete slab multiple times. The support beam is set to replicate the force distribution from the tires of the vehicle and the base used under the slab is identical to the sub-grade below a pre-cast concrete slab. The quality factor Q of the pad is measured throughout the duration of different fatigue cycling tests. The results are presented in Fig. 4.23. Three different loading conditions are tested as shown in Table. 4.5, where 32 kip emulates the force exerted on the concrete slab by a fully loaded semi-truck (1 kip = 4448 N).

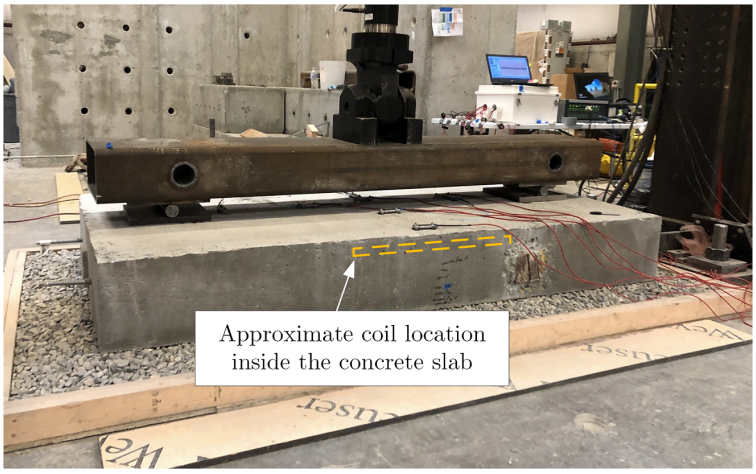

Fig. 4.22: Hardware test setup for testing the WPT system and the corresponding power electronics.

Table 4.5: Testing conditions for fatigue cycling

Test	Force	Cycles
Test 1	32 kip	300000
Test 2	50 kip	10000
Test 3	64 kip	6000

Three-Point Bending Test

The three-point bending test is performed to understand how the slab behaves under catastrophic failure. While this is unlikely to happen in a daily-use scenario, the results from this test provide information on how a pavement failure would affect the electrical system. Based on the variation in quality factor, preventative safety measures can be installed in place to prevent fault propagation through the electrical system in the event of a structural failure. Fig. 4.24a shows the approximate location of the coil inside the concrete slab.

Results from the three-point bending test are shown in Fig. 4.25 and Fig. 4.26. Fig. 4.25 shows a frequency sweep of the pad impedances measured before and after failure and Fig. 4.26 shows the variation in pad quality factor over the duration of the test. The abrupt change in Q immediately after slab failure is due to an increase in the pad ESR. The pad inductance is observed to still remain in the same range as before the test. This shows that the embedded wireless charging pad is still functional even after a catastrophic failure in the concrete slab. Further, the location and propagation of cracks in the slab indicate that

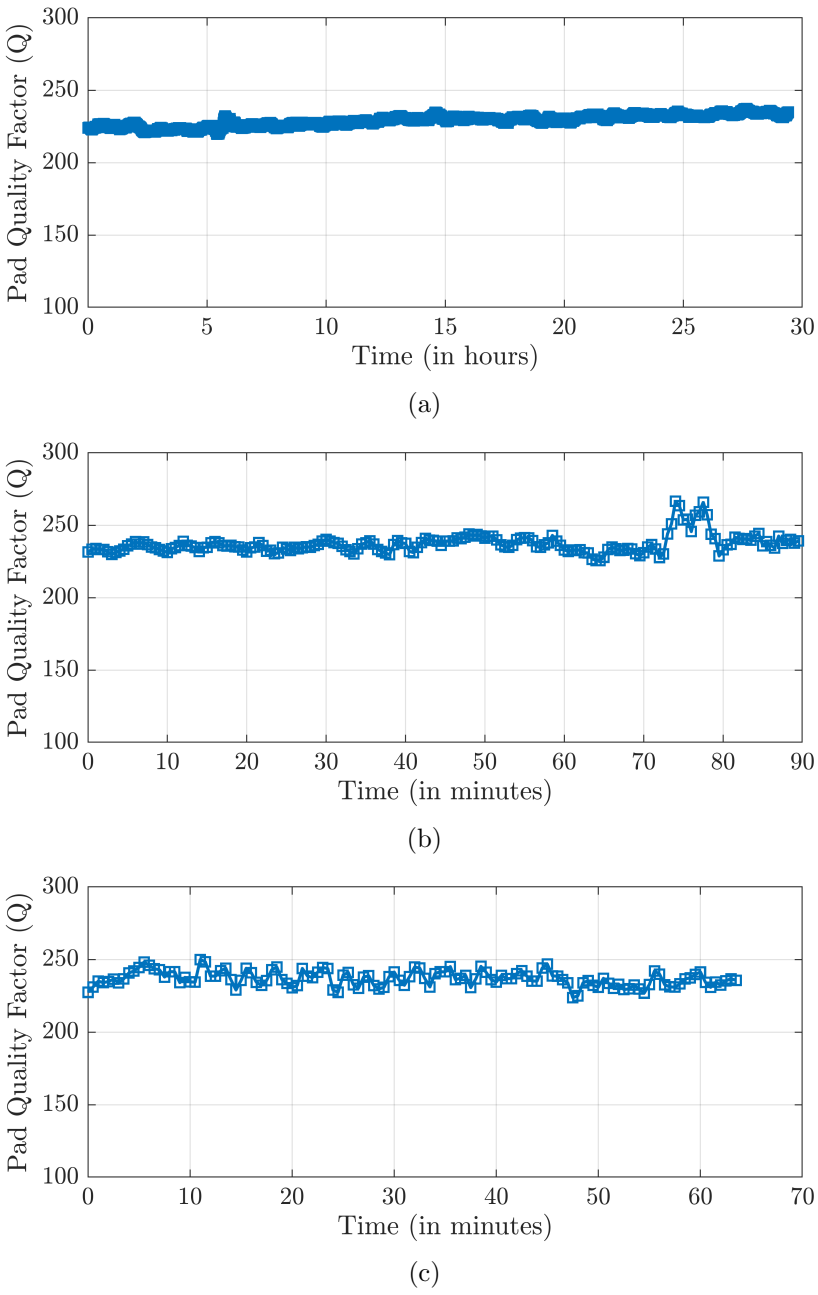

Fig. 4.23: Variation in pad Q over the duration of the fatigue cycling tested at a) 32 kip b) 50 kip c) 64 kip.

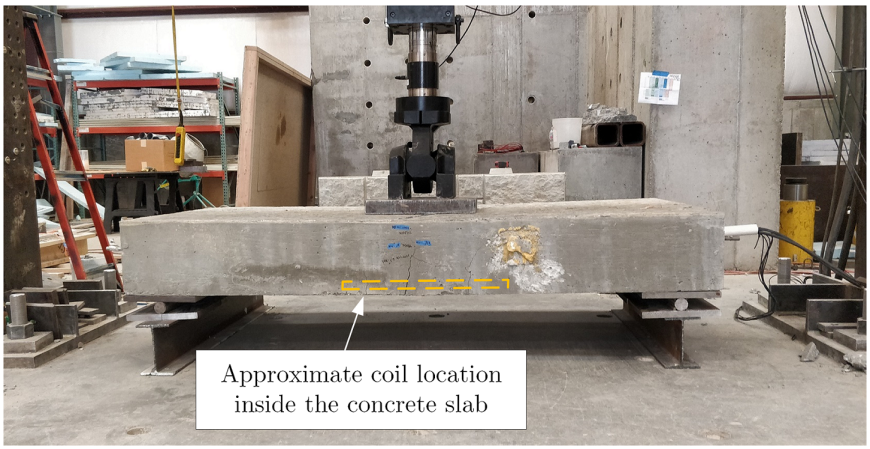

(a)

(b)

Fig. 4.24: Test setup used for the three-point bending test a) before pad failure b) after pad failure.

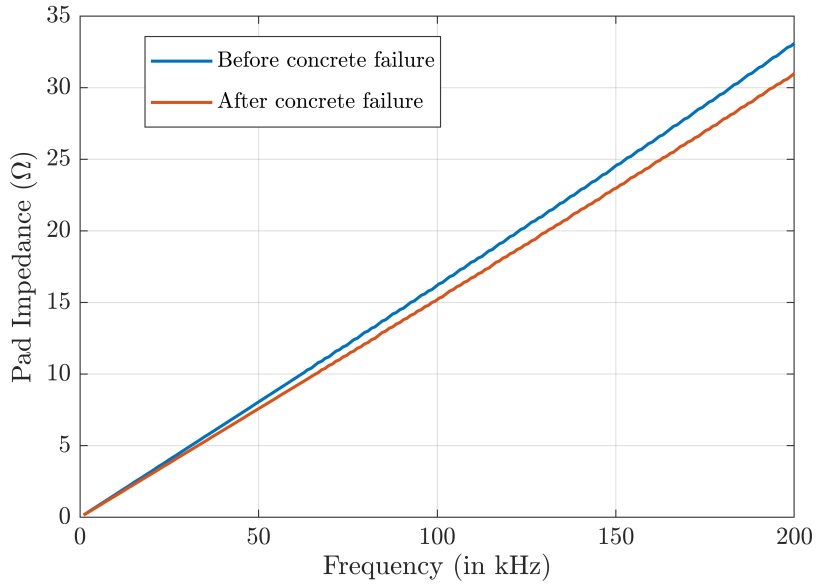

Fig. 4.25: Frequency sweep measurement of the concrete-embedded pad impedance before and after 3-point bending test failure.

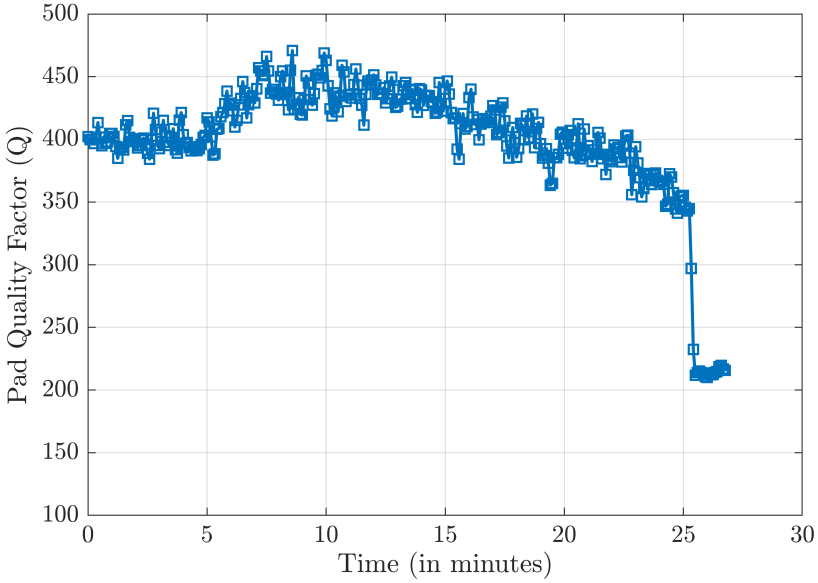

Fig. 4.26: Q measurement during the 3-point bending test.

the WPT coil provides some amount of additional reinforcement as well.

It should be noted that the initial pad quality factor Q is different in Fig. 4.23 and Fig. 4.25 due to the location of the primary pad inside the concrete slab and the orientation of the slab. In the fatigue cycling tests, the pad is closer to the top of the concrete slab and hence is closer to the loading ram and spreader beam which are both made of metal. This results in a lower Q compared to the three-point bending test, where the pad is closer to the bottom of the concrete slab.

4.4.3 Summary

The design of a fully functional pavement-integrated DWPT system is presented in this chapter. The designed system is tested under accelerated real world conditions to observe the characteristics of the system in the long-run. It is observed that the DWPT system functions as intended during all the structural testing and remains functional even after catastrophic failure. This is a significant improvement from prior implementations of pavement-embedded WPT pads.

CHAPTER 5

MULTI-PAD RECEIVER COILS

5.1 Design Considerations

Dynamic wireless power transfer (DWPT) technologies can recharge electric vehicles (EVs) while in motion [81, 94, 95]. This reduces range anxiety and helps increase EV adoption [103]. However, initial infrastructure costs for DWPT systems are significant due to the scale of deployment required [104–106]. These systems can become economically viable only when primary side (transmitter) infrastructure can be reused for different vehicle classes. Due to a wide range of power requirements, the use of modular standardized receivers is seen as a feasible solution [87, 107].

Larger vehicles typically have higher power requirements and greater energy consumption per mile [108]. The use of modular receiver pads makes use of this relation to ensure that the wide range of power needs are met for different vehicle classes. This work explores the use of modular receivers to scale the power transfer capability of dynamic wireless charging systems. An electric sports utility vehicle (SUV) is chosen as the test vehicle. WPT3 secondary pads as specified by the SAE J2954 standard are chosen to be used as individual modules in a multi-pad receiver [109]. The vehicle choice and choice of the secondary pad are arbitrary and chosen for ease of demonstration. Three elongated primary pads are used to generate the required alternating magnetic field at 85 kHz.

The wireless inductive power transfer system consists of three rectangular primary pads and three square WPT3 receiver pads specified by the SAE J2954 standard. The overlapping rectangular transmitter pads designed in [28] are used in this work and the transmitter design is fixed for all the analysis that follows. The three primary pads are capable of transferring 30 kW of power each. The system is intended to be a scaled down demonstration of the use of multi-pad receivers to vary the power level based on the vehicle

power requirements. The coupling coefficient (k) profiles between each of the three primary pads and each of the three secondary pads is as shown in Fig. 5.1. The simulated coupling coefficient (k) is less than 0.07. This is due to the primary pads being elongated and the individual receiver pads being much smaller than the primary pad.

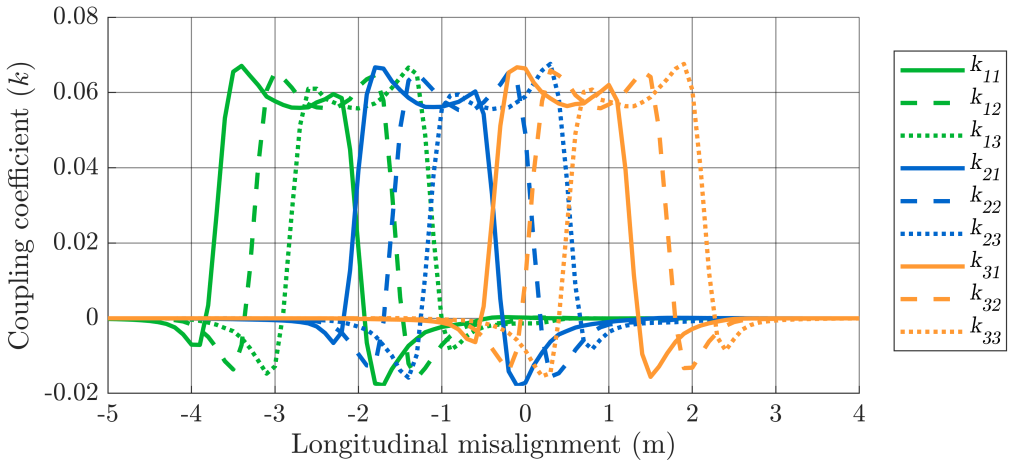

Fig. 5.1: Dynamic profiles for coupling coefficients between primary pads and secondary pads.

5.2 Connection Methods for Multiple Receivers

Multiple receivers can be connected in series, parallel or operated as independent receivers. Fig. 5.2 and Fig. 5.3 describe the three different connection methods for multiple receivers. This analysis considers only three secondary pads due to space constraints on the available light-duty vehicle, but can be extended to any number of secondary pads. Primary side control as specified by the SAE J2954 standard is assumed for all comparisons presented in this work [109].

5.2.1 Independent Receivers

Operating each receiver pad independently with three compensation networks and three rectifiers allows for a modular receiver system. One or more receivers can be disabled depending on the vehicle power requirements. This connection method adds significant system

complexity. To set a required power reference, the primary controller needs information on the number of individual receiver pads being energized. This further complicates control and requires a communication link between the primary and secondary sides of the system.

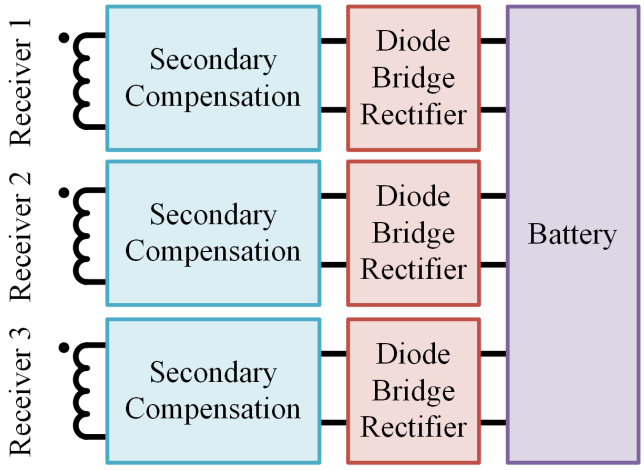

Fig. 5.2: Multi-pad receivers operating as independent receivers.

Advantages

Having independent receivers requires multiple smaller compensation networks and rectifiers to process the received wireless power. In stationary charging scenarios when only one or two receivers are coupled, depending on the shape and size of the available primary pad, the multi-pad receiver can be operated as a single pad receiver, minimizing losses in the other two receiver pads. Additionally, in DWPT systems, having independently operated receiver pads allows for scalable power transfer without having to adjust the primary side track current.

Disadvantages

In the event one or more receiver pads are damaged, the vehicle system needs to detect the failure and lower the desired total power level to ensure that each of the remaining receiver pads stay within their ratings. Similarly, coupling imbalances and tuning network

component tolerances can also contribute to a mismatch in receiver power.

In DWPT systems it is likely that the coupling between an energized primary pad to the individual secondary pads may be imbalanced. For instance, this can occur when a vehicle is driving onto a DWPT system, and some secondary pads are over the primary pad and others haven't reached the primary pad yet. In this case the power reference for the primary side power controller needs to reflect the number of receiver pads over the primary pad, i.e. the number of receiver pads with sufficient coupling to the primary pad. This information is difficult to estimate without accurate and low-latency vehicle position sensors. This complicates both primary and secondary side controls.

While independent receivers are expected to improve system efficiency and versatility, they would require complex sensing and control on the secondary side and are not analyzed in this chapter.

5.2.2 Series or Parallel Connected Receivers

Receiver pads can be connected in both series or parallel combinations to effectively form a larger receiver pad. The parallel and series connected multi-pad receivers are shown in Fig. 5.3a and Fig. 5.3b respectively.

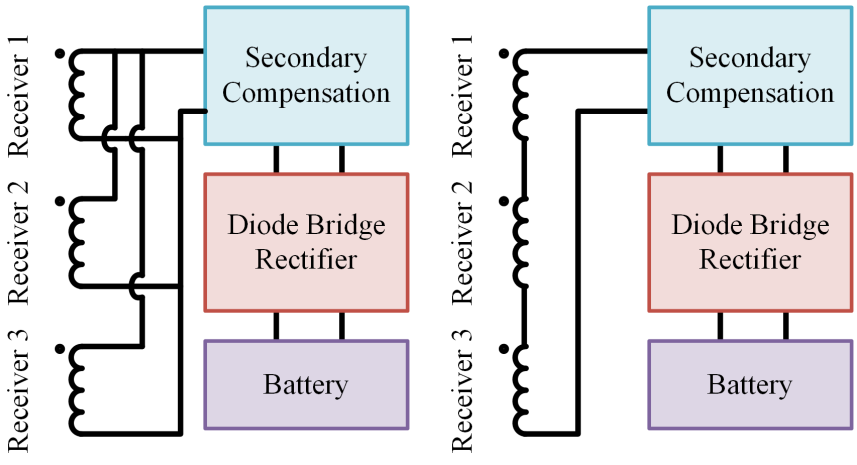

Fig. 5.3: Multiple receivers connected in a) parallel and b) series.

Advantages

Both parallel and series configurations simplify primary side control since they require only one power reference and can function even without a communication link between the primary and secondary sides of the system. When connected in series, all the receiver pads are forced to operate in phase since the same current flows through all the coils. The multi-pad receiver effectively behaves as an elongated single-pad receiver. With the parallel connection of receivers, the effective receiver pad voltage is lowered and thus simplifies the insulation and high voltage safety requirements.

Disadvantages

Parallel connected secondary pads have a difference in induced open circuit voltage (V_{oc}) due to the cross coupling between receivers and can cause issues with undesirable currents circulating between the secondary pads. In case of series connected secondary pads, when the car arrives on the first primary pad or leaves the last primary pad, all three modules of the multi-pad receiver are still energized even though they are not sufficiently coupled to the primary pad. All the modules have the same current flowing through them even when coupling is insufficient for a few of the modules to receive power. This can marginally decrease the energy efficiency of the system.

5.2.3 Analytical Comparison

Since the primary and secondary pad designs are fixed, the receiver pad open circuit voltage (V_{oc}) and the secondary side required power (P_{req}) are used to calculate the values of the secondary compensation network as described in (5.1) to (5.6) as follows

$$C_{\text{ser2}} = \frac{1}{\omega(Z_{\text{pad,sec}} - Z_{\text{ser,sec}})} \tag{5.1}$$

$$C_{\text{par2}} = \frac{1}{\omega(Z_{\text{par2}})} \tag{5.2}$$

$$L_{\text{ser2}} = \frac{Z_{\text{ser2}}}{\omega} \tag{5.3}$$

where the impedances $Z_{\text{pad,sec}}$, $Z_{\text{ser,sec}}$ and ω are defined as follows

$$Z_{\text{pad,sec}} = \omega L_{\text{sec}} \tag{5.4}$$

$$Z_{\text{ser,sec}} = Z_{\text{pad,sec}} + \frac{1}{\omega C_{\text{ser2}}} = \frac{V_{oc}}{I_{\text{br2}}} \tag{5.5}$$

$$\omega = 2\pi f \tag{5.6}$$

where I_{br2} is the diode bridge AC input current in order to charge the battery with the required power P_{req} (30 kW) and f is the operating frequency of the system (85 kHz). The secondary pad V_{oc} is measured when the primary pad is energized with nominal track current.

Table 5.1: Secondary Side LCCL Compensation Values for Series and Parallel Connected Multi-Pad Receivers

Component	Series	Parallel
C_{ser2}	32.24 nF	323.52 nF
C_{par2}	423.99 nF	1.40 uF
L_{ser2}	8.27 uH	2.49 uH

Table. 5.1 presents the compensation network values for both series and parallel connections when tuned to deliver the same output power of 30 kW to the receiver side battery. The simulated values for current and voltage stresses for each system are presented in Table. 5.2 and Table. 5.3. I_{rms}, V_{rms} and V_{pk} represent the root mean square (RMS) current, voltage and the peak voltage seen across each component in the compensation network respectively. Reactive power (S) which is used to compare the two compensation networks can be found as follows.

$$S = I_{\text{rms}} \times V_{\text{rms}} \tag{5.7}$$

The reactive power presented in (5.8) does not take into account the shape of the voltage waveforms. The presence of a higher peak in the voltage waveforms requires appropriately sized capacitors. Therefore, the $V_{\text{pk}}I_{\text{rms}}$ metric is used to compare the capacitor banks. This takes into account the peak voltage stress on a particular capacitor bank in addition to the RMS current flowing through it.

Table 5.2: LCCL Compensation Network Sizing for Series Connected Multi-Pad Receiver

	I_{rms} (A)	V_{rms} (V)	V_{pk} (V)	S (kVA)	$V_{\text{pk}}I_{\text{rms}}$(kVA)
L_{sec}	75	4802	6837	360.15	512.78
C_{ser2}	75	4374	6215	328.05	466.12
C_{par2}	123	541	778	66.54	95.69
L_{ser2}	85	395	886	33.57	75.31

Table 5.3: LCCL Compensation Network Sizing for Parallel Connected Multi-Pad Receiver

	I_{rms} (A)	V_{rms} (V)	V_{pk} (V)	S (kVA)	$V_{\text{pk}}I_{\text{rms}}$(kVA)
L_{sec}	245	1795	2575	439.77	630.88
C_{ser2}	245	1417	2018	374.16	494.41
C_{par2}	292	388	572	113.30	167.02
L_{ser2}	89	173	479	15.40	42.63

It is observed that for the simulated system, the series connected multi-pad receiver is the better solution due to lower reactive power requirements on the compensation network elements. Additionally, in the parallel configuration, the presence of high currents in the inductors L_{sec} and L_{ser2} requires a high gauge litz wire or a multi-filar winding with multiple current paths connected in parallel. This introduces practical challenges such as a larger bend radius and uneven current sharing in the parallel paths and requires complicated interleaving in order to resolve these challenges. Considering the above factors and also a lower $V_{\text{pk}}I_{\text{rms}}$ on the elements C_{ser2} and C_{par2}, the series connected multi-pad receiver is

chosen for hardware implementation and is presented in the Section 5.4.

5.3 Simulation Models

The series and parallel connection methods for multi-pad receivers are simulated in PLECS to understand the trade-offs between the two. The system is modeled using the methods presented in Chapter 3. The simulation model is experimentally validated using the series connected multi-pad receiver.

Simulation models of the wireless power transfer system are modeled in ANSYS, PLECS and LTSpice. The inductance matrix and coupling coefficients of the three primary pads and three secondary pads are obtained from ANSYS. These dynamic profiles are fed into a PLECS simulation model and simulated along with the power electronics and compensation networks. Nominal operating point simulations are performed in LTSpice to fine tune compensation networks and analyze system transients.

5.3.1 ANSYS Maxwell

Three independent receiver pads and three transmitter pads are simulated in ANSYS with an optimetric sweep to simulate the dynamic profile of the inductance matrix. The 3D model used for simulation is shown in Fig. 5.4.

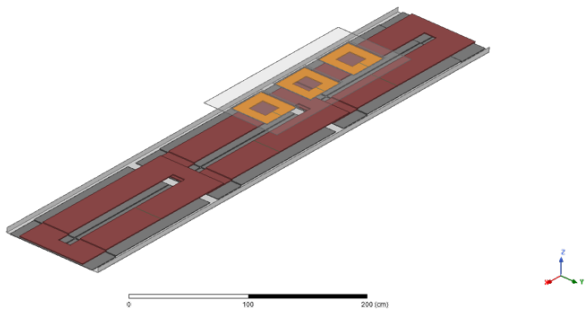

Fig. 5.4: DWPT system modeled in ANSYS Maxwell for FEM simulation.

5.3.2 PLECS

The DWPT system is modeled in PLECS using ideal switches and diodes. The resonant networks are modeled as ideal elements in series with their equivalent series resistances (ESRs). The values of these ESRs are obtained using a Hioki IM 3536 LCR meter. A screenshot of the PLECS simulation model is shown in Fig. 5.5.

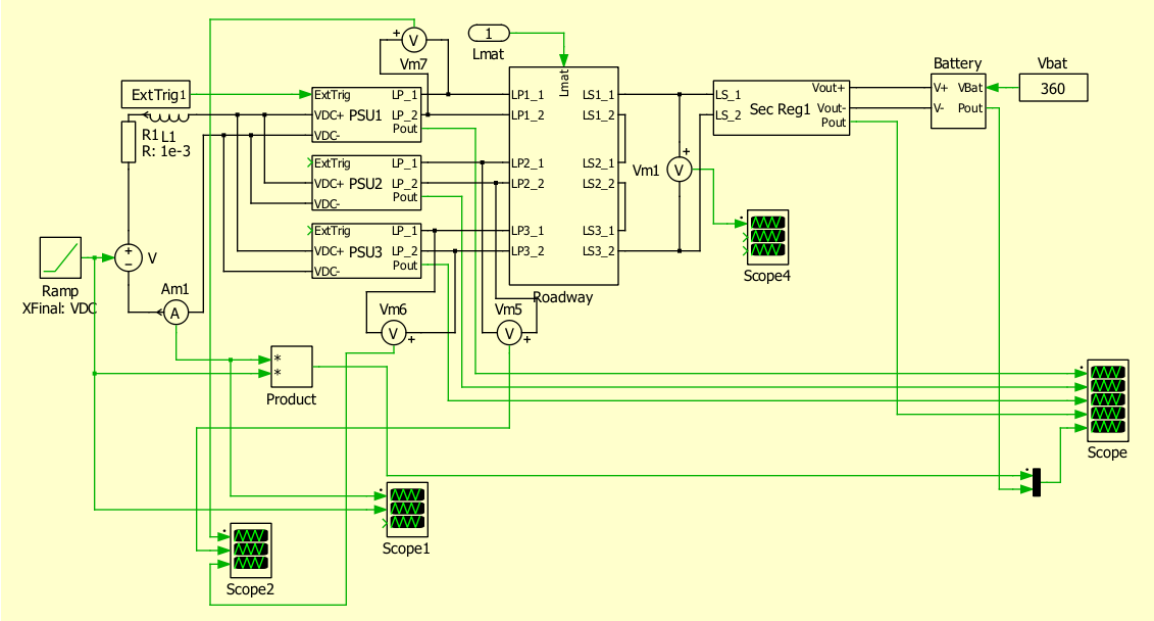

Fig. 5.5: DWPT system modeled in PLECS for circuit simulation.

5.3.3 LTSpice

A circuit simulation is designed to evaluate the current and voltage stresses on the coils at various operating points. This simulation does not consider the dynamic profile of coupling between the primary and secondary coils. The coupling coefficient k can be adjusted in the simulation to obtain the various voltage and current stresses on different components in the system. Screenshots of the LTSpice simulation are shown in Fig. 5.6 and Fig. 5.7. The input DC source is modeled as a 600 V voltage source along with cable parasitics. The DC output of the rectifier on the secondary side is modeled as a 360 V DC source.

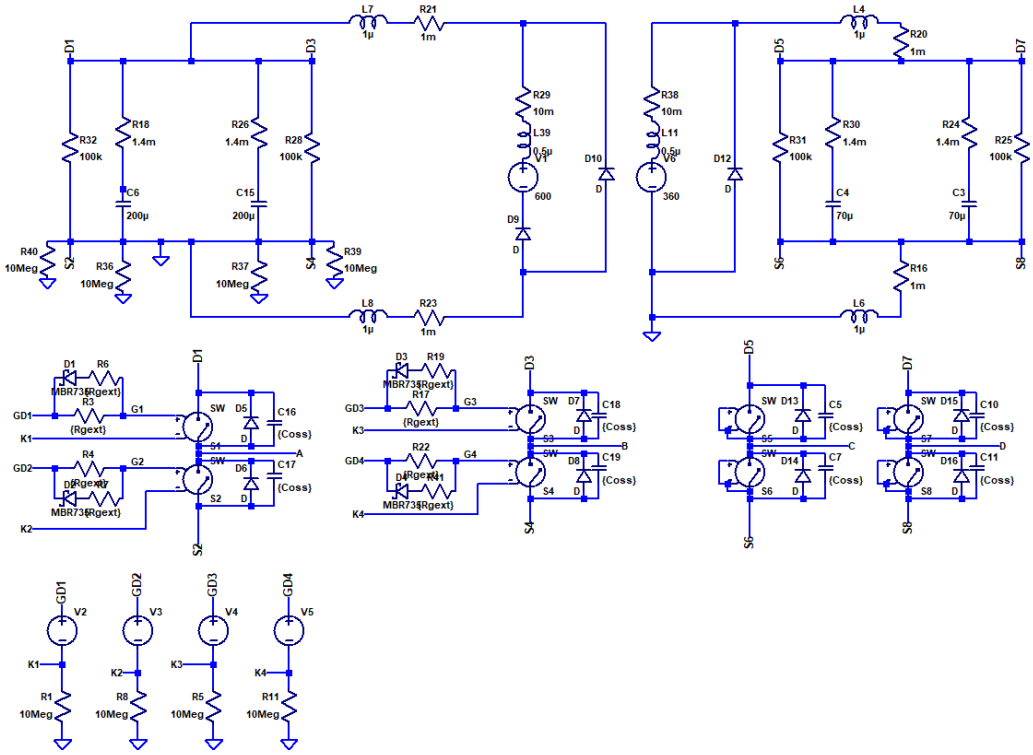

Fig. 5.6: H-bridge inverter and rectifier model in LTSpice to simulate the WPT system.

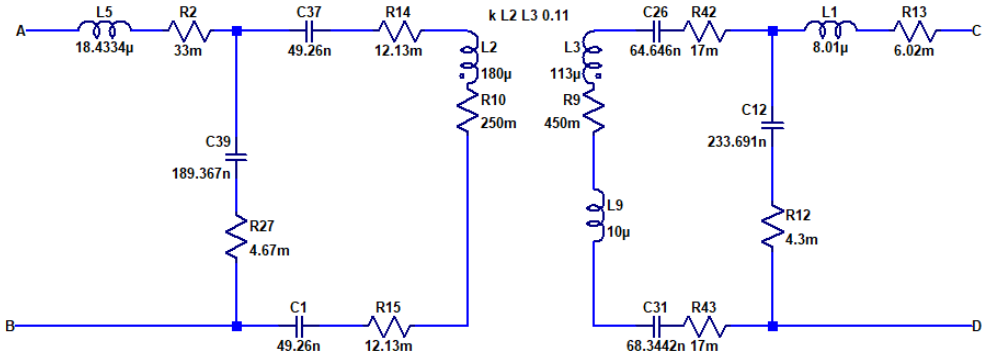

Fig. 5.7: Primary and secondary resonant tank model with constant coupling coefficient.

The three receiver pads can be connected in series or parallel as shown in Fig. 5.3. A screenshot of the simulation model with the series connection and the resultant V_{oc} waveform are shown in Fig. 5.8a and Fig. 5.8b respectively. Similarly the three receivers are connected in parallel as shown in Fig. 5.9a and the corresponding V_{oc} simulation is shown in Fig. 5.9b. The performance of series and parallel connections is evaluated by simulating the open

circuit voltage obtained at the input of the secondary compensation network. It is observed that the obtained open circuit voltage is three times higher for the series connection when compared to the parallel connection. This indicates that the effective mutual inductance between the primary pads and the secondary receiver arrangement is the same in both the series and parallel configurations.

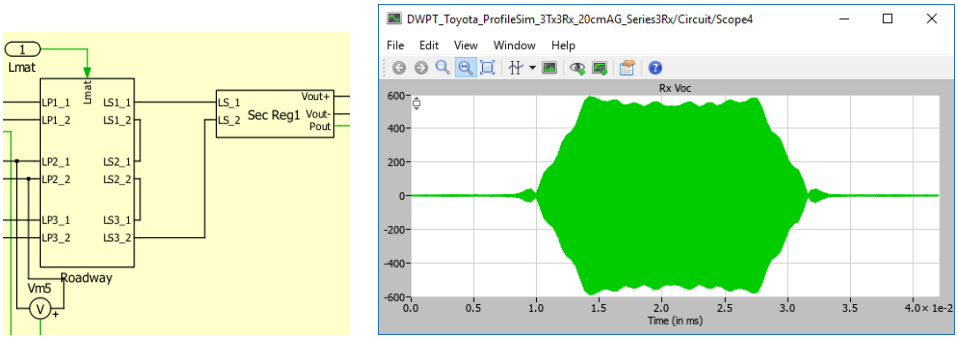

(a) (b)

Fig. 5.8: Series connected three-pad receiver a) PLECS schematic b) V_{oc} waveform.

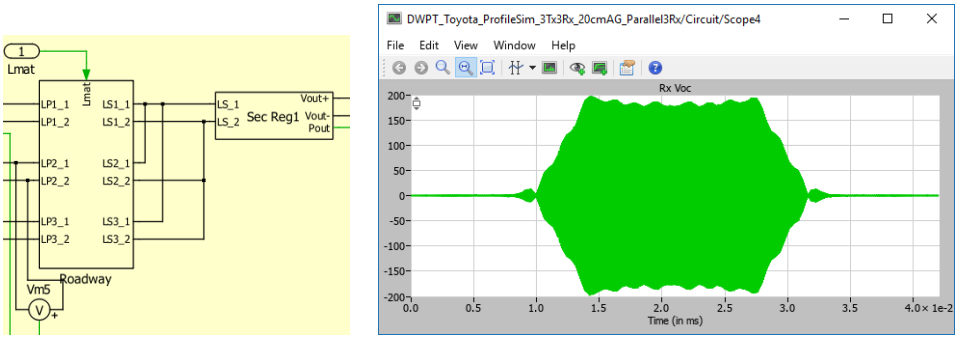

(a) (b)

Fig. 5.9: Parallel connected three-pad receiver a) PLECS schematic b) V_{oc} waveform.

The multi-pad receiver system is simulated in Simulink/PLECS using time-varying mutual inductance profiles. The detailed self- and mutual inductance values for different longitudinal misalignments are obtained from ANSYS Maxwell. The three receivers are connected in series configuration and the total inductance of the three receivers is shown

as L_{sec} in Fig. 5.10, which shows one primary pad and the secondary multi-pad receiver. To make a fair comparison between the two configurations, the output power is required to remain the same in both cases. The secondary LCCL compensation networks in the series and parallel configurations are tuned accordingly. The primary LCCL compensation values are shown in Table. 5.5. The primary pad compensation network is tuned to supply a constant track current of 43 A, which is the nominal value required for 30 kW power transfer to the secondary side battery load.

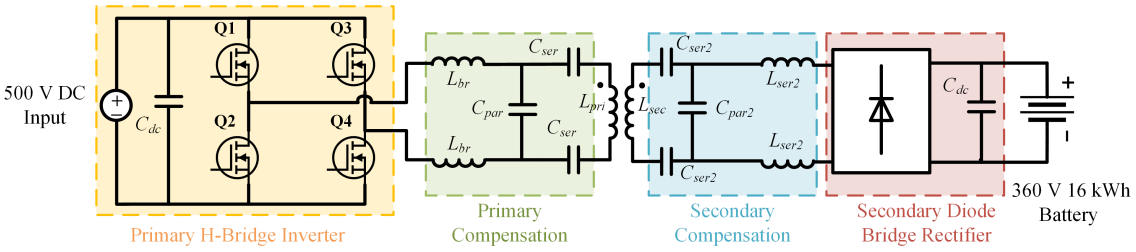

Fig. 5.10: Wireless power transfer system overview.

As explained in Section 5.2.2, both the series and parallel connections have their advantages and disadvantages. The decision to pick one over the other depends on practical considerations such as current and voltage stresses on the compensation network and optimal sizing of the compensation elements.

The simulated secondary side battery current waveform is shown in Fig. 5.11. The simulated current profile shows dynamic power transfer to the multi-pad receiver at a vehicle speed of 1000 mph (1600 km/h) with the battery current set to be 360 V. The profile can be scaled down to match realistic vehicle speeds while keeping the shape constant. The unrealistic vehicle speed is used to speed up the DWPT circuit simulation in PLECS.

5.4 Hardware Development

The individual primary pads each have a self-inductance of 175 µH and each module of the three-pad receiver has a self-inductance of 40 µH. The coupling coefficient (k) profiles between the primary pads and the secondary pads are shown in Fig. 5.1. In Fig. 5.1, k_{mn}

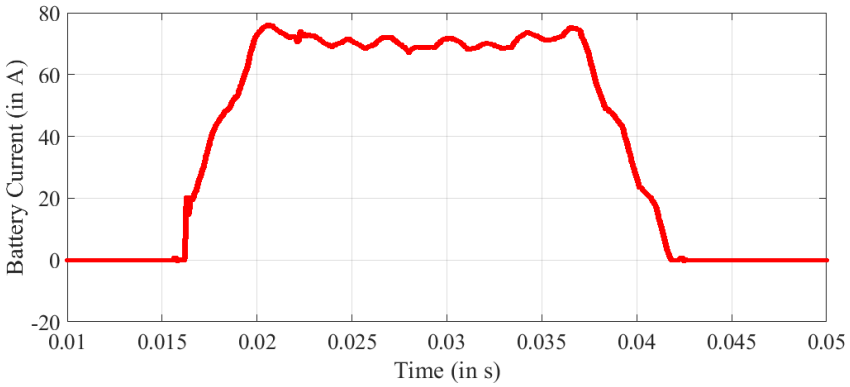

Fig. 5.11: Simulated battery current waveforms showing dynamic power transfer to the multi-pad receiver.

denotes the coupling coefficient between the m^{th} primary pad and the n^{th} secondary pad. Similarly, M_{mn} denotes the mutual inductance between the m^{th} primary pad and the n^{th} secondary pad. The coupling coefficient is defined as follows [89]

$$k_{ps} = \frac{M_{ps}}{\sqrt{L_p L_s}} \tag{5.8}$$

where L_p and L_s are the self-inductances of the primary and secondary coils respectively and M_{ps} is the mutual inductance between them.

While the coupling coefficient in Fig. 5.1 is low, the mutual inductance still remains sufficiently large for the required system, owing to the higher self-inductances of the elongated primary pads. The nominal mutual inductance between individual primary and secondary pads is estimated to be 5.5 µH.

The measured self-inductance for the three primary pads is shown in Table 5.4. The measurements are obtained using a Hioki IM 3536 LCR meter. This measurement includes the additional inductance due to cables going from the trench into the cabinet inside the shed. The variation in the self-inductances of the three pads is due to the variation in cable lengths routed from the shed to the trench in the test track. These variations are tuned out by making adjustments to the three primary compensation networks.

The system overview showing the arrangement of three primary and secondary pads

Table 5.4: Primary Pad Self-Inductances

	L_{pri} (μH)
Pad 1	171.45
Pad 2	177.86
Pad 3	181.59

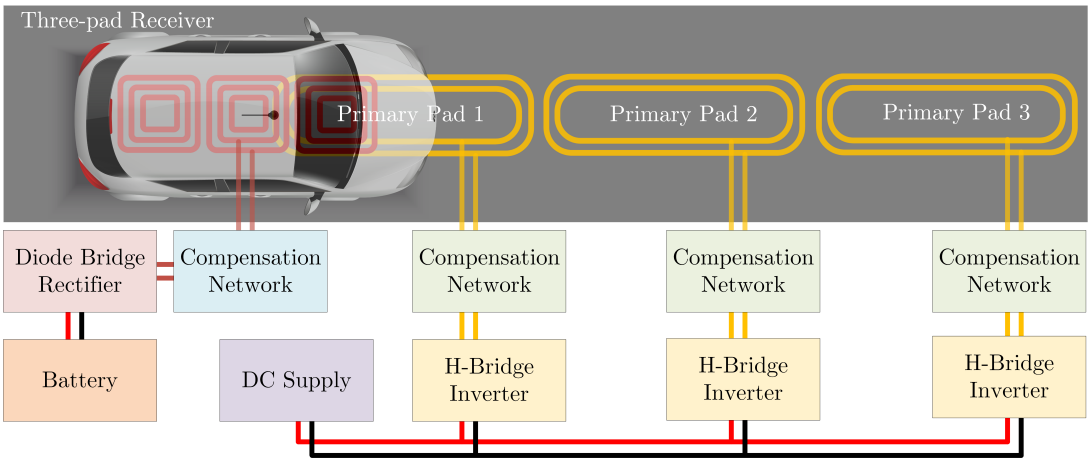

Fig. 5.12: System overview with three transmitter pads and a three-pad receiver.

can be seen in Fig. 5.12 and an overview of the wireless power transfer system is shown in Fig. 5.10.

5.4.1 Vehicle Detection System

The RFID vehicle detection system consists of a Raspberry Pi 3 B+, ThingMagic USB Pro, and Laird S9025PL RFID antenna. The program for the system utilizes the "RPI.GPIO" library and a python wrapper for the ThingMagic USB Pro API. The system works by constantly polling for a specific electronic product code (EPC), which corresponds to the RFID tag on the vehicle. When the vehicle is detected reliably, a signal is sent over a wireless communication link to the controller of the first primary pad to start its detection mode. The distance of the RFID antenna from the start of the first primary pad determines how early the first primary pad turns on. The RFID vehicle detection hardware is shown in Fig. 5.13.

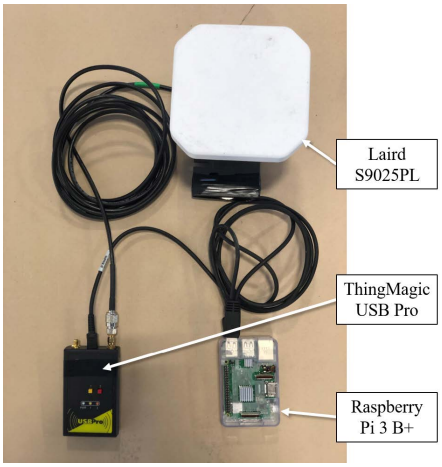

Fig. 5.13: Hardware used for the vehicle detection system.

5.4.2 Compensation Networks

The secondary series compensation capacitors (C_{ser2}) are placed close to the receiver pads to decrease the length of high voltage cabling required. These capacitors are mounted close to the receiver pads and placed in an acrylic water resistant enclosure as shown in Fig. 5.14. The C_{ser2} capacitor bank is also distributed between the three pads to avoid a large voltage from building up at any two terminals on the receiver system. The leads are terminated and connected to obtain a series combination of the three secondary pads and the distributed series compensation capacitor bank. The two leads coming from the receiver pads and series compensation caps are terminated with an Anderson power connector (blue) for quick connection and disconnection in case the system needs to be modified.

Similarly, on the primary side, the series compensation capacitors shown in Fig. 5.15 are placed in a weather proof enclosure under the primary pads. This reduces the amount of high voltage cabling required from the shed cabinets to the trench.

The primary side compensation network consists of a series inductor (L_{br}), parallel capacitor (C_{par}) and series capacitor banks (C_{ser}). All the primary and secondary compensation capacitor banks are built using standard capacitor values available. Illinois Capacitors HC1, HC2, HC3, HC4 and HC6 series of capacitors are used for the compensation network. The details regarding primary compensation network are given in Table 5.5.

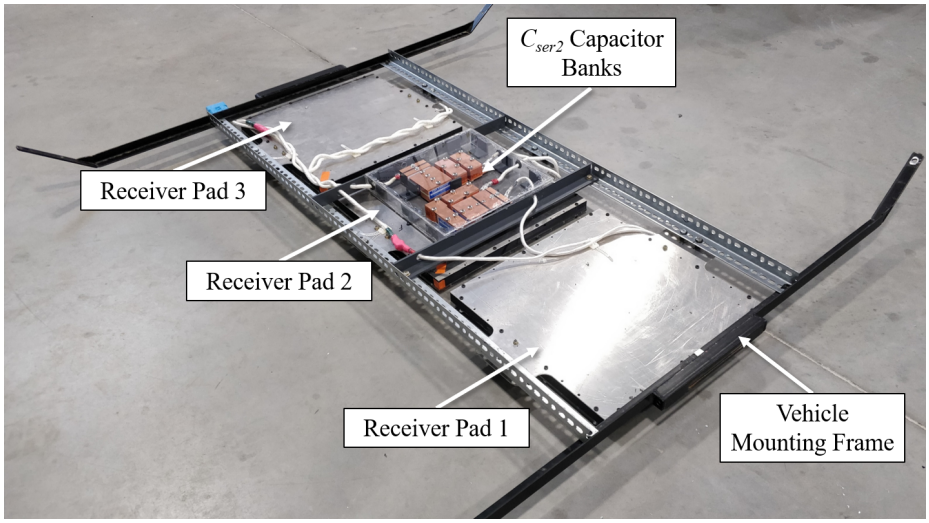

Fig. 5.14: Three receiver pads connected in series with compensation capacitors - top view.

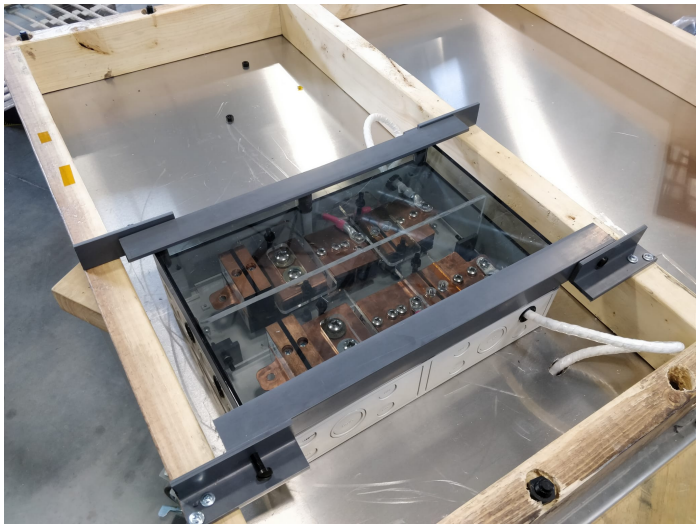

Fig. 5.15: Series compensation capacitors mounted under the primary pad.

5.4.3 Pad Weatherproofing

The three primary pads are embedded in a thermally conductive polyurethane epoxy (Epoxies 50-2151 FR) to protect it from dust, debris, rain and snow. Each pad is potted in two steps to allow pad overlap even after potting. The fully potted primary pads are shown in Fig. 5.16. The epoxy is chosen for its curing properties and good thermal conductivity. Since the pads have restricted air-flow after being potted, it is essential that the epoxy is thermally conductive in order to move heat away from the coil and ferrites. However, due to

Table 5.5: LCCL Compensation Values for the Primary Pad

Component	Value
L_{br}	8.7 µH
C_{par}	189 µF
C_{ser}	49 µF

Fig. 5.16: Three primary pads potted and placed in the outdoor trench.

the transient nature of dynamic wireless charging and efficient turn-on and turn-off of the primary pads during system operation, no significant thermal challenges are encountered.

5.5 Transmitter Power Electronics

The transmitter side power electronics include the primary series capacitors, the primary parallel capacitor, the primary series inductor, the inverter and the cooling system. In addition to these, the primary side electronics also consist of a controller board and current sensors to detect the DC input current going to the inverter and the AC inverter output. Excluding the primary pad and series compensation capacitors, the rest of the electronics are placed in a cabinet inside a shed. Three primary side power electronics assemblies are

mounted inside the cabinet and connected to each of the three primary pads as shown in Fig. 5.17. An image of the shed, test track, and vehicle used is as shown in Section 5.7

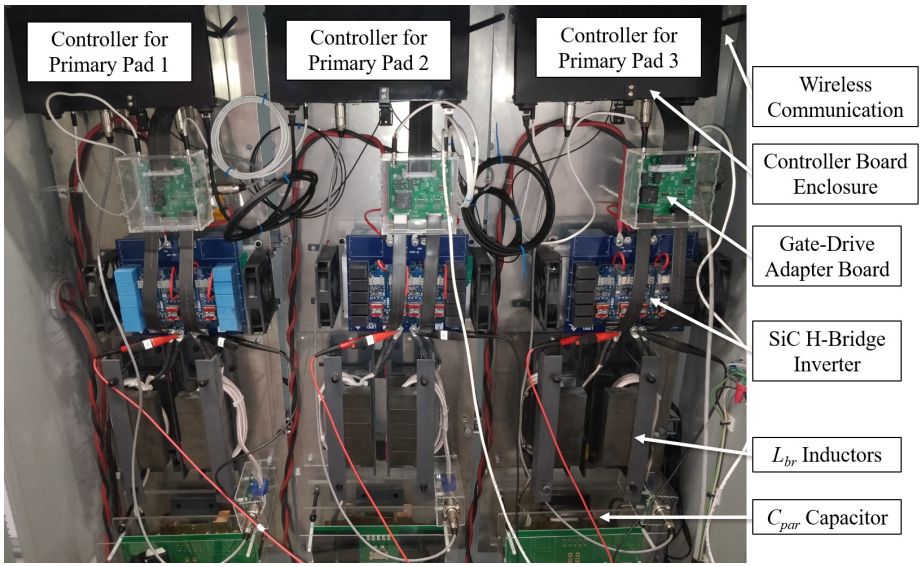

Fig. 5.17: Primary side electronics and compensation network.

5.6 Receiver Power Electronics

The receiver side power electronics includes the secondary series capacitors, the secondary parallel capacitor, the secondary series inductor, the diode bridge rectifier and cooling system. Individual receiver pads are constructed according to WPT3 specification (rated to 11.1 kVA) described in the SAE J2954 standard [109]. The receiver pads and the series compensation capacitors are mounted under the vehicle as shown in Fig. 5.18. The remaining elements of the secondary side power electronics system are mounted inside the vehicle as shown in Fig. 5.19. The DC output of the diode bridge rectifier is directly connected to an Orion battery management system (BMS) unit interfaced to the high voltage battery.

5.7 Testing and Results

To validate the simulation model developed and to experimentally test the three-pad receiver, the following hardware setup shown in Fig. 5.20 is developed. Three elongated

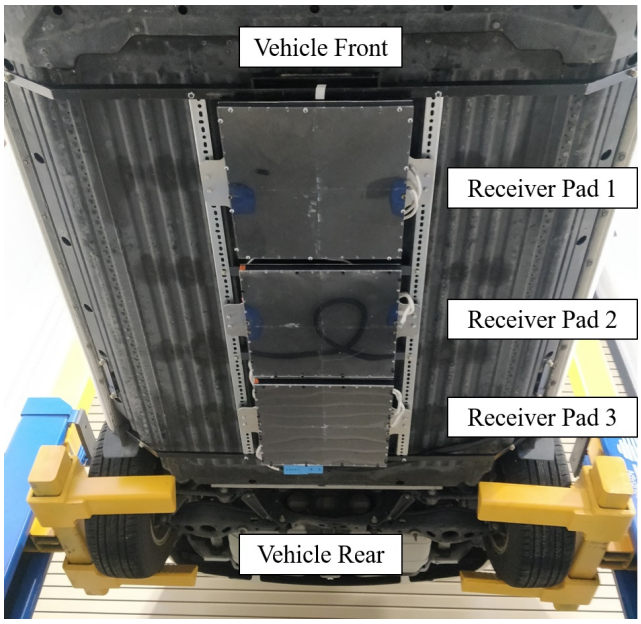

Fig. 5.18: Three receiver pads and series compensation capacitors mounted to the EV - bottom view.

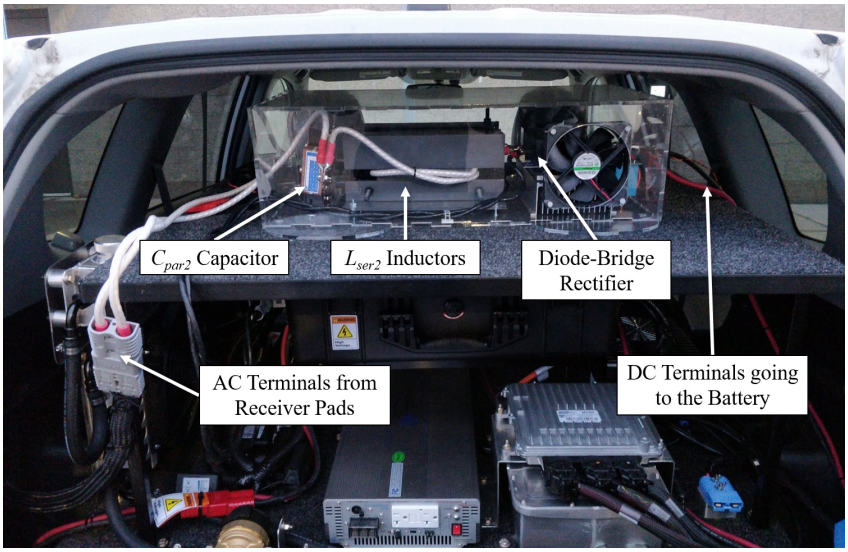

Fig. 5.19: Secondary side electronics and compensation network inside the vehicle.

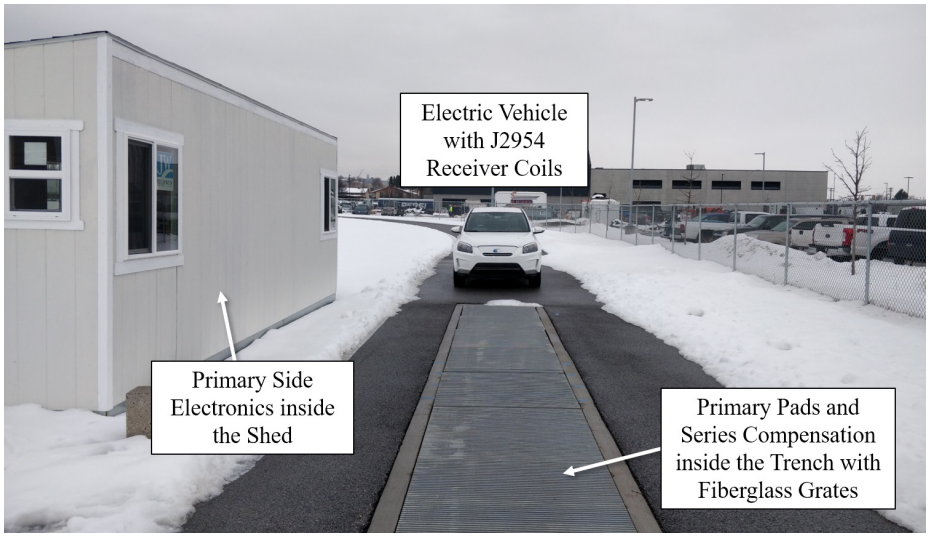

Fig. 5.20: Hardware DWPT system overview.

rectangular transmitter pads form a primary track which is 5.15 m long. The air-gap between the primary and secondary coils is set to be 200 mm from the bottom of the receiver pad to the top of the primary pad. This value is calculated based on the vehicle ground clearance and depth of the primary pad inside the roadway and the system is designed accordingly.

5.7.1 Track Current Tests

The system is energized without the receiver side present on the track. This test verifies the primary side tuning between the series inductor and the parallel capacitor. A well-tuned primary compensation generates a sinusoidal current source through the primary pad and series compensation capacitors. The waveform in Fig. 5.21. shows the track current, inverter output current and voltage during a track current test. The test is performed with DC input voltage of 600 V. Based on the design of the primary compensation network, a track current of 56 A is expected. This can be calculated as explained in Section 2.2. The primary electronics and test setup inside the shed are shown in Fig. 5.22.

5.7.2 Open Circuit Voltage Tests

The simulated mutual inductance profile can be validated by performing the open

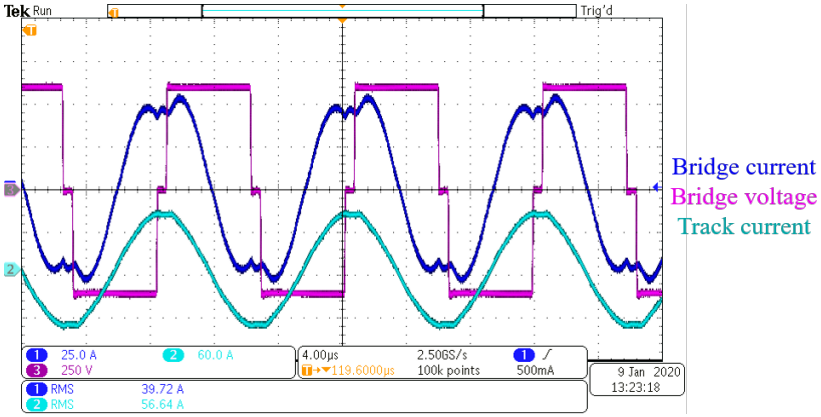

Fig. 5.21: Scope waveforms showing inverter output current, output voltage and track current through the primary pad.

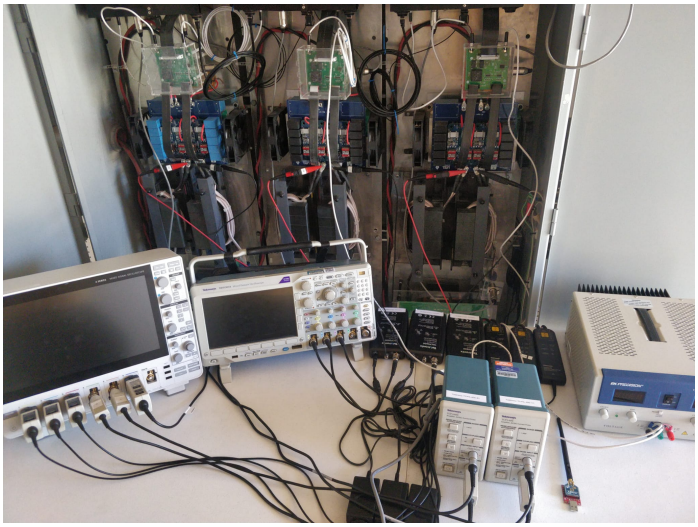

Fig. 5.22: View of the test setup inside the shed.

circuit voltage tests. The receiver pad is disconnected from the secondary compensation network and the open circuit voltage induced on the receiver pads is measured across the leads coming from the receiver pads. The profile is measured by energizing the primary pad with a low track current and driving the vehicle over the pads in a straight path. The simulated and measured V_{oc} profiles with one transmitter pad energized are shown in Fig. 5.23b and Fig. 5.23a respectively. Similarly, the simulated and measured Voc profiles with two transmitter pads energized are shown in Fig. 5.24b and Fig. 5.24a respectively. It should be noted that the magnitude of the voltage changes with coupling factor (or mutual

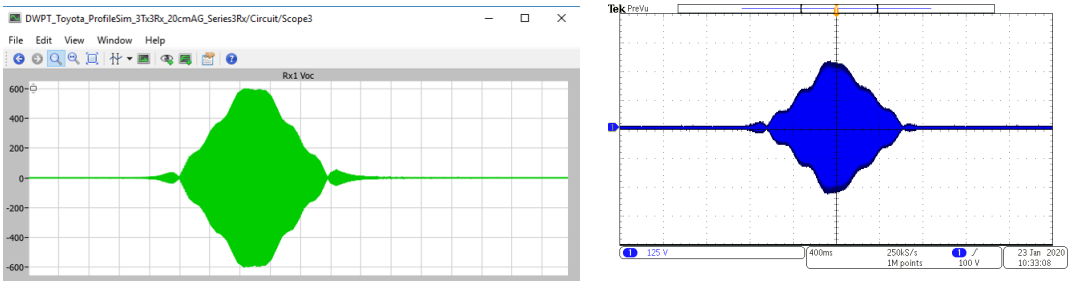

(a) (b)

Fig. 5.23: Single primary pad energized: a) Simulated V_{oc} profile b) Measured V_{oc} profile.

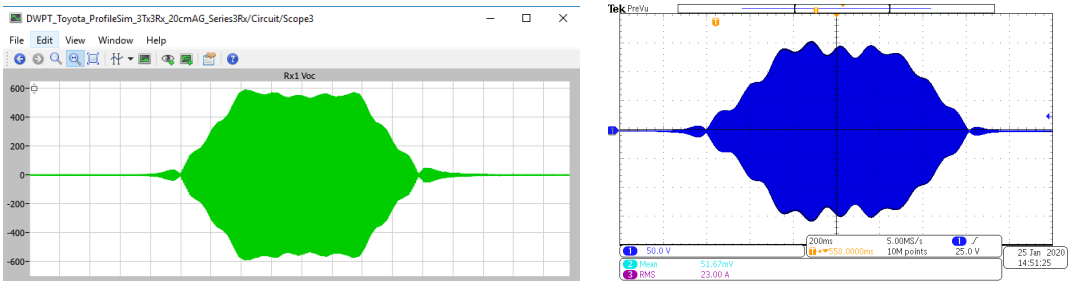

(a) (b)

Fig. 5.24: Two primary pads: a) Simulated V_{oc} profile b) Measured V_{oc} profile.

inductance). This test verifies the shape of the dynamic open circuit voltage profile and validates the simulation model. The simulations in Fig. 5.23a and Fig. 5.24a assume a vehicle speed of 60 mph and the corresponding time scale shown is 0.2 s per division on the x-axis. The x-axis shows the time from 0 to 3.565 33 s. Simulation time can be improved by setting the vehicle speed to be higher. The hardware V_{oc} results are obtained using a primary pad track current of 25 A, which is lower than the nominal track current of 56 A. This dynamic profile retains its shape and scales proportionally when the track current is varied.

5.7.3 Electric and Magnetic Field Safety

The leakage magnetic (B) and electric (E) fields are measured at three different locations in and around the RAV4 EV while the wireless charging system is operational. A Narda EHP-200 probe is used to measure the fields. The measurement locations are shown in Fig. 5.25. The measured field values are shown in Table 5.6.

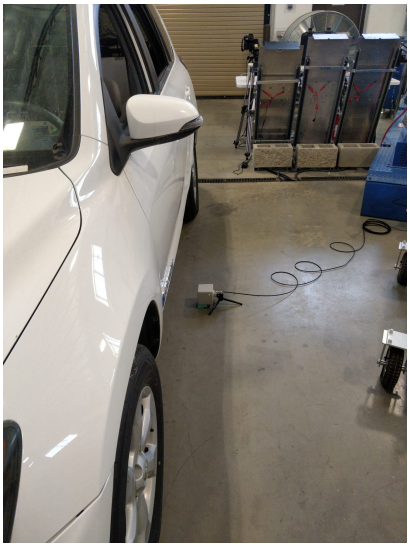

(a)

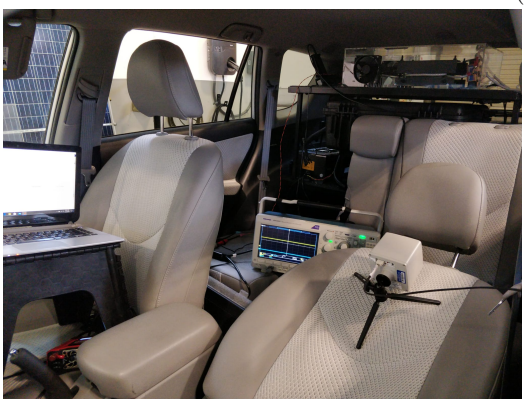

(b)

(c)

Fig. 5.25: Field probe in a) position 1 outside the RAV4 EV b) position 2 on the driver seat inside the RAV4 EV c) position 3 beside the receiver power electronics inside the RAV4 EV.

Table 5.6: Measured Leakage Field Values

Position	Location	Field	Measurement
1	Outside the car	B	5.91 µT
1	Outside the car	E	66.93 V/m
2	Driver seat	B	0.16 µT
2	Driver seat	E	0.48 V/m
3	Next to the receiver power electronics	B	7.09 µT
3	Next to the receiver power electronics	E	152.25 V/m

5.7.4 Power Transfer Tests

Once the system track current and open circuit voltage profiles are verified, the system is functional and ready for power transfer tests. The system is energized at lower voltages and tested to observe power transfer. Once the waveforms are as expected, the system is energized to its full input voltage and tested. Two results from the power transfer tests are shown in Fig. 5.26 and Fig. 5.27. In Fig. 5.26, a DC input voltage of 500 V is supplied to the primary inverter. The DC input current is measured at 67.33 A with an inverter output current of 89.65 A when the receiver is present on the track. The receiver side waveforms indicate 75 A of DC current going into an auxiliary battery on the electric vehicle at a battery voltage of 365 V. In Fig. 5.27, the bridge voltage, bridge current and track current measured on the primary side when the system operates with an input DC voltage of 550 V. A peak DC current of 78 A at a battery voltage of 373 V is observed at the secondary side rectifier output. This corresponds to a power transfer of 29 kW and the DC-DC efficiency is found to be 88%.

The DWPT system is tested at varying speeds to validate the system response, detection, and automated turn-on of the individual primary pads. Two different speeds of 7 mph and 22 mph are considered. The higher speed limit is set by the vehicle safety limitations on the test track and the weather conditions. The system operates without active power regulation in these tests and hence the profiles are expected to stay the same even at highway speeds of 60 mph to 80 mph. The dynamic profiles of battery current seen in Fig. 5.28 closely resemble the simulated battery current shown in Fig. 5.11. The human error involved in aligning the vehicle perfectly with the primary pads results in slight variations in

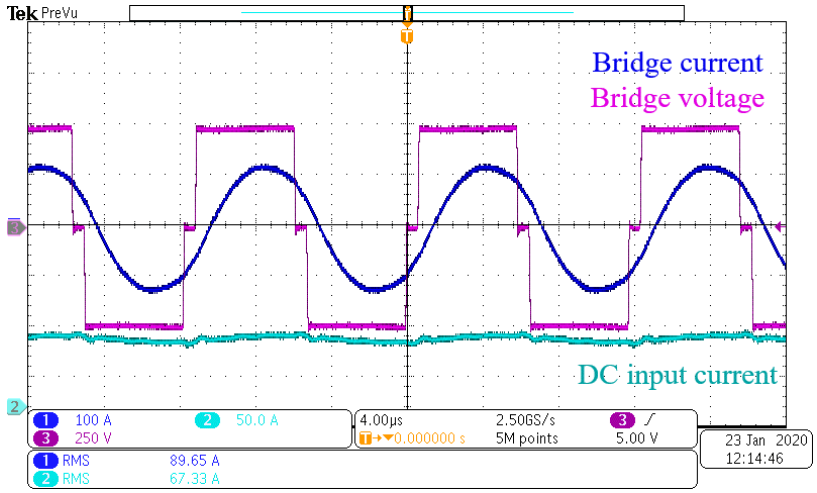

Fig. 5.26: Scope waveforms showing inverter output current, output voltage and input DC current.

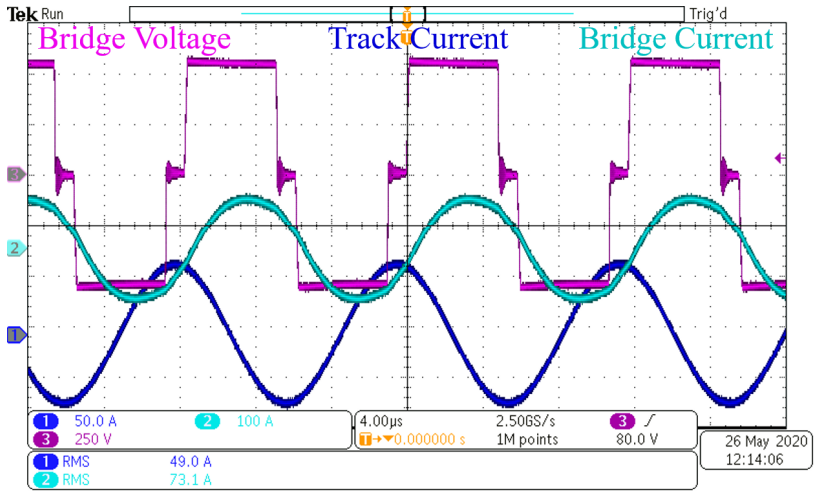

Fig. 5.27: Primary side waveforms showing inverter (bridge) output voltage and current along with the track current.

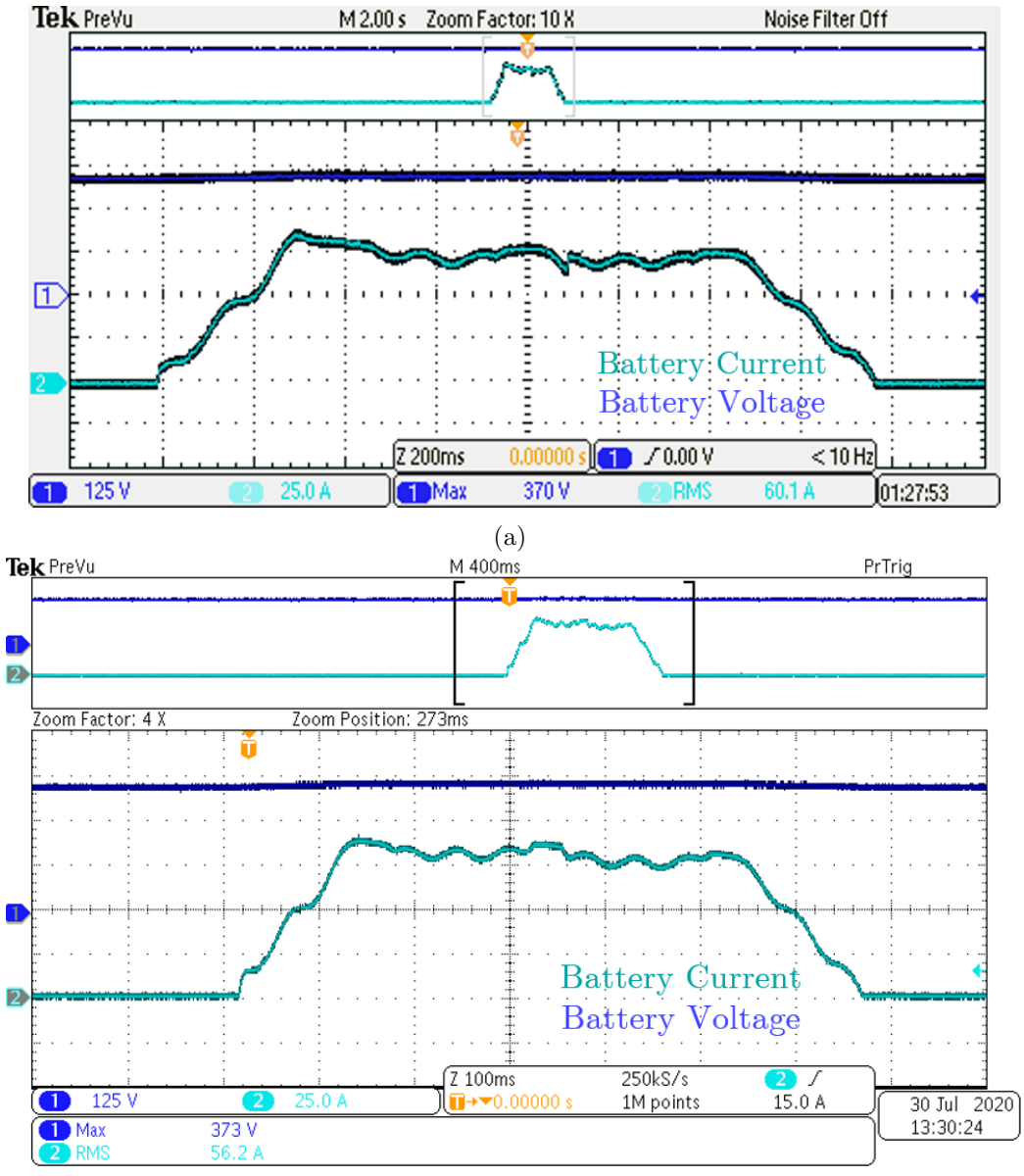

Fig. 5.28: Secondary side measured battery current and battery voltage showing a) 29.6 kW delivered to the battery at 7 mph vehicle speed b) 29.8 kW delivered to the battery at 22 mph vehicle speed.

the coupling profile and actual power transfer. It can be observed that even without active power regulation, a relatively smooth profile of power transfer can be obtained during dynamic wireless power transfer by adjusting the coil overlap and the turn-on and turn-off of adjacent primary pads.

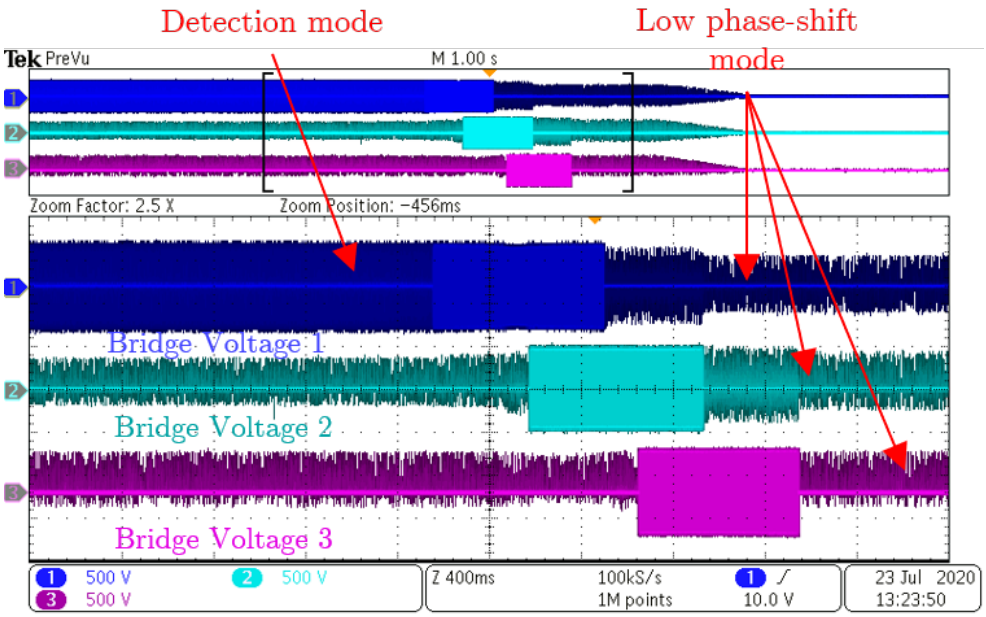

Fig. 5.29: Scope waveforms showing inverter output voltage for all three primary pads.

At 7 mph, the primary side waveforms showing the three bridge (inverter output) voltages are shown in Fig. 5.29. A detection mode can be seen on Bridge Voltage 1 waveform. This mode energizes the first primary pad at a low track current (>10 A) to enable vehicle detection. As the receiver pad comes within the acceptable coupling range, a change in DC input current is detected and the first primary pad ramps up to its nominal value of track current. The pad turn-on and turn-off transitions are achieved using just the DC current and inverter output current sensors. Communication between the primary pad controllers is limited to a fiber optic link carrying a synchronization signal to ensure that the three pads operate in phase.

The three different track current waveforms and the total input DC current to the

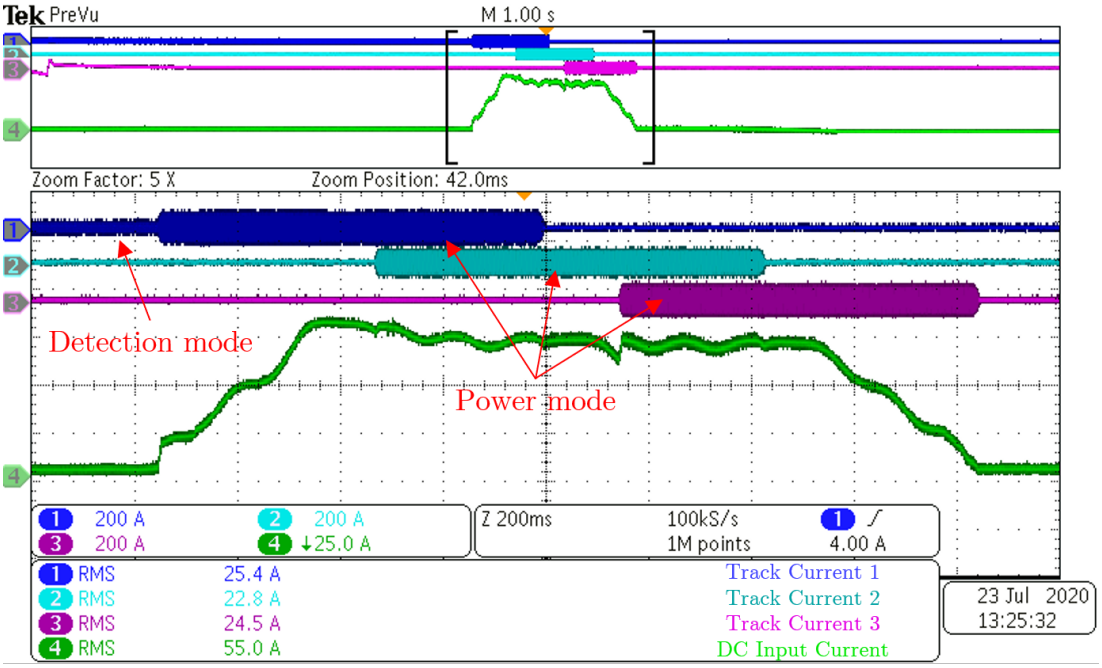

Fig. 5.30: Scope waveforms showing primary pad currents and total input DC current at 7 mph and a peak power transfer of 29.6 kW to the vehicle battery.

system can be seen in Fig. 5.30. The low track current in detection mode is clearly visible in this figure. Further, the DC input current profile also resembles the battery input DC current profile on the secondary side as shown in Fig. 5.28a.

The primary side waveforms from the 22 mph dynamic power test with all three pads are shown in Fig. 5.31. The figure shows the three inverter output voltages and the three individual DC input currents. The sum of all the three input DC currents results in a profile similar to the one in Fig. 5.30. The presence of an approaching vehicle is detected using an RFID antenna and the first primary pad is set to its detection mode. Once in the detection mode, the system automatically ramps up the power transfer to the secondary when the minimum coupling threshold is exceeded.

The three primary track currents can be seen in Fig. 5.32. The change in track current from the low phase-shift mode to the detection mode and the change in track current from detection mode to power mode is also seen in the figure.

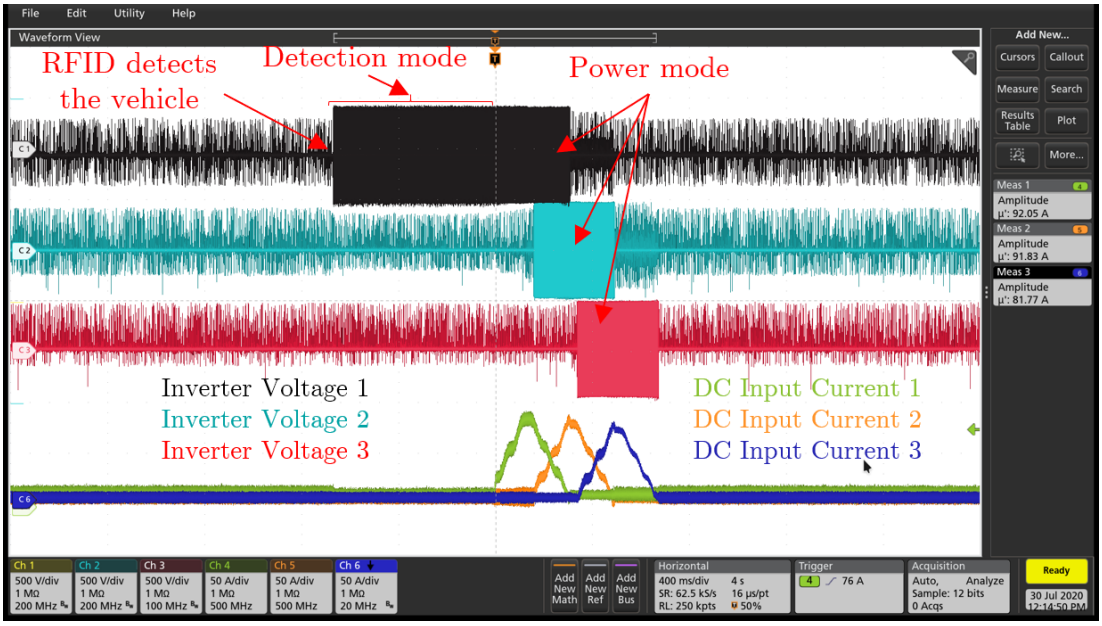

Fig. 5.31: Scope waveforms showing inverter output voltages and input DC currents for all three primary pads at 22 mph vehicle speed and a peak power transfer of 29.8 kW to the vehicle battery.

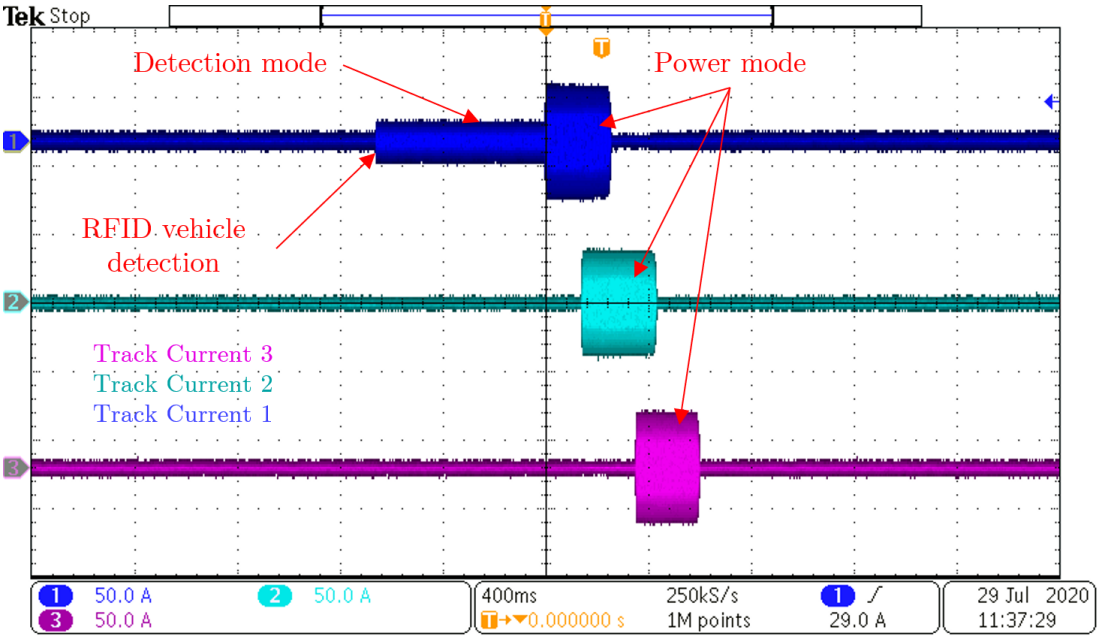

Fig. 5.32: Scope waveforms showing the three primary track currents at 22 mph vehicle speed using automated system turn-on.

5.7.5 Summary

This chapter presents the design of a 30 kW three-pad receiver system for dynamic wireless power transfer applications. Three Z3 receivers rated to 11.1 kVA are used to receive 30 kW of power from an electrified roadway, demonstrating the scalability of the system. Despite the standard Z3 pads being sub-optimal for dynamic wireless charging, this work develops a usable DWPT system with multiple Z3 standard pads.

In the current work, an electric SUV is used as the test vehicle to emulate a larger vehicle using multi-pad receivers. In reality, for an SUV or a sedan sized vehicle, an optimal receiver system would only use have one receiver pad due to the space constraints under the vehicle. And larger vehicles like semi-trucks and buses would have two or more pads in their receiver system.

CHAPTER 6

SAFETY AND COMPLIANCE FOR DWPT SYSTEMS

6.1 Introduction

Most electronic devices generate electro-magnetic (EM) fields which can interfere with the operation of other electronic devices. When these EM fields are sufficiently high, they can affect human health and well-being as well as interfere with other devices. Therefore, it is imperative to understand the sources of these fields and the effects they have on human beings and other electronic devices. Few of the major standards organizations regulating the amount of acceptable EM emissions are

- Federal Communications Commission (FCC)
- International Commission on Non-ionizing Radiation Protection (ICNIRP)
- International Electrotechnical Commission (IEC)
- Comité International Spécial des Perturbations Radioélectriques (CISPR)
- International Standards Organization (ISO) and
- Society of Automotive Engineers (SAE)

Due to a lack of standards specific to dynamic wireless power transfer, DWPT systems typically follow the safety and compliance guidelines set for stationary wireless charging.

6.2 ICNIRP Limits

From a safety standpoint, the ICNIRP standard is widely accepted as the benchmark for compliance. The ICNIRP standard specifies a limit of 27.5 µT for 85 kHz wireless charging. This is the maximum magnetic flux density limit for a wireless charging product that is accessible by the general public. Occupational limits tend to be higher, but are not

Table 6.1: Table showing the CISPR 11 limits for wireless power transfer [2].

Frequency range (kHz)	Limits for a measuring distance D in meters					
	Magnetic field quasi-peak (dBµA/m)					
	≤1 kW		1 kW - 7.7 kW		≥7.7 kW	
	D = 10 m	D = 3 m	D = 10 m	D = 3 m	D = 10 m	D = 3 m
19-25	57	81.5	72	96.5	87	111.5
25-36	22.6-21	47.1-45.5	22.6-21	47.1-45.5	22.6-21	47.1-45.5
36-40	56.2	80.7	71.2	95.7	86.2	110.7
40-55	20.6-19.3	45.1-43.8	20.6-19.3	45.1-43.8	20.6-19.3	45.1-43.8
55-65	54.4	78.9	69.4	93.9	84.4	108.9
65-79	18.5-17.7	43-42.2	18.5-17.7	43-42.2	18.5-17.7	43-42.2
79-90	52.8	77.3	67.8	92.3	82.8	107.3
90-130	17.2-15.6	41.7-40.1	17.2-15.6	41.7-40.1	17.2-15.6	41.7-40.1

considered as a target specification when designing consumer goods. Some manufacturers also target the lower 15 µT limit to ensure safe operation even in the vicinity of pacemakers.

With stationary wireless chargers, it is likely to have pedestrians in close proximity to the radiated magnetic field. Hence, it is essential to minimize the leakage magnetic field and comply with the ICNIRP standards. However, with dynamic wireless charging, pedestrians or human beings are not expected to be in close proximity to the wireless charging system. In such cases, it is still essential to meet the product performance and EMC standards such as the CISPR standards.

6.3 CISPR Limits

The CISPR limits are aimed at electro-magnetic compliance (EMC) and preventing interference with other electronic devices rather than a health and safety perspective. The CISPR 11 standard specifies the EM emission limits for WPT systems. According to the CISPR 11 standard, the radiation produced by wireless chargers is considered intentional radiation for the purpose of transferring electro-magnetic energy. Further, WPT systems have a relatively strong EM field in their fundamental frequency of power transfer due to the the sinusoidal coil currents. This makes it easy to relax the standards in specific frequency ranges that are dedicated for use in wireless charging technologies.

The CISPR 11 standard specifies the magnetic field quasi-peak limits for radiated emissions generated by wireless power transfer systems. A quasi-peak measurement is a

Table 6.2: CISPR 11 limits for harmonic band emissions for 85 kHz WPT in Japan [3].

Radiated emission limits of fundamental wave	Radiated emission limits in other bands	
79 - 90 kHz	9 - 150 kHz	150 kHz - 30 MHz
68.4 dBμA/m at 10 m (quasi-peak)	23.1 dBμA/m at 10 m (quasi-peak), except 79-90 kHz	39 dBμA/m at 0.15 MHz to 3 dBμA/m at 30 MHz
		Exceptions: for 158 - 180 kHz, 237 - 270 kHz, 316 - 360 kHz, and 395 - 450 kHz emission limits are higher than above by 10 dB

weighted measurement based on how often the peak value is repeated. The higher the rate of peak value repetition, higher the quasi-peak value. Table. 6.1 shows the radiated emission limits for various fundamental frequency bands at different measuring distances of D = 3 m and D = 10 m. It can be observed that the commonly used WPT frequency bands in the multiples of 20 kHz have more relaxed limits on the radiated emissions compared to the other frequency bands in the table. Table. 6.2 show the limits on the fundamental and higher order harmonics for 85 kHz EV wireless power transfer adopted by Japan in 2016 [3]. The highest power level currently considered is 7.7 kW.

6.4 Booster Pad Example

The Booster Coil DWPT pad developed in [23] is considered as an example DWPT system and methods to reduce the leakage magnetic field are evaluated. An image of the Booster Coil pads is shown in Fig. 6.1. The Booster Coil pad is designed to have additional turns at the ends of a segmented rectangular pad to help increase the ampere-turns available and *boost* the power transfer during the transition from one pad to another. These additional turns also contribute to the leakage magnetic field generated by the DWPT system. This work presents the different ways of reducing leakage fields using both passive and active shielding methods in DWPT systems and a simulation analysis is performed to evaluate an active shielding method. Compliance limits specified by the CISPR 11 standard are

considered as the target magnetic field levels in this work.

Fig. 6.1: Image of Booster Coil pads in the outdoor trench.

To measure the leakage magnetic field of the system and to evaluate different shielding methods, a 30 kW DWPT system is modeled. The FEM models to evaluate coil parameters and leakage fields are developed using ANSYS Maxwell and the circuit models to evaluate power transfer and tuning networks are developed using LTSpice.

6.4.1 ANSYS Model

The Booster Coil pad is modeled in ANSYS as shown in Fig. 6.2. A 4.7 m $\times$ 1.8 m steel plate is considered as the metal chassis of the vehicle. The system is designed with three primary Booster Coil pads and one secondary pad on the vehicle.

The adaptive mesh generated is as shown in Fig. 6.3. Two 20 m long test lines (1 and 3) are used on either side of the system, 10 m away from the center of the primary pad. The second test line is setup between the primary and secondary pads, where the highest magnetic field is expected. The leakage magnetic field is measured on the test lines to satisfy CISPR 11 limits in the 79 - 90 kHz range of frequencies.

Prior works in [110] explore the concept of modeling leakage magnetic fields and compare simulation and hardware results. The results show a good match between hardware and simulation results. Three different boundary conditions are considered in [110]. These

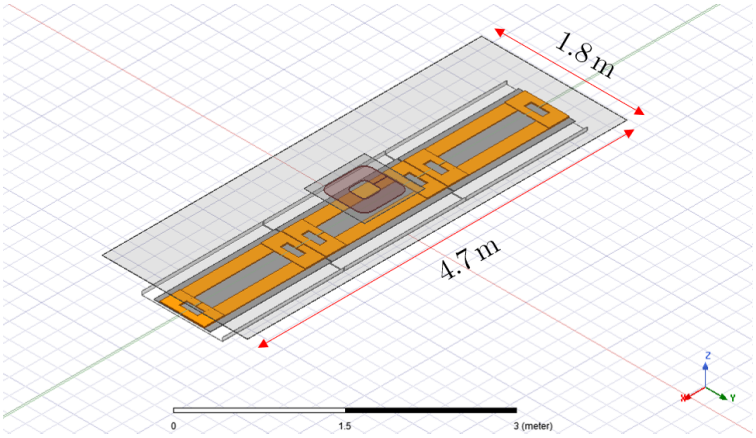

Fig. 6.2: Image of Booster Coil pads modeled in ANSYS.

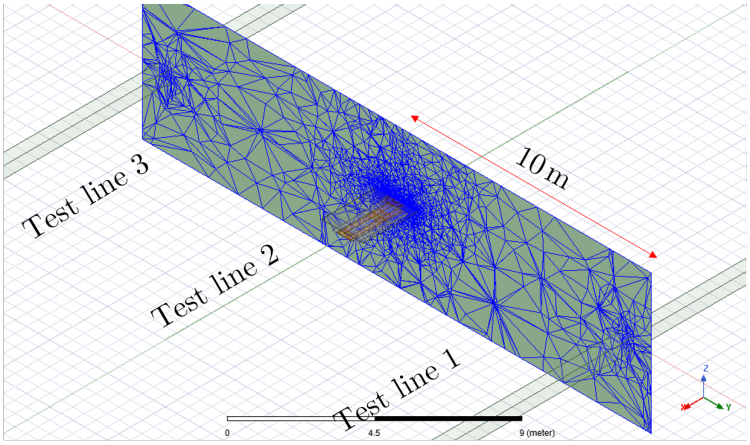

Fig. 6.3: Adaptive meshing across a test plane showing the mesh shape.

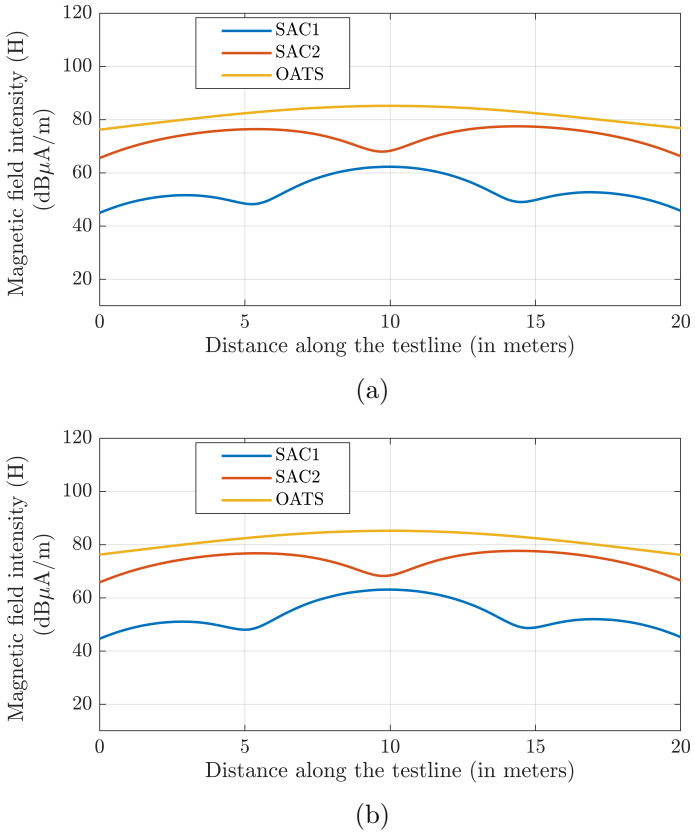

Fig. 6.4: Plots showing leakage magnetic field along a) test lines 1 and b) test line 3.

are as follows:

- Open-air test site (OATS)
- Semi-anechoic chamber 1 (SAC1)
- Semi-anechoic chamber 2 (SAC2)

The designed Booster Coil model is tested using the three different boundary conditions and the results are presented in Fig. 6.4 and Fig. 6.5.

6.4.2 LTSpice Model

An LTSpice simulation is developed to obtain accurate amplitude and phase information of the current excitations of the primary and secondary coils. This information is then used in the ANSYS simulation to obtain accurate field data. The LTSpice simulation is

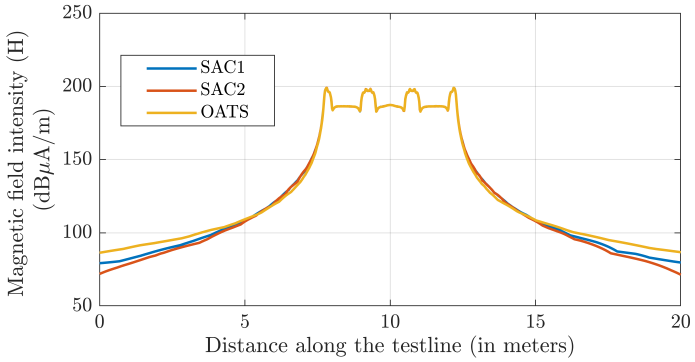

Fig. 6.5: Plot showing leakage magnetic field along the test line 2

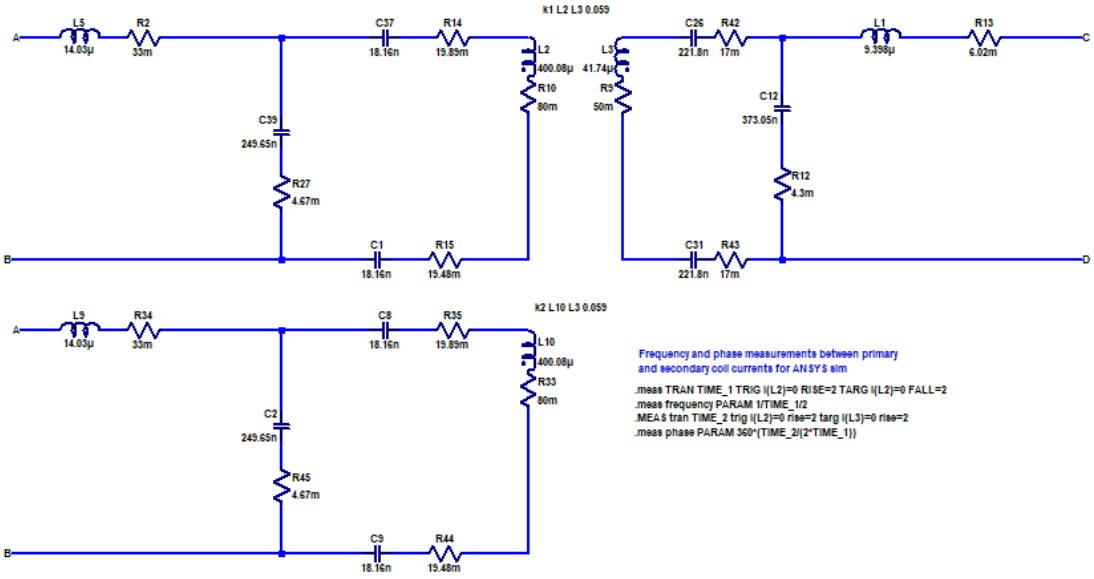

Fig. 6.6: LTSpice simulation used to obtain the amplitude and phase of the current excitations.

shown in Fig. 6.6. The LTSpice model shows two primary pads and one secondary pad to model the system behavior at the transition zone between two primary pads. The coupling and self-inductance data is obtained from the FEM model simulated in ANSYS Maxwell.

6.5 Methods to Reduce Leakage Magnetic Field

Various shielding methods can be used to reduce leakage magnetic field in WPT systems. Shielding of leakage fields can be achieved by providing a lower reluctance path for

magnetic flux or by generating opposing fields to cancel the field generated by the WPT system. Depending on whether external excitation is used or not, shielding methods can be classified as passive or active shielding.

6.5.1 Passive Shielding

Passive shielding methods do not require external excitation and can be implemented in the following ways

- Metal shielding
- Ferrite shielding
- Shorted loop of wire

The passive shielding methods have a significant impact in low power systems, but their effectiveness is limited when there is a large air-gap between the primary and secondary pads. In the present example, an active shielding method is considered due to the high power level.

6.5.2 Active Shielding

Active shielding refers to those methods which require external excitation to generate opposing magnetic fields to counter the leakage magnetic field. Active shielding in WPT systems can be achieved by adding cancellation coils adjacent to the primary or secondary coils to create opposing fields [111].

The cancellation coils used to reduce the EM fields generated by the main coils in the system also generate their own EM fields. This is also an important aspect to consider while developing an active EM field cancellation system.

6.5.3 Simulation Results

To evaluate the effectiveness of active shielding with cancellation coils, the booster coil system resonant network is tuned to achieve 30 kW of power transfer while the shielding

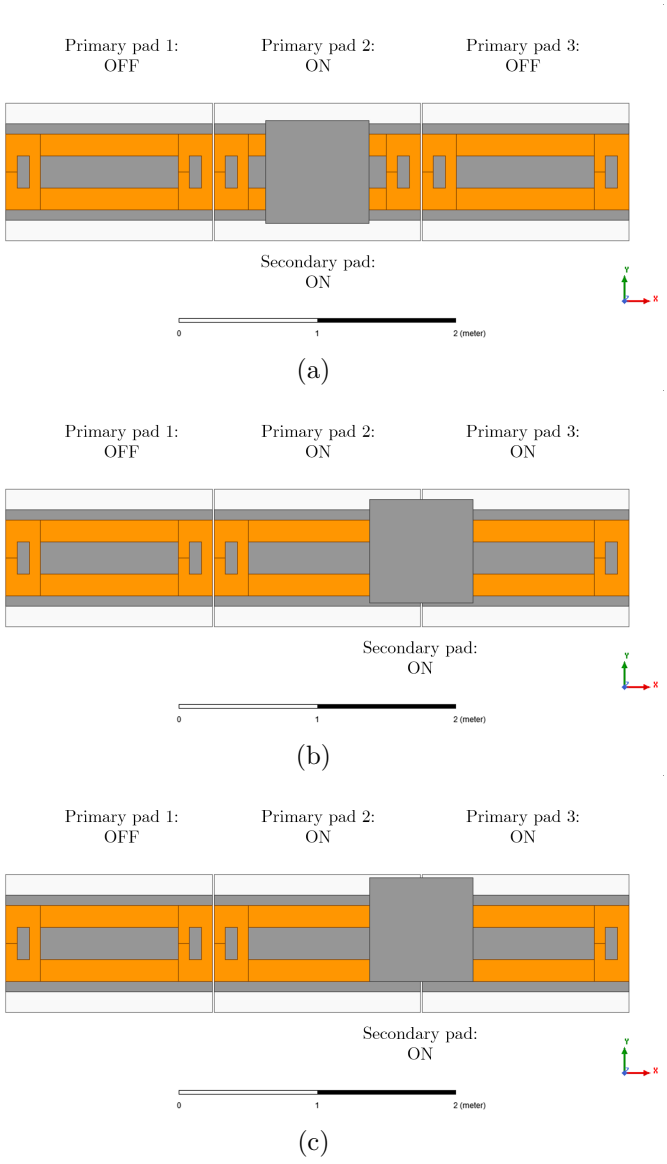

Fig. 6.7: ANSYS model with the receiver in a) position 1 b) position 2 and c) position 3.

methods are varied. The worst case position for leakage field is chosen as the baseline simulation. Three different positions of the secondary pad are evaluated to measure the leakage field and identify the worst case leakage field. The three positions are shown in Fig. 6.7. Providing adequate shielding in the worst case scenario ensures compliance with the CISPR 11 limits in the other scenarios as well.

The magnetic fields in each of the three secondary pad positions are plotted in Fig. 6.8. The lower limit of the scale in Fig. 6.10 corresponds to the CISPR 11 limit of 82.8 dBµA/m.

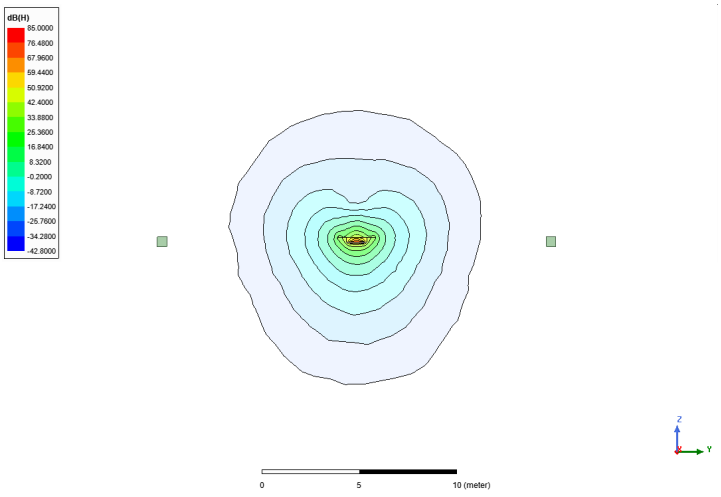

(a)

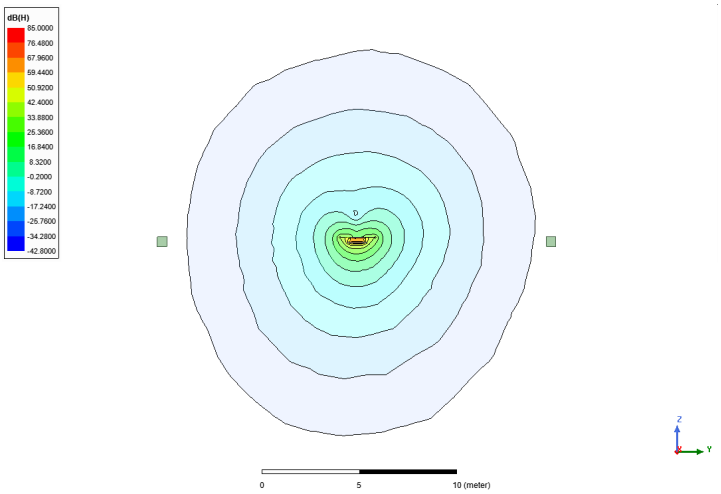

(b)

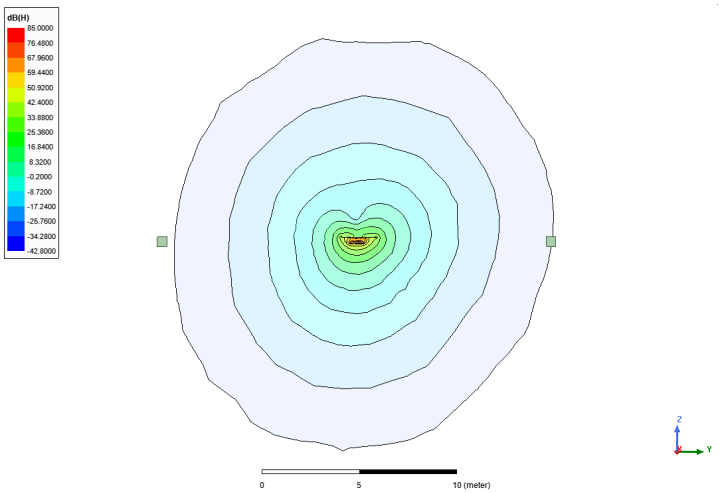

(c)

Fig. 6.8: Leakage field comparison on test plane with receiver pad in a) position 1 b) position 2 and c) position 3.

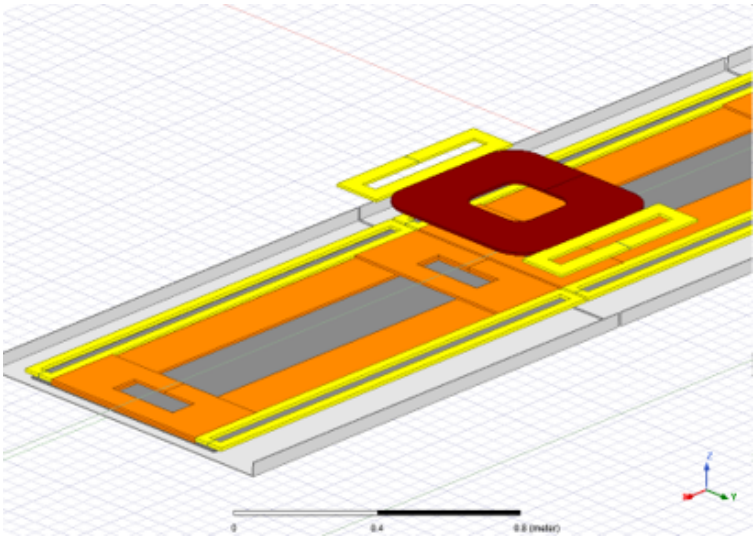

Fig. 6.9: Active cancellation for primary and secondary pads.

This corresponds to a value of $-42.8\,\mathrm{dB\mu A/m}$ on the ANSYS field plots. For convenience, the outermost contour of the field plots is set to this limit value. The white regions on the contour plot represent the regions where the CISPR 11 limits are satisfied. The green boxes represent the meshing zone used to improve resolution of the results along test line 1 and test line 3.

The 100 mm misaligned condition when the secondary pad is located in between the two primary pads (transition zone) is observed to have higher leakage magnetic fields compared to other positions as seen in Fig. 6.8c. It is observed that the magnetic field exceeds the limit on test line 1. This scenario is considered the baseline case with no EM field cancellation methods. The three cases considered for comparison are as follows:

- No cancellation coils, 100 mm misalignment and transition zone (baseline case)
- Active cancellation coils, baseline case and phase-shift control of the full bridge inverter
- Active cancellation coils, baseline case and DC-DC control of the full bridge inverter

Active shielding of magnetic fields in the system is achieved by using additional cancellation coils on either side of the primary and secondary coils. An image of the active

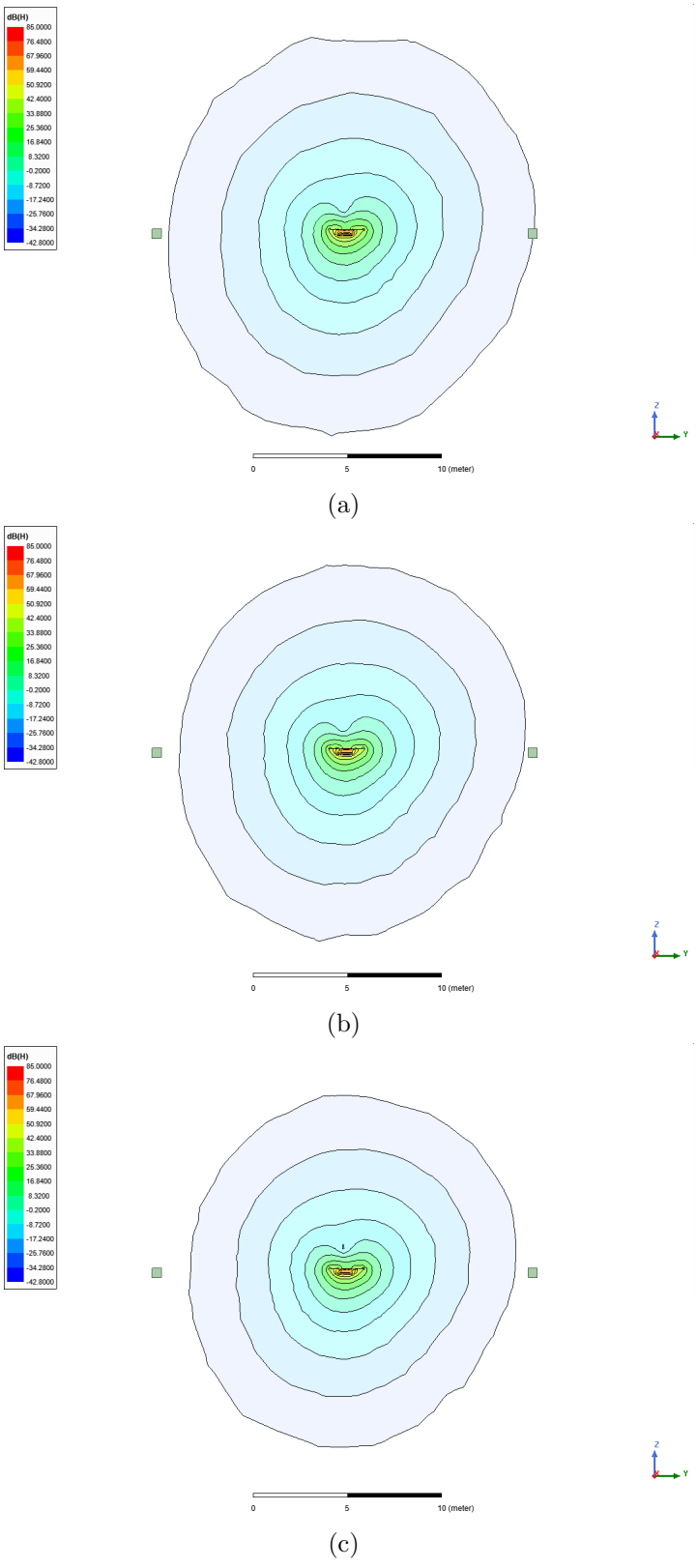

(a)

(b)

(c)

Fig. 6.10: Leakage field comparison on test plane with a) no cancellation b) active cancellation and phase-shift control c) active cancellation and DC-DC control.

Table 6.3: Summary of how system attributes are affected by shielding methods.

Parameter	Baseline simulation (no cancellation)	Active cancellation (Phase shift control)	Active cancellation (DC-DC control)
Primary inductance (μH)	402.39	405	405
Secondary inductance (μH)	41.71	46	46
Coupling coefficient (at the transition zone)	0.048	0.067	0.067
Primary current (ampere-turns)	711	560	470
Secondary current (ampere-turns)	455	455	455
Primary booster current (ampere-turns)	427	336	282
Primary cancellation current (ampere-turns)	NA	50	50
Secondary cancellation current (ampere-turns)	NA	100	100
DC link voltage (V)	600	600	420
Phase shift angle (°)	170	110	170

cancellation coils (yellow) can be seen in Fig. 6.9. With the addition of these extra coils, there is a change in system coupling coefficient and self-inductance, this results in a higher power transfer level than required. Hence the power level needs to be regulated for a fair comparison. In practice, this can be achieved either by phase-shift control of the inverter or adjusting the input DC link voltage using a front-end DC/DC converter. The system parameters with each of the three cases are presented in Table 6.3. The magnetic field contour plots of the simulation analysis are shown in Fig. 6.10.

6.5.4 Summary

This chapter discusses the compliance requirements for WPT systems based on the CISPR 11 standard and a method of active cancellation is presented to reduce the leakage magnetic fields generated by a booster coil pad.

CHAPTER 7

CONCLUSIONS AND FUTURE WORK

7.1 Conclusions

This dissertation presents details on the different practical aspects of implementing dynamic wireless power transfer systems. The design of a 50 kW concrete-embedded transmitter pad is presented and multiple prototypes are constructed and tested. 56 kW of power transfer is demonstrated over a coil-to-coil air-gap of 203.2 mm at 93% DC-DC efficiency. This allows for additional pavement surfacing with materials such as asphalt. Pavement-embedded transmitter pads involve additional thermal and structural challenges. Several design modifications and considerations are presented in this dissertation. Test results from the thermal and structural tests are also included for reference. The tests indicate that the DWPT hardware is still functional after several loading cycles emulating heavy-duty vehicular traffic. The design effort also focused on simplifying the pad design, thereby reducing construction complexity. The proposed pad design procedure also supports the use of existing construction methods and materials.

To improve the utilization of DWPT hardware and make it economically viable, different vehicle classes must be able to receive adequate power from the same transmitter hardware. The proposed solution to tackle this problem is the use of multi-pad receivers. The design of a scaled-down 30 kW multi-pad receiver system is presented. A three-pad receiver is mounted to the chassis of an electric SUV and interfaced with a battery pack inside the vehicle. Three transmitter pads in a roadway test bed are used to transfer power to the three-pad receiver. The receiver is designed from three Z3 standard circular pads specified in the SAE J2954 standard, each rated to 11 kVA. Series and parallel connections for multi-pad receivers are evaluated and a series connected three-pad receiver is designed to operate at 30 kW. Hardware design and experimental results show dynamic wireless power

transfer at vehicle speeds upto 22 mph.

A method of digital twin modeling for the wireless charging pads is also presented in this dissertation. Detailed modeling workflow including the development of FEM pad models and circuit simulation models in PLECS and LTSpice are presented. The modeling method provides a platform for further research on evaluating the controls and system dynamics for future DWPT work.

7.2 Future Work

Future research in the field of in-motion charging of EVs is required in the areas of scalable manufacturing of pavement-DWPT systems, vehicle-to-vehicle (V2V), vehicle-to-infrastructure (V2I) and vehicle-to-grid (V2G) communication protocols and better standardization of both static and dynamic wireless charging technologies for EVs. The development of the test bed at Utah State University and testing of roadway embedded power electronics is expected to provide more insight into future research requirements.

Another aspect of DWPT technologies essential for real world deployment is the communication and synchronization between adjacent transmitter pads and corresponding electronics. While this is currently achieved using fiber optic cable, a shift to wireless synchronization between the transmitter pads can help achieve greater modularity in the charging infrastructure.

REFERENCES

[1] T. Gardner, "Wireless power transfer roadway integration," Master's thesis, Utah State University, Logan, UT, 2017.

[2] International Telecommunication Union, "Wireless power transmission using technologies other than radio frequency beam." [Online]. Available: https://www.itu.int/pub/R-REP-SM.2303-2-2017

[3] K. Ishida, "Global status on wpt standardization and regulation," Mar 2017.

[4] "U.s. energy information administration - eia - independent statistics and analysis." [Online]. Available: https://www.eia.gov/energyexplained/use-of-energy/transportation.php

[5] "Fast facts on transportation greenhouse gas emissions," Jul 2020. [Online]. Available: www.epa.gov/greenvehicles/fast-facts-transportation-greenhouse-gas-emissions

[6] M. Holland, "Tesla model 3 on supercharger v3 - adds 50% range in under 12 minutes! (charts!)," Sep 2019. [Online]. Available: https://cleantechnica.com/2019/06/24/tesla-model-3-on-supercharger-v3-adds-50-range-in-under-12-minutes-charts/

[7] F. Todeschini, S. Onori, and G. Rizzoni, "An experimentally validated capacity degradation model for li-ion batteries in phevs applications," *IFAC Proceedings Volumes*, vol. 45, no. 20, pp. 456–461, 2012, 8th IFAC Symposium on Fault Detection, Supervision and Safety of Technical Processes. [Online]. Available: https://www.sciencedirect.com/science/article/pii/S1474667016347966

[8] J. M. Miller, O. C. Onar, C. White, S. Campbell, C. Coomer, L. Seiber, R. Sepe, and A. Steyerl, "Demonstrating dynamic wireless charging of an electric vehicle: The benefit of electrochemical capacitor smoothing," *IEEE Power Electronics Magazine*, vol. 1, no. 1, pp. 12–24, 2014.

[9] S. Y. Choi, B. W. Gu, S. Y. Jeong, and C. T. Rim, "Advances in wireless power transfer systems for roadway-powered electric vehicles," *IEEE Journal of Emerging and Selected Topics in Power Electronics*, vol. 3, no. 1, pp. 18–36, 2015.

[10] V. Cirimele, R. Torchio, A. Virgillito, F. Freschi, and P. Alotto, "Challenges in the electromagnetic modeling of road embedded wireless power transfer," *Energies*, vol. 12, no. 14, p. 2677, Jul 2019. [Online]. Available: http://dx.doi.org/10.3390/en12142677

[11] P. Machura, V. De Santis, and Q. Li, "Driving range of electric vehicles charged by wireless power transfer," *IEEE Transactions on Vehicular Technology*, vol. 69, no. 6, pp. 5968–5982, 2020.

[12] S. C. Anenberg, J. Miller, D. K. Henze, R. Minjares, and P. Achakulwisut, "The global burden of transportation tailpipe emissions on air pollution-related mortality in 2010 and 2015," *Environmental Research Letters*, vol. 14, no. 9, p. 094012, sep 2019. [Online]. Available: https://doi.org/10.1088/1748-9326/ab35fc

[13] "Climate policy priorities for the new administration and congress," Feb 2021. [Online]. Available: www.c2es.org/document/climate-policy-priorities-for-the-new-administration-and-congress/

[14] "Progress and potential for electric vehicles to reduce carbon emissions." [Online]. Available: www.rff.org/publications/reports/potential-role-and-impact-evs-us-decarbonization-strategies/

[15] "All-electric vehicles." [Online]. Available: https://www.fueleconomy.gov/feg/evtech.shtml

[16] S. Phillippi, "Building the business case for fleet electrification." [Online]. Available: https://www.greenbiz.com/article/curves-road-fleet-electrification-sponsored

[17] Electrification Coalition. (2012) The electric drive bellwether? [Online]. Available: www.electrificationcoalition.org/the-electric-drive-bellwether/

[18] ——. (2012) Economic impact of the electrification roadmap. [Online]. Available: www.electrificationcoalition.org/economic-impact-of-the-electrification-roadmap/

[19] "Go anywhere." [Online]. Available: https://www.tesla.com/trips

[20] "Enabling extreme fast charging: A technology gap assessment." [Online]. Available: https://www.energy.gov/eere/vehicles/downloads/enabling-extreme-fast-charging-technology-gap-assessment

[21] D. Yelaverthi, "Three-phase unfolding based soft dc-link converter topologies for ac to dc applications," Ph.D. dissertation, Utah State University, Logan, UT, 2021.

[22] H. Tu, H. Feng, S. Srdic, and S. Lukic, "Extreme fast charging of electric vehicles: A technology overview," *IEEE Transactions on Transportation Electrification*, vol. 5, no. 4, pp. 861–878, 2019.

[23] R. M. Nimri, A. Kamineni, and R. Zane, "A modular pad design compatible with sae j2954 for dynamic inductive power transfer," in *2020 IEEE PELS Workshop on Emerging Technologies: Wireless Power Transfer (WoW)*, 2020, pp. 45–49.

[24] B. J. Varghese, A. Kamineni, N. Roberts, M. Halling, D. J. Thrimawithana, and R. A. Zane, "Design considerations for 50 kw dynamic wireless charging with concrete-embedded coils," in *2020 IEEE PELS Workshop on Emerging Technologies: Wireless Power Transfer (WoW)*, 2020, pp. 40–44.

[25] B. J. Varghese, R. A. Zane, A. Kamineni, R. Tavakoli, Z. Pantic, C. Chou, and L. Liu, "Multi-pad receivers for high power dynamic wireless power transfer," in *2020 IEEE Energy Conversion Congress and Exposition (ECCE)*, 2020, pp. 5162–5168.

[26] "Porsche charging options for on the road." [Online]. Available: https://www.porsche.com/international/aboutporsche/e-performance/charging-on-the-road/

[27] "Supercharger." [Online]. Available: https://www.tesla.com/supercharger

[28] R. Tavakoli, "Design of road embedded dynamic charging systems for electrified transportation," Ph.D. dissertation, Utah State University, Logan, UT, 2020.

[29] Z. Zhang, H. Pang, C. H. T. Lee, X. Xu, X. Wei, and J. Wang, "Comparative analysis and optimization of dynamic charging coils for roadway-powered electric vehicles," *IEEE Transactions on Magnetics*, vol. 53, no. 11, pp. 1–6, 2017.

[30] G. Rituraj, B. K. Kushwaha, and P. Kumar, "A unipolar coil arrangement method for improving the coupling coefficient without ferrite material in wireless power transfer systems," *IEEE Transactions on Transportation Electrification*, vol. 6, no. 2, pp. 497–509, 2020.

[31] C. Wang, C. Zhu, G. Wei, J. Feng, J. Jiang, and R. Lu, "Design of compact three-phase receiver for meander-type dynamic wireless power transfer system," *IEEE Transactions on Power Electronics*, vol. 35, no. 7, pp. 6854–6866, 2020.

[32] T. Fujita, T. Yasuda, and H. Akagi, "A dynamic wireless power transfer system applicable to a stationary system," *IEEE Transactions on Industry Applications*, vol. 53, no. 4, pp. 3748–3757, 2017.

[33] Z. Wang, S. Cui, S. Han, K. Song, C. Zhu, M. I. Matveevich, and O. S. Yurievich, "A novel magnetic coupling mechanism for dynamic wireless charging system for electric vehicles," *IEEE Transactions on Vehicular Technology*, vol. 67, no. 1, pp. 124–133, 2018.

[34] Y. Liu, R. Mai, D. Liu, Y. Li, and Z. He, "Efficiency optimization for wireless dynamic charging system with overlapped dd coil arrays," *IEEE Transactions on Power Electronics*, vol. 33, no. 4, pp. 2832–2846, 2018.

[35] S. Cui, Z. Wang, S. Han, C. Zhu, and C. C. Chan, "Analysis and design of multiphase receiver with reduction of output fluctuation for ev dynamic wireless charging system," *IEEE Transactions on Power Electronics*, vol. 34, no. 5, pp. 4112–4124, 2019.

[36] F. Lu, H. Zhang, H. Hofmann, and C. C. Mi, "A dynamic charging system with reduced output power pulsation for electric vehicles," *IEEE Transactions on Industrial Electronics*, vol. 63, no. 10, pp. 6580–6590, 2016.

[37] L. Chen, G. R. Nagendra, J. T. Boys, and G. A. Covic, "Double-coupled systems for ipt roadway applications," *IEEE Journal of Emerging and Selected Topics in Power Electronics*, vol. 3, no. 1, pp. 37–49, 2015.

[38] Z. Chen, W. Jing, X. Huang, L. Tan, C. Chen, and W. Wang, "A promoted design for primary coil in roadway-powered system," *IEEE Transactions on Magnetics*, vol. 51, no. 11, pp. 1–4, 2015.

[39] G. R. Nagendra, G. A. Covic, and J. T. Boys, "Sizing of inductive power pads for dynamic charging of evs on ipt highways," *IEEE Transactions on Transportation Electrification*, vol. 3, no. 2, pp. 405–417, 2017.

[40] H. Hao, G. A. Covic, and J. T. Boys, "An approximate dynamic model of lcl- t-based inductive power transfer power supplies," *IEEE Transactions on Power Electronics*, vol. 29, no. 10, pp. 5554–5567, 2014.

[41] W. Chen, F. Lin, G. A. Covic, and J. T. Boys, "Design considerations of a bipolar track for dynamic electric vehicle charging," in *2019 IEEE Energy Conversion Congress and Exposition (ECCE)*, 2019, pp. 1188–1194.

[42] S. Y. Jeong, J. H. Park, G. P. Hong, and C. T. Rim, "Autotuning control system by variation of self-inductance for dynamic wireless ev charging with small air gap," *IEEE Transactions on Power Electronics*, vol. 34, no. 6, pp. 5165–5174, 2019.

[43] A. Ong, P. K. S. Jayathuathnage, J. H. Cheong, and W. L. Goh, "Transmitter pulsation control for dynamic wireless power transfer systems," *IEEE Transactions on Transportation Electrification*, vol. 3, no. 2, pp. 418–426, 2017.

[44] V. B. Vu, M. Dahidah, V. Pickert, and V. T. Phan, "A high-power multiphase wireless dynamic charging system with low output power pulsation for electric vehicles," *IEEE Journal of Emerging and Selected Topics in Power Electronics*, vol. 8, no. 4, pp. 3592–3608, 2020.

[45] D. Kobayashi, T. Imura, and Y. Hori, "Real-time coupling coefficient estimation and maximum efficiency control on dynamic wireless power transfer for electric vehicles," in *2015 IEEE PELS Workshop on Emerging Technologies: Wireless Power (2015 WoW)*, 2015, pp. 1–6.

[46] H. Feng, T. Cai, S. Duan, J. Zhao, X. Zhang, and C. Chen, "An lcc-compensated resonant converter optimized for robust reaction to large coupling variation in dynamic wireless power transfer," *IEEE Transactions on Industrial Electronics*, vol. 63, no. 10, pp. 6591–6601, 2016.

[47] C. T. Rim and C. Mi, *Wireless power transfer for electric vehicles and mobile devices*. Wiley Blackwell, 2017.

[48] K. Hata, T. Imura, and Y. Hori, "Dynamic wireless power transfer system for electric vehicles to simplify ground facilities - power control and efficiency maximization on the secondary side," in *2016 IEEE Applied Power Electronics Conference and Exposition (APEC)*, 2016, pp. 1731–1736.

[49] A. Zakerian, S. Vaez-Zadeh, and A. Babaki, "A dynamic wpt system with high efficiency and high power factor for electric vehicles," *IEEE Transactions on Power Electronics*, vol. 35, no. 7, pp. 6732–6740, 2020.

[50] A. Kamineni, M. J. Neath, G. A. Covic, and J. T. Boys, "A mistuning-tolerant and controllable power supply for roadway wireless power systems," *IEEE Transactions on Power Electronics*, vol. 32, no. 9, pp. 6689–6699, 2017.

[51] H. Feng, T. Cai, S. Duan, J. Zhao, X. Zhang, and C. Chen, "An lcc-compensated resonant converter optimized for robust reaction to large coupling variation in dynamic wireless power transfer," *IEEE Transactions on Industrial Electronics*, vol. 63, no. 10, pp. 6591–6601, 2016.

[52] Z. Yan, L. Wu, and W. Baoyun, "High-efficiency coupling-insensitive wireless power and information transmission based on the phase-shifted control," *IEEE Transactions on Power Electronics*, vol. 33, no. 9, pp. 7821–7831, 2018.

[53] X. Ge, Y. Sun, Z. Wang, and C. Tang, "Dual-independent-output inverter for dynamic wireless power transfer system," *IEEE Access*, vol. 7, pp. 107 320–107 333, 2019.

[54] B. J. Varghese, A. Kamineni, and R. A. Zane, "Investigation of a dd2q pad structure for high power inductive power transfer," in *2019 IEEE PELS Workshop on Emerging Technologies: Wireless Power Transfer (WoW)*, 2019, pp. 129–133.

[55] J. Jiang, Z. Li, K. Song, B. Song, S. Dong, and C. Zhu, "A cascaded topology and control method for two-phase receivers of dynamic wireless power transfer systems," *IEEE Access*, vol. 8, pp. 47 445–47 455, 2020.

[56] A. C. Bagchi, "Emerging works on wireless inductive power transfer: Auv charging from constant current distribution and analysis of controls in ev dynamic charging," Ph.D. dissertation, Utah State University, Logan, UT, 2020.

[57] T. Saha, A. C. Bagchi, and R. A. Zane, "Analysis and design of an lcl–t resonant dc–dc converter for underwater power supply," *IEEE Transactions on Power Electronics*, vol. 36, no. 6, pp. 6725–6737, 2021.

[58] T. Koyama, T. Honjo, M. Ishihara, K. Umetani, and E. Hiraki, "Simple self-driven synchronous rectifier for resonant inductive coupling wireless power transfer," in *2017 IEEE International Telecommunications Energy Conference (INTELEC)*, 2017, pp. 363–368.

[59] J. Luo, W. Xiao, G. Zhang, D. Qiu, B. Zhang, F. Xie, and Y. Chen, "Novel cuk-based bridgeless rectifier of wpt system with wide power modulation range and low current ripple," *IEEE Transactions on Industrial Electronics*, pp. 1–1, 2021.

[60] W. Chen, C. Liu, C. Lee, and Z. Shan, "Cost-effectiveness comparison of coupler designs of wireless power transfer for electric vehicle dynamic charging," *Energies*, vol. 9, no. 11, p. 906, 2016.

[61] G. Y. Dayanikli, R. R. Hatch, R. M. Gerdes, H. Wang, and R. Zane, "Electromagnetic sensor and actuator attacks on power converters for electric vehicles," in *2020 IEEE Security and Privacy Workshops (SPW)*, 2020, pp. 98–103.

[62] R. Tavakoli, A. Echols, U. Pratik, Z. Pantic, F. Pozo, A. Malakooti, and M. Maguire, "Magnetizable concrete composite materials for road-embedded wireless power transfer pads," in *2017 IEEE Energy Conversion Congress and Exposition (ECCE)*, 2017, pp. 4041–4048.

[63] "Magment dynamic wireless charging." [Online]. Available: https://www.magment.de/en-dynamic-wireless-charging

[64] K. Throngnumchai, A. Hanamura, Y. Naruse, and K. Takeda, "Design and evaluation of a wireless power transfer system with road embedded transmitter coils for dynamic charging of electric vehicles," in *2013 World Electric Vehicle Symposium and Exhibition (EVS27)*, 2013, pp. 1–10.

[65] A. Marghani, D. Wilson, and T. Larkin, "Performance of inductive power transfer-based pavements of electrified roads," in *2019 IEEE PELS Workshop on Emerging Technologies: Wireless Power Transfer (WoW)*, 2019, pp. 196–201.

[66] S. Kim, M. Amirpour, G. Covic, and S. Bickerton, "Thermal characterisation of a double-d pad," in *2019 IEEE PELS Workshop on Emerging Technologies: Wireless Power Transfer (WoW)*, 2019, pp. 1–5.

[67] S. Lee, M. Kim, B. Lee, and J. Lee, "Impact of rebar and concrete on power dissipation of wireless power transfer systems," *IEEE Transactions on Industrial Electronics*, vol. 67, no. 1, pp. 276–287, 2020.

[68] G. A. Covic, "Inductive power transfer," *Proceedings of the IEEE*, vol. 101, no. 6, pp. 1–14, 2013.

[69] B. J. Varghese, A. Kamineni, and R. A. Zane, "Empirical closed-form analysis for inductance and coupling coefficient calculation for ferrite-based matched inductive charging systems," in *2019 IEEE Energy Conversion Congress and Exposition (ECCE)*, 2019, pp. 1210–1214.

[70] H. Li, J. Fang, and Y. Tang, "Reduced-order dynamical models of tuned wireless power transfer systems," in *2018 International Power Electronics Conference (IPEC-Niigata 2018 -ECCE Asia)*, 2018, pp. 337–341.

[71] H. Li, J. Fang, and Y. Tang, "A simplified dynamical model for tuned wireless power transfer systems," 2019.

[72] R. Tavakoli and Z. Pantic, "Analysis, design, and demonstration of a 25-kw dynamic wireless charging system for roadway electric vehicles," *IEEE Journal of Emerging and Selected Topics in Power Electronics*, vol. 6, no. 3, pp. 1378–1393, 2018.

[73] R. Tavakoli, A. Jovicic, N. Chandrappa, R. Bohm, and Z. Pantic, "Design of a dual-loop controller for in-motion wireless charging of an electric bus," in *2016 IEEE Energy Conversion Congress and Exposition (ECCE)*, 2016, pp. 1–8.

[74] C. M. Apostoaia and M. Cernat, "A dynamic inductive power transfer system," in *2019 8th International Conference on Renewable Energy Research and Applications (ICRERA)*, 2019, pp. 839–844.

[75] V. P. Galigekere, R. Zeng, J. Pries, O. Onar, and G.-J. Su, "Direct envelope modeling of load-resonant inverter for wireless power transfer applications," 3 2020. [Online]. Available: https://www.osti.gov/biblio/1649407

[76] E. Ayisire, A. El-Shahat, and A. Sharaf, "Magnetic resonance coupling modelling for electric vehicles wireless charging," in *2018 IEEE Global Humanitarian Technology Conference (GHTC)*, 2018, pp. 1–2.

[77] C. Cui, K. Song, C. Zhu, Q. Zhang, Y. Liu, and S. Dong, "State feedback controller design of dynamic wireless power transfer system," in *2018 IEEE PELS Workshop on Emerging Technologies: Wireless Power Transfer (Wow)*, 2018, pp. 1–5.

[78] Electrification Coalition. (2020) Saving money with electric vehicle leasing. [Online]. Available: www.electrificationcoalition.org/saving-money-with-ev-leasing/

[79] ——. (2020) Municipal fleet electrification: A case study of charlotte, nc. [Online]. Available: www.electrificationcoalition.org/charlotte-case-study/

[80] ——. (2020) Municipal fleet electrification: A case study of austin, tx. [Online]. Available: www.electrificationcoalition.org/austin-case-study/

[81] M. S. Sheng, A. V. Sreenivasan, G. A. Covic, D. Wilson, and B. Sharp, "Inductive power transfer charging infrastructure for electric vehicles: A new zealand case study," in *2019 IEEE PELS Workshop on Emerging Technologies: Wireless Power Transfer (WoW)*, 2019, pp. 53–58.

[82] C. Yang, W. Lou, J. Yao, and S. Xie, "On charging scheduling optimization for a wirelessly charged electric bus system," *IEEE Transactions on Intelligent Transportation Systems*, vol. 19, no. 6, pp. 1814–1826, 2018.

[83] J. M. Miller, P. T. Jones, J. M. Li, and O. C. Onar, "Ornl experience and challenges facing dynamic wireless power charging of ev's," *IEEE Circuits and Systems Magazine*, vol. 15, no. 2, pp. 40–53, 2015.

[84] D. Kosmanos, L. A. Maglaras, M. Mavrovouniotis, S. Moschoyiannis, A. Argyriou, A. Maglaras, and H. Janicke, "Route optimization of electric vehicles based on dynamic wireless charging," *IEEE Access*, vol. 6, pp. 42 551–42 565, 2018.

[85] A. A. S. Mohamed, C. R. Lashway, and O. Mohammed, "Modeling and feasibility analysis of quasi-dynamic wpt system for ev applications," *IEEE Transactions on Transportation Electrification*, vol. 3, no. 2, pp. 343–353, 2017.

[86] E. Sproul, D. A. Trinko, Z. D. Asher, B. Limb, T. H. Bradley, J. C. Quinn, and R. Zane, "Electrification of class 8 trucking: Economic analysis of in-motion wireless power transfer compared to long-range batteries," in *2018 IEEE Transportation Electrification Conference and Expo (ITEC)*, 2018, pp. 744–748.

[87] B. J. Limb, Z. D. Asher, T. H. Bradley, E. Sproul, D. A. Trinko, B. Crabb, R. Zane, and J. C. Quinn, "Economic viability and environmental impact of in-motion wireless power transfer," *IEEE Transactions on Transportation Electrification*, vol. 5, no. 1, pp. 135–146, 2019.

[88] W. H. Hayt and J. A. Buck, *Engineering electromagnetics*. McGraw-Hill Education, 2019.

[89] G. A. Covic and J. T. Boys, "Modern trends in inductive power transfer for transportation applications," *IEEE Journal of Emerging and Selected Topics in Power Electronics*, vol. 1, no. 1, p. 28–41, 2013.

[90] S. Li, W. Li, J. Deng, T. D. Nguyen, and C. C. Mi, "A double-sided lcc compensation network and its tuning method for wireless power transfer," *IEEE Transactions on Vehicular Technology*, vol. 64, no. 6, pp. 2261–2273, 2015.

[91] W. Zhang and C. C. Mi, "Compensation topologies of high-power wireless power transfer systems," *IEEE Transactions on Vehicular Technology*, vol. 65, no. 6, pp. 4768–4778, 2016.

[92] A. N. Barnes, "Thermal modeling and analysis of roadway embedded wireless power transfer modules," Master's thesis, Utah State University, Logan, UT, 2020.

[93] N. Raine, "Long term feasibility of inductive power transfer systems in concrete," Master's thesis, Utah State University, Logan, UT, 2021.

[94] A. Foote, O. C. Onar, S. Debnath, J. Pries, V. P. Galigekere, and B. Ozpineci, "System design of dynamic wireless power transfer for automated highways," in *2019 IEEE Transportation Electrification Conference and Expo (ITEC)*, 2019, pp. 1–5.

[95] C. C. Mi, G. Buja, S. Y. Choi, and C. T. Rim, "Modern advances in wireless power transfer systems for roadway powered electric vehicles," *IEEE Transactions on Industrial Electronics*, vol. 63, no. 10, pp. 6533–6545, 2016.

[96] C. Snyder, "The effects of charge/discharge rate on capacity fade of lithium ion batteries," Ph.D. dissertation, Rensselaer Polytechnic Institute, Jan 2016.

[97] J. Bochmann, M. Curbach, and F. Jesse, "Influence of artificial discontinuities in concrete under compression load-a literature review," *Structural Concrete*, vol. 19, no. 2, p. 559–567, Aug 2017.

[98] E. Rojas, P. Barr, and M. Halling, "Bridge response due to temperature variations," *U.S. Department of Transportation*, 2014.

[99] B. J. Varghese, J. Mermigas, A. Kamineni, and R. A. Zane, "Inductive wireless charging pad for electric vehicles reinforced with non-conductive elements," Patent 20 210 078 425, March, 2021.

[100] R. Sabbah, R. Kizilel, J. Selman, and S. Al-Hallaj, "Active (air-cooled) vs. passive (phase change material) thermal management of high power lithium-ion packs: Limitation of temperature rise and uniformity of temperature distribution," *Journal of Power Sources*, vol. 182, no. 2, p. 630–638, 2008.

[101] N. A. Roberts, J. Mullen, R. A. Zane, A. Kamineni, B. J. Varghese, and M. Halling, "Static heat exchanger for wireless power transfer pad," Patent 20 210 082 613, March, 2021.

[102] "Dynamometer drive schedules," Mar 2021. [Online]. Available: https://www.epa.gov/vehicle-and-fuel-emissions-testing/dynamometer-drive-schedules

[103] Z. Lin, J.-M. Li, and J. Dong, "Dynamic wireless power transfer: Potential impact on plug-in electric vehicle adoption," in *SAE Technical Paper*. SAE International, 04 2014. [Online]. Available: https://doi.org/10.4271/2014-01-1965

[104] E. Suomalainen and F. Colet, "A corridor-based approach to estimating the costs of electric vehicle charging infrastructure on highways," *World Electric Vehicle Journal*, vol. 10, 2019.

[105] Y. Jang, S. Jeong, and M. Lee, "Initial energy logistics cost analysis for stationary, quasi-dynamic, and dynamic wireless charging public transportation systems," *Energies*, vol. 9, no. 7, p. 483, Jun 2016. [Online]. Available: http://dx.doi.org/10.3390/en9070483

[106] A. Gil and J. Taiber, "A literature review in dynamic wireless power transfer for electric vehicles: Technology and infrastructure integration challenges," in *Sustainable Automotive Technologies 2013*, J. Wellnitz, A. Subic, and R. Trufin, Eds. Cham: Springer International Publishing, 2014, pp. 289–298.

[107] A. Foote, O. C. Onar, S. Debnath, M. Chinthavali, B. Ozpineci, and D. E. Smith, "Optimal sizing of a dynamic wireless power transfer system for highway applications," in *2018 IEEE Transportation Electrification Conference and Expo (ITEC)*, June 2018, pp. 1–6.

[108] "Energy consumption of full electric vehicles." [Online]. Available: https://ev-database.org/cheatsheet/energy-consumption-electric-car

[109] "SAE J2954: Wireless power transfer for light-duty plug-in/electric vehicles and alignment methodology," *SAE International*.

[110] G. Ombach, L. Percebon, and S. Mathar, "Magnetic leakage field study of a 7 kw wireless electric vehicle charging system," Jun 2016. [Online]. Available: https://www.mdpi.com/2032-6653/8/2/501

[111] B. J. Varghese, A. Kamineni, and R. A. Zane, "Wireless power transfer with active field cancellation using multiple magnetic flux sinks," Patent 20 210 082 617, March, 2021.

[112] D. Patil, J. M. Miller, B. Fahimi, P. T. Balsara, and V. Galigekere, "A coil detection system for dynamic wireless charging of electric vehicle," *IEEE Transactions on Transportation Electrification*, vol. 5, no. 4, pp. 988–1003, 2019.

[113] H. Feng, R. Tavakoli, O. C. Onar, and Z. Pantic, "Advances in high-power wireless charging systems: Overview and design considerations," *IEEE Transactions on Transportation Electrification*, vol. 6, no. 3, pp. 886–919, 2020.

[114] S. Ruddell, U. K. Madawala, and D. J. Thrimawithana, "A wireless ev charging topology with integrated energy storage," *IEEE Transactions on Power Electronics*, vol. 35, no. 9, pp. 8965–8972, 2020.

[115] G. Buja, C. Rim, and C. C. Mi, "Dynamic charging of electric vehicles by wireless power transfer," *IEEE Transactions on Industrial Electronics*, vol. 63, no. 10, pp. 6530–6532, 2016.

[116] O. C. Onar, "Guest editorial special issue on wireless charging systems," *IEEE Transactions on Transportation Electrification*, vol. 3, no. 2, pp. 301–302, 2017.

[117] V. Cirimele, M. Diana, F. Freschi, and M. Mitolo, "Inductive power transfer for automotive applications: State-of-the-art and future trends," *IEEE Transactions on Industry Applications*, vol. 54, no. 5, pp. 4069–4079, 2018.

[118] M. Maemura and A. Wendt, "Dynamic power transfer as a feature - employing stationary wpt devices for dynamic operation," in *2020 IEEE PELS Workshop on Emerging Technologies: Wireless Power Transfer (WoW)*, 2020, pp. 50–55.

[119] A. Zaheer, M. Neath, H. Z. Z. Beh, and G. A. Covic, "A dynamic ev charging system for slow moving traffic applications," *IEEE Transactions on Transportation Electrification*, vol. 3, no. 2, pp. 354–369, 2017.

[120] K. Sasaki and T. Imura, "Combination of sensorless energized section switching system and double-lcc for dwpt," in *2020 IEEE PELS Workshop on Emerging Technologies: Wireless Power Transfer (WoW)*, 2020, pp. 62–67.

[121] A. Kamineni, M. J. Neath, A. Zaheer, G. A. Covic, and J. T. Boys, "Interoperable ev detection for dynamic wireless charging with existing hardware and free resonance," *IEEE Transactions on Transportation Electrification*, vol. 3, no. 2, pp. 370–379, 2017.

[122] Y. Huang, C. Liu, Y. Zhou, Y. Xiao, and S. Liu, "Power allocation for dynamic dual-pickup wireless charging system of electric vehicle," *IEEE Transactions on Magnetics*, vol. 55, no. 7, pp. 1–6, 2019.

[123] A. Babaki, S. Vaez-Zadeh, and A. Zakerian, "Performance optimization of dynamic wireless ev charger under varying driving conditions without resonant information," *IEEE Transactions on Vehicular Technology*, vol. 68, no. 11, pp. 10 429–10 438, 2019.

[124] D. Kim, S. Kim, S. Kim, J. Moon, I. Cho, and D. Ahn, "Coupling extraction and maximum efficiency tracking for multiple concurrent transmitters in dynamic wireless charging," *IEEE Transactions on Power Electronics*, vol. 35, no. 8, pp. 7853–7862, 2020.

[125] C. Wang, C. Zhu, K. Song, G. Wei, S. Dong, and R. G. Lu, "Primary-side control method in two-transmitter inductive wireless power transfer systems for dynamic wireless charging applications," in *2017 IEEE PELS Workshop on Emerging Technologies: Wireless Power Transfer (WoW)*, 2017, pp. 1–6.

[126] H. Jafari, M. Mahmoudi, T. O. Olowu, and A. Sarwat, "Multi-level power controller design for dynamic wireless electric vehicle charging systems," in *2020 IEEE Transportation Electrification Conference Expo (ITEC)*, 2020, pp. 986–991.

[127] Y. Dai, L. Ma, M. Huang, and H. Su, "Modeling and analysis methods for the dwpt system applicated in evs charging," in *2018 IEEE PELS Workshop on Emerging Technologies: Wireless Power Transfer (Wow)*, 2018, pp. 1–6.

[128] J. Jiang, K. Song, Z. Li, C. Zhu, and Q. Zhang, "System modeling and switching control strategy of wireless power transfer system," *IEEE Journal of Emerging and Selected Topics in Power Electronics*, vol. 6, no. 3, pp. 1295–1305, 2018.

[129] G. de Freitas Lima and R. B. Godoy, "Modeling and prototype of a dynamic wireless charging system using lsps compensation topology," *IEEE Transactions on Industry Applications*, vol. 55, no. 1, pp. 786–793, 2019.

[130] S. A. Moosavi, S. S. Mortazavi, A. Namadmalan, A. Iqbal, and M. Al-Hitmi, "Design and sensitivity analysis of dynamic wireless chargers for efficient energy transfer," *IEEE Access*, vol. 9, pp. 16 286–16 295, 2021.

[131] Y. Guo, L. Wang, Q. Zhu, C. Liao, and F. Li, "Switch-on modeling and analysis of dynamic wireless charging system used for electric vehicles," *IEEE Transactions on Industrial Electronics*, vol. 63, no. 10, pp. 6568–6579, 2016.

[132] A. K. Swain, S. Devarakonda, and U. K. Madawala, "Modeling, sensitivity analysis, and controller synthesis of multipickup bidirectional inductive power transfer systems," *IEEE Transactions on Industrial Informatics*, vol. 10, no. 2, pp. 1372–1380, 2014.

[133] T. Tan, K. Chen, Y. Jiang, Z. Zhao, and L. Yuan, "Dynamic modeling and analysis of multi-receiver wireless power transfer system," in *2019 IEEE PELS Workshop on Emerging Technologies: Wireless Power Transfer (WoW)*, 2019, pp. 391–395.

[134] N. Teerakawanich, "Dynamic modeling of wireless power transfer systems with a moving coil receiver," in *2018 IEEE Transportation Electrification Conference and Expo, Asia-Pacific (ITEC Asia-Pacific)*, 2018, pp. 1–5.

[135] "A critical review on wireless charging for electric vehicles," *Renewable and Sustainable Energy Reviews*, vol. 104, pp. 209–234, 2019.

[136] A. Dayerizadeh, H. Feng, and S. M. Lukic, "Dynamic wireless charging: Reflexive field containment using saturable inductors," *IEEE Transactions on Industry Applications*, vol. 56, no. 2, pp. 1784–1792, 2020.

[137] M. Budhia, G. A. Covic, and J. T. Boys, "Design and optimization of circular magnetic structures for lumped inductive power transfer systems," *IEEE Transactions on Power Electronics*, vol. 26, no. 11, p. 3096–3108, 2011.

[138] M. Budhia, J. T. Boys, G. A. Covic, and C.-Y. Huang, "Development of a single-sided flux magnetic coupler for electric vehicle ipt charging systems," *IEEE Transactions on Industrial Electronics*, vol. 60, no. 1, p. 318–328, 2013.

[139] F. Y. Lin, C. Carretero, G. A. Covic, and J. T. Boys, "A reduced order model to determine the coupling factor between magnetic pads used in wireless power transfer," *IEEE Transactions on Transportation Electrification*, vol. 3, no. 2, p. 321–331, 2017.

CURRICULUM VITAE

Benny J. Varghese

Journal Articles

- A Smart Autonomous WPT System for Electric Wheelchair Applications With Free-Positioning Charging Feature, A. Azad, R. Tavakoli, U. Pratik, B. J. Varghese, C. Coopmans and Z. Pantic, *IEEE Journal of Emerging and Selected Topics in Power Electronics*, vol. 8, no. 4, pp. 3516-3532, Dec. 2020

- Optimum Design of Decoupled Concentric Coils for Operation in Double-Receiver Wireless Power Transfer Systems, U. Pratik, B. J. Varghese, A. Azad and Z. Pantic, *IEEE Journal of Emerging and Selected Topics in Power Electronics*, vol. 7, no. 3, pp. 1982-1998, Sept. 2019

Patents

- Inductive wireless charging pad for electric vehicles reinforced with non-conductive elements, B. J. Varghese, J. Mermigas, A. Kamineni, and R. A. Zane, September 2020, *patent pending.*

- Static heat exchanger for wireless power transfer pad, N. A. Roberts, J. Mullen, R. A. Zane, A. Kamineni, B. J. Varghese, and M. Halling, September 2020, *patent pending.*

- Wireless power transfer with active field cancellation using multiple magnetic flux sinks, B. J. Varghese, A. Kamineni, and R. A. Zane, September 2020, *patent pending.*

Conference Papers

- Experimental and Usability Evaluation of Wireless Power Devices Based on the Air-Fuel Alliance Magnetic Resonance Standard, B. J. Varghese, K. Sealy, S. Gupta, and Z. Pantic, *2021 IEEE Applied Power Electronics Conference and Exposition (APEC)*, Phoenix, AZ, USA, 2021, *accepted*

- Design Considerations for 50 kW Dynamic Wireless Charging with Concrete-Embedded Coils, B. J. Varghese, A. Kamineni, N. Roberts, M. Halling, D. J. Thrimawithana and R. A. Zane, *2020 IEEE PELS Workshop on Emerging Technologies: Wireless Power Transfer (WoW)*, Seoul, Korea (South), 2020

- Multi-Pad Receivers for High Power Dynamic Wireless Power Transfer, B. J. Varghese, R. A. Zane, A. Kamineni, R Tavakoli, Z. Pantic, C. Chou, Y. Liu, *2020 IEEE Energy Conversion Congress and Exposition (ECCE)*, Detroit, MI, USA, 2020

- Investigation of a DD2Q Pad Structure for High Power Inductive Power Transfer, B. J. Varghese, A. Kamineni and R. A. Zane, *2019 IEEE PELS Workshop on Emerging Technologies: Wireless Power Transfer (WoW)*, London, UK, 2019

- Empirical Closed-Form Analysis for Inductance and Coupling Coefficient Calculation for Ferrite-Based Matched Inductive Charging Systems, B. J. Varghese, A. Kamineni and R. A. Zane, *2019 IEEE Energy Conversion Congress and Exposition (ECCE)*, Baltimore, MD, USA, 2019

- Design and optimization of decoupled concentric and coplanar coils for WPT systems, B. J. Varghese, T. Smith, A. Azad and Z. Pantic, *2017 IEEE Wireless Power Transfer Conference (WPTC)*, Taipei, Taiwan, 2017